Aggregation, gelation and hydrodynamic spinning of whey proteins

Alice Vilotte

THÈSE

Pour obtenir le grade de

DOCTEUR DE L'UNIVERSITE GRENOBLE ALPES

Spécialité : **Mécanique des fluides, Energétique, Procédés**

Arrêté ministériel : 25 mai 2016

Présentée par

Alice VILOTTE

Thèse dirigée par **Hugues BODIGUEL,** Professeur des universités, Université Grenoble Alpes,
coencadrée par **Clément de LOUBENS,** Chargé de recherche, CNRS,
Komla AKO, Maître de conférence, Université Grenoble Alpes,
sous la supervision industrielle de
Deniz Z. GUNES, Expert scientifique, Nestlé Research, Lausanne
Christophe SCHMITT, Expert scientifique, Nestlé Research, Lausanne

préparée au sein du **Laboratoire Rhéologie et Procédés**
dans **l'École Doctorale I-MEP2 – Ingénierie – Matériaux, Mécanique, Environnement, Energétique, Procédés, Production**

Aggregation, gelation and hydrodynamic spinning of whey proteins

Thèse soutenue publiquement le **9 Juillet 2021**,
devant le jury composé de :

Monsieur Laurent HEUX
Directeur de recherche, Centre de recherches sur les macromolécules végétales, Université Grenoble Alpes, Président
Madame Laurence RAMOS
Directrice de recherche, Laboratoire Charles Coulomb, Université de Montpellier, Rapportrice
Monsieur Taco NICOLAI
Directeur de recherche, Institut des Molécules et Matériaux du Mans, Le Mans Université, Rapporteur
Monsieur François LEQUEUX
Directeur de recherche, Laboratoire Sciences et Ingénierie de la Matière Molle, ESPCI Paris, PSL University, Sorbonne Université, Examinateur
Monsieur Thomas CROGUENNEC
Professeur des universités, INRAE, Agrocampus Ouest, Examinateur
Monsieur Hugues BODIGUEL
Professeur des universités Laboratoire Rhéologie et Procédés, Université Grenoble Alpes, Directeur de thèse

Remerciements

Ce travail de recherche a été réalisé au sein du Laboratoire Rhéologie et Procédés, sous la direction de Monsieur Hugues Bodiguel, Professeur des universités à l'Université Grenoble Alpes et la supervision de Monsieur Clément de Loubens, chargé de recherche au CNRS. Ce projet de recherche a été porté et financé par la collaboration industrielle de Nestlé (Nestlé centre de recherche, Lausanne, Suisse), encadré par Monsieur Deniz Z. Gunes et Monsieur Christophe Schmitt.

J'adresse en premier lieu mes chaleureux remerciements à Hugues Bodiguel et Clément de Loubens pour la qualité de leur encadrement scientifique qui m'a permis de me former consciencieusement au métier de la recherche ; de toujours questionner mes résultats et leur faire confiance. Je les remercie pour toutes les connaissances scientifiques et compétences transversales que j'ai acquises à leur côté grâce à leurs conseils et leur encadrement. Je les remercie tout particulièrement pour leur patience, pour leur gentillesse, pour leur écoute, pour leur grande disponibilité ainsi que pour leur porte qui restait toujours ouverte. Le chemin tracé par les tasses de café m'a toujours permis de remonter jusqu'à eux. Je remercie également Komla Ako, co-endrant de ce travail pour son encadrement, sa disponibilité ainsi que pour nos discussions scientifiques.

Je remercie sincèrement Monsieur Deniz Z. Gunes et Monsieur Christophe Schmitt, sans qui ce projet n'aurait pas vu le jour. Je les remercie pour leur confiance, leur accueil lors de mes séjours au centre recherche, la très grande qualité de nos échanges scientifiques qui m'ont permis d'accroitre mes connaissances sur le vaste monde des protéines.

Je remercie les rapporteurs et tous les membres du jury d'avoir participé à la lecture et à l'évaluation de mes travaux de recherche, et également d'avoi nourri notre discussion scientifique par leur expertise et l'intêret porté à ce travail. Je remerciement vivement Madame Laurence Ramos et Monsieur Taco Nicolai d'avoir accepté de rapporter ce travail. Merci également à Monsieur Laurent Heux d'avoir accepté de présider ce jury. Merci à Monsieur François Lequeux et Monsieur Thomas Croguennec d'avoir accepté d'examiner ce travail.

Mes sincères remerciements vont à tous les membres du Laboratoire Rhéologie et Procédés ainsi qu'à Madame Nadia El Kissi, directrice du laboratoire durant mes années de doctorat, pour m'avoir acccueillie. Je remercie également tout le personnel permanent du laboratoire pour leur gentillesse quotidienne : Louise, Sylvie, François, Éric, Mohamed, Didier, Fréderic, Vincent; Frédéric Pignon pour nos discussions sur le SAXS, Denis pour ta bienveillance et ta bonne humeur ! Un merci particulier aux doctorants de ma promo, déjà ou bientôt docteur ! Merci Mehdi pour ton amitié. Je prends modèle sur ta superbe persévérance face aux aléas expérimentaux, ta positivité et ton optimisme, ta force face aux aléas de la vie. Une pensée tout particulière à ma team girlpower: merci Mathilde d'avoir été ce sacré binôme de doctorat, toujours disponible pour une pause café/thé/piscine/mojitos ou un déjeuner dans ta cuisine, et d'avoir emplit notre bureau de ce rire si communicatif. Merci Amélie pour ton amitié indéféctible, ta douceur, ta force au travail comme au quotidien et tes merveilleux

coups de crayons. Merci Candice pour ton amitié et ta bonne humeur communicative ! Merci à tous les doctorants qui ont contribué de près ou de loin à cette aventure et partagé une partie de laser game, une position de yoga, une bière, un cookie, une soirée, un déjeuner ou une pause café : Diego, Revaz, Youness, William, Hanna, Mamasita, Hajar, Louis, Hugues, Ayoub, Adja. Merci William pour tes déblocages latex de dernière minute !

Je remercie chaleureusement les membres de l'équipe protéines du centre de recherche de Nestlé auprès de qui j'ai pu me former : Sandrine, Claudine, Luca, Anne-Marie. Merci Lionel pour ton accompagnement scientifique et amical durant ma thèse, et ton accueil toujours chaleureux lors de mes venues au CRN.

Je remercie mes Totaly Spies, Mathilde, Marion et Orianne, ces amies d'une Vie qui apportent à chaque moment une saveur inoubliable ! Je ne compte plus les années passées à vos côtés, depuis les intercours au collège et lycée à se retrouver pour papoter, les compétitions de babminton, aux soirées pyjamas et autres soirées endiablées avec Céline. Mais surtout, votre amitié indéfectible est pour moi source continuelle de richesses, de pépites, de réflexions, de projets et de joie. Merci d'être les très chères témoins de mes succès et de mes échecs mais surtout celui de mon bonheur.

Une grosse pensée à la famille K2 : nessi, dame soso, beber, lucos, margue, apo, nass, ariane, des bancs des classes préparatoires à ceux de l'agro, de Paris à Grignon en passant par le Kremlin, merci pour votre soutien, votre amitié et votre unicité !

Merci à ma super team dreCHAge - Vanina, Audrey, Léa, Faby, Norine, Caro, Olivier - qui a illuminé mes mercredi et jeud soirs, contre vents, neige et marées, et m'a initié durant plus de trois ans à cet art vivant rigoureux et pétillant qu'est le dressage, sans oublier Piadzzo, ce compagnon hors-pair dont je n'oublierai jamais la gentillesse indéfectible.

Je remercie tous les professeurs qui m'ont encadré durant mes études et m'ont donné le goût des sciences ; Mme Metz pour avoir planté la graine du fameux adage « structure/fonction » qui m'émerveille toujours autant, grâce à ces fabuleux cours de biologique en classe préparatoire ; mes tuteurs de stage et tout particulièrement Avenaash Bala, qui m'a accueilli au centre de recherche de Fonterra et m'a transmis son goût de la recherche et dirigé vers la voie du doctorat.

Un immense et tout particulier merci à ma famille. A mes parents, qui m'ont toujours soutenue dans tous mes choix. Merci pour l'éducation que vous m'avez transmise, l'enseignement que vous m'apportez encore aujourd'hui et l'encadrement que vous m'avez procuré et qui m'a permis d'arriver jusqu'ici. A mes deux grands frères, Florent et Antoine, qui sont une grande source d'inspiration au quotidien et dont je suis fière et heureuse d'avoir à mes côtés. Je dédie également ce travail à mes grands-parents, qui m'ont également inculqué, de part leur histoire et personnalité, la valeur du travail. Enfin je dédie cette thèse à celui avec qui cette aventure scientifique a commencé il y a plus de trois ans et avec qui la grande aventure commence. Ton soutien me porte et m'accompagne depuis le début, et n'a jamais failli dans les

moments difficiles. Tu réinventes chaque petit moment de la vie et y apporte la saveur propre au bonheur. Les adversités traversées face à l'éloignement géographique semblent bien loin, personne ne connaitra mieux que nous les variations des lueurs matinales tant sur le clocher de la gare de Lyon que sur les rochers des montagnes grenobloises au gré des saisons. Vive la ghilice !

Contents

Abstract

Whey protein isolates have received increasing interest due to their high nutritional value and their growing availability on the market as a co-product of cheese production. Whey protein isolate (WPI) can be aggregated upon heating to create new functional properties, which depend on aggregate size and structural properties. Based on the fractal properties of these aggregates, one major application is to texture food products by two different ways: by forming a stable suspension of aggregates or by forming a space filling network, through a gelation process. Fractal aggregate size generally ranges from a few hundred nanometres to a few microns at most. However, it would be interesting if their size could reach at least 30 microns (the limit of consumer perception), to increase their thickening power (assuming aggregates remain fractal). Up to now, technological routes to create thickening particles were based mainly on the physico-chemical conditions of aggregation. The objective of the PhD is to study new aggregation and gelation processes, with the aim to produce novel aggregate structures, to enhance their texturizing ability.

Firstly, a good understanding of molecular self-assembly was required, taking into account the industrial process parameters. Indeed, in industrial conditions, aggregates are obtained under flow conditions at high temperature ($\geq$75°C) in few minutes. We developed a down scaling approach to study both the kinetics of aggregation after few seconds and its dependence with the mean shear rate, in which heat transfer does not limit aggregation. The size and mass of aggregates and protein conformation were characterized by small-angle X-ray scattering (SAXS) and resonant mass measurement (RMM). We showed that for fractal aggregates formed at low WPI and salt concentration, (i) aggregation at 92°C was limited by a step of nucleation, (ii) shear rate had no significant effect on the size of the aggregates, or on the aggregation kinetics and (iii) slower thermalization led to smaller aggregates size.

Secondly, standard characterization methods of aggregates structure being limited to sub-micrometric aggregates, we developed a new method for aggregates of several tens of microns based on a covalent labelling of WPI and fluorescent microscopy. We have shown that, depending on the physico-chemical and heating conditions, the range of size where fractal aggregates exhibits a fractal dimension equal to 2 can be extended from 10 to 60 μm.

Thirdly, we developed a new structuring process to form fibers from fractal aggregates, by a combination of microflows and Ca^{2+}-induced gelation. The WPI fibers presented a core-shell structure. Moreover, the size and the stability of the fiber was due to a complex interplay between different phenomena: hydrodynamics stresses, gelation kinetics, local pH changes during gelation and osmotic stresses.

Finally, characterization of gelation of fractal aggregates by Ca^{2+} was carried out in a bi-dimensional geometry in order to gain insights on the different phenomena that govern the formation and structure of the fiber. Especially, we showed the presence of osmotic flux which concentrates the aggregates in a front and form the shell of the fiber.

Key words: Whey protein isolate , aggregation, gelation, kinetics, hydrodynamic spinning, kinetics, microfluidic

Introduction

Whey proteins isolate are of increasing interest due to their high nutritional value and their growing availability in the market as a co-product of cheese production. Whey proteins isolate (WPI) can be aggregated by heating to create new functional properties that depend on the size of the aggregates and their structural properties. This wide range of functional properties is derived from the properties of globular proteins. They have been shown to form stable suspensions of structurally diverse aggregates, stabilized by repulsive interactions [56]; to form soft solid networks by salt or acid induction in one or two steps above a critical protein concentration [5, 46]; to improve the formation of emulsions by heating; to improve emulsion formation and stability through increased surface hydrophobicity [90]; to be used for encapsulation and release of bioactive components through pH-sensitive gel swelling behavior [73]. In the food industry, one of the main applications of WPI aggregates is as natural food thickeners. In this regard, the challenge is to control the structure of the aggregates to impart thickening properties.

A complex interaction between physico-chemical parameters such as pH, ionic strength and protein concentration has been shown to influence the aggregation kinetics and resulting structure-related properties of the aggregates. For more than twenty years, the influence of physico-chemical and heating parameters has been studied on protein aggregation (kinetics, structures and resulting properties) at a static laboratory scale, in order to control the structure and resulting properties of the aggregates.

At the industrial scale, the aggregation process can be subjected to other parameters such as a strong thermal gradient and shear gradients in a continuous small-scale flow process. The shift from a static to a continuous aggregation process has led to new research on process parameter studies. Several studies have examined the influence of shear or flow regime on the aggregation process and the resulting aggregate structure [29, 38, 116, 136]. These studies have shown the joint influence of several parameters and revealed the complexity of the mechanisms on the resulting size of the aggregates.

For several years, the structuring of aggregates has also been studied from a process-oriented approach in order to shape the aggregates. For example, microfluidic flow focusing geometry has been used to generate monodisperse and stable whey protein microbeads in a hydrophobic phase [6]. Studies have also focused on the formation of elongated structures (fibers) from whey protein aggregates. The structures of fractal dimension equal to 1 are interesting for the texturing of food products thanks to their entanglement and their aspect ratio. The process approach allows to modulate both the size and the structure. Coupled with the knowledge of the effects of physico-chemical parameters, flow structuring offers new ways to elaborate innovative structures.

This thesis focused on the understanding of thermal aggregation of whey proteins and the development of new aggregation and gelation processes in order to produce new aggregate structures to improve their texturizing ability. It was the result of a collaborative research with the Nestlé Research Center, Lausanne, Switzerland and was funded by Nestlé Research, Lausanne, Switzerland.

Chapter 1 presents the physico-chemical concepts and general mechanisms concerning the denaturation and thermal aggregation of whey proteins as well as the cold gelation induced by the addition of salts. The influence of process parameters such as temperature and shear was also presented. Flow structuring has been introduced in the context of the formation of whey protein gel spheres and in the context of hydrogel fiber formation more generally. We concluded this chapter by defining the objectives of the thesis with respect to the state of the art.

Chapter 2 presents the materials and methods used in the manuscript and details the analyses made by small angle X-ray scattering.

Chapters 3, 4, 5 and 6 results are presented as articles and were therefore written in English.

Chapter 3 was published in Food Hydrocolloids in 2021 and investigated the denaturation and aggregation kinetics under high temperature flow and the effect of shear on the kinetics, size and mass of the aggregates. A small-scale flow aggregation process was developed to decouple the effect of temperature and shear by neglecting the effect of the thermal gradient.

Chapter 4 presents and highlights a methodology developed to overcome the lack of structural characterization methods for aggregates of several tens of microns in size. This method was based on quantitative image analysis of covalently labeled fluorescent aggregates and allowed the characterization of the size and protein mass of aggregates.

Chapter 5 presents a new flow structuring of fractal aggregates, which was based on the reaction diffusion of calcium ions in a jet of a concentrated aggregate suspension, and studied the influence of hydrodynamic, physico-chemical parameters on the formation, size and stability of the gelled fibers.

The results of chapter 6 are presented as an opening and bring additional elements of understanding to the results of chapter 5.

Valorization of the work

Publication

A. Vilotte, H. Bodiguel, K. Ako, D. Gunes, C. Schmitt, C. de Loubens, 2021, Whey proteins aggregation in a millifluidic continuous process (2020) Food Hydrocolloids 110 (2021) 106137 DOI: 10.1016/j.foodhyd.2020.106137

Oral presentations

A. Vilotte, H. Bodiguel, K. Ako, D. Gunes, C. Schmitt, C. de Loubens. Influence of kinetic and shear parameters on the structure of whey protein aggregates by Small-Angle X-Ray Scattering and Fluorescent microscopy. *Edible Soft Matter*. April 2019, Le Mans, France.

A. Vilotte, H. Bodiguel, K. Ako, D. Gunes, C. Schmitt, C. de Loubens. Whey protein aggregation : a kinetic study under flow. *International Congress on Rheology*. December 2020, Cyberspace.

A. Vilotte, H. Bodiguel, K. Ako, D. Gunes, C. Schmitt, C. de Loubens. Shaping hollow fibers of whey protein isolate. *GdR SLAMM - journée thématique « Les protéines sont-elles des colloïdes/polymères comme les autres ? »*. January 2021, Cyberspace.

A. Vilotte, H. Bodiguel, K. Ako, D. Gunes, C. Schmitt, C. de Loubens. Shaping hollow fibers of whey protein isolate. *The Annual European Rheology Conference*. March 2021, Cyberspace.

C. de Loubens, A. Vilotte, H. Bodiguel, K. Ako, C. Schmitt, D. Gunes. Whey protein aggregation : a kinetic study under flow. *International Symposium on Food Rheology and Structure*. June 2019, Zurich, Switzerland.

Poster presentation

A. Vilotte, H. Bodiguel, K. Ako, C. Schmitt, D. Gunes, C. de Loubens. Whey protein aggregation : a kinetic study under flow. *International Colloids Conference*. June 2019, Sitges, Spain

Chapter 1

State of the art and objectives

Contents

1.1 Bovine whey proteins

1.1.1 Whey proteins

Milk is a biological fluid composed of water, lactose, lipids, proteins and mineral salts. It is defined as both a colloidal suspension of proteins in a continuous phase composed of water and mineral salts and as an emulsion of fat globules in a continuous phase. Milk proteins are composed of 80 % of micellar caseins and 20 % of whey proteins. These two classes of proteins are differentiated mainly by their structure, their solubility at pH 4.6, their thermal stability as well as by their very different physico-chemical properties. Micellar caseins are characterized by a colloidal structure, by their resistance to heat treatment and by their precipitation at pH 4.6. Whey proteins or serum proteins are globular proteins that remain soluble at pH 4.6 following isoelectric precipitation of micellar caseins. They are mainly composed of β-lactoglobulin, α-lactalbumin, immunoglobulins and bovine serum albumin. They are characterized by their sensitivity to heat which induces conformational changes until the denaturation of their secondary structure.

1.1.2 Structure of native proteins

Proteins are macromolecules defined by an assembly of amino acids linked by a peptide bond and characterized by four levels of structural organization. Amino acids are ampholytes that give the protein an amphoteric character. A protein is made up of amino ($NH2/NH^{3+}$) and carboxylic ($COOH/COO^{-}$) terminal groups that can be ionized according to their ionization constant (pKa), as well as a side chain whose residues can be hydrophilic or hydrophobic. Among the hydrophilic amino acids, we distinguish basic (lysine, arginine, histidine), acidic (aspartate and glutamate) and polar amino acids whose side chain is not charged. Hydrophobic amino acids are characterized by their non-polar side chains.

In its native form, β-lactoglobulin is composed of 162 amino acids including about 20 basic amino acids and 28 acidic amino acids, a free thiol function (-SH) whose reactivity is a function of pH ($pK_A = 8.3$ [56]), two disulfide bridges and a molecular mass of 18.3 kDa [19, 103]. Its isoelectric point is 5.2. It occurs in a monomer, dimer, or octamer equilibrium, shifted by pH, ionic strength, and/or temperature. The α-lactalbumin is composed of 123 amino acids and has eight cysteine residues all involved in disulfide bridges. It has a molecular weight of 14.2 kDa.

There are four levels of structure in the molecular structure of a protein.

Primary structure of a protein is its sequence of amino acids, linked together by a peptide bond that engages the carboxyl group of one amino acid and the primary amino group of a second amino acid. The mass of a protein is quantified in dalton or molecular mass, which is a dimensionless number. β-lactoglobulin has a mass of 18.2 kDa or 18 200 g/mol. Whey protein isolate (WPI) is given an average mass of 17.5 kDa.

The secondary structure involves hydrogen bonds between the side chains of the amino acids which will organize and stabilize locally certain segments of the peptide chain according to two distinct major motifs: the α helix and the β sheet. The two motifs are distinguished by the angles formed in the structure.

The tertiary structure describes the three-dimensional arrangement of the protein. It corresponds to a higher degree of organization after the secondary structure. This folding gives the protein its specific functionality. The tertiary structure involves different types of covalent and non-covalent interactions: hydrophobic, electrostatic, hydrogen, Van de Waals.

The quaternary structure is the last level of organization of proteins and describes the arrangement between several protein units. The non-covalent interactions involved are the same as in the tertiary structure. In solution at room temperature, the quaternary structure of β-lactoglobulin is organized into monomers and dimers depending on the environmental conditions. This monomer/dimer equilibrium is shifted towards the monomeric form under the effect of heat [32].

1.1.3 Nature and origin of covalent and non-covalent bonds

Covalent and non-covalent bonds play an essential role in stabilizing the three-dimensional arrangement of proteins and in their functionality. Weak non-covalent interactions allow the rearrangement of the tertiary structure which opens the way to new functionalities. Non-covalent bonds are composed mainly of four types of interactions: hydrogen bonds, Van der Waals interactions, hydrophobic interactions and electrostatic interactions. The energy required to break a non-covalent interaction is of the order of 4-20 kJ/mol. The understanding of the establishment of these bonds is essential for the understanding of the mechanisms of denaturation, aggregation, gelation and functional properties of aggregates. A distinction is made between "physical" gels formed by reversible attractive bonds and "chemical" gels formed by chemical reactions involving irreversible bonds [139].

Electrostatic interactions are either attractive between two ions of opposite charge or repulsive between two ions of the same charge. The electric field being uniform in all directions, electrostatic interactions do not generate any specific geometry. They are a function of the distance between the charged groups, the interaction will decrease as a function of the distance between the groups.

Van der Waals forces are short-range forces, either attractive or repulsive in nature. We can distinguish the Keesom forces between two permanent dipoles (difference in electronegativity between two atoms), the Debye forces between a permanent dipole and an induced dipole (a polar molecule creates around it an electric field and if a apolar molecule comes in its vicinity, it is influenced by this field) and the London forces between an instantaneous dipole and an induced dipole (the electronic movements can punctually separate the (+) and (-) barycenters of an apolar molecule.

Under these conditions, the instantaneous moment of one of the molecules creates an induced moment on the other and vice versa).

Hydrophobic interactions result from the low affinity of non-polar residues for water molecules due to their hydrophobicity. The non-polar residues interact with each other by hydrophobic interactions and reduce the hydrophobic surface exposed to water molecules increasing the entropy of the system. In their tertiary structure, proteins will adopt a conformation that will tend to reduce the hydrophobic surface exposed to water molecules by burying the hydrophobic residues in the core of the structure. As hydrophobic interactions are noncovalent and relatively weak, they might rapidly dissociate [56].

Hydrogen interactions result from the interaction between a hydrogen atom and an electronegative atom carrying a non-binding doublet. Their establishment is favored at low temperature during the aggregation stage.

Covalent bonds are bonds of higher energy and are less easily broken. If proteins contain cysteines, disulfide bridges can be formed between two thiol functions -SH carried by the cysteines.

1.1.4 Ionization of proteins as a function of pH

The ionization of carboxyl and amino terminal groups and residues of amino acids of acidic (aspartate, glutamate) and basic (lysine, arginine) nature depends on pH, so they are either positively charged or negatively charged. These amino acids are therefore the main contributors to the net charge of a protein.

The net charge density reflects the amount of charge carried on the surface of the particle and is measured by potentiometric titration. It is defined as the sum of the charges of ionizable groups at a given pH and is noted α. It varies according to the ionization of the groups on the surface of the protein and thus the pH. The ionization of the groups depends on their pK_a value: asparatate: pK_a 3.86, glutamate: pK_a = 4.25, histidine: $pK_a = 6.0$, lysine: $pK_a = 10.53$, arginine: $pK_a = 12.48$ [16].

A pH value above the pK_a value will result in deprotonation of ionized groups, whereas a decrease in pH below the pK_a value will result in protonation of ionized groups. The variation in net charge density thus underlies the subsequent variation in repulsive electrostatic forces and variability in the resulting aggregate structures [56]. Electrostatic interactions depends on the net charge density rather than the pH and α depends on the protein concentration and ionic strength at a given pH.

The net charge density is distinguished from the effective charge density, which is measured by electrophoresis. This technique measures the value of the electric potential at the interface of the stern layer and the diffuse layer. This value, called zeta potential, takes into account the counter ions of the stern layer. When the pH increases, the polarity of the surface charge measured at the boundary of the stern layer and the diffuse layer reverses on either side of the isoelectric point where the potential is zero (IEP). This behavior is valid for most electrolytes. The evolution of

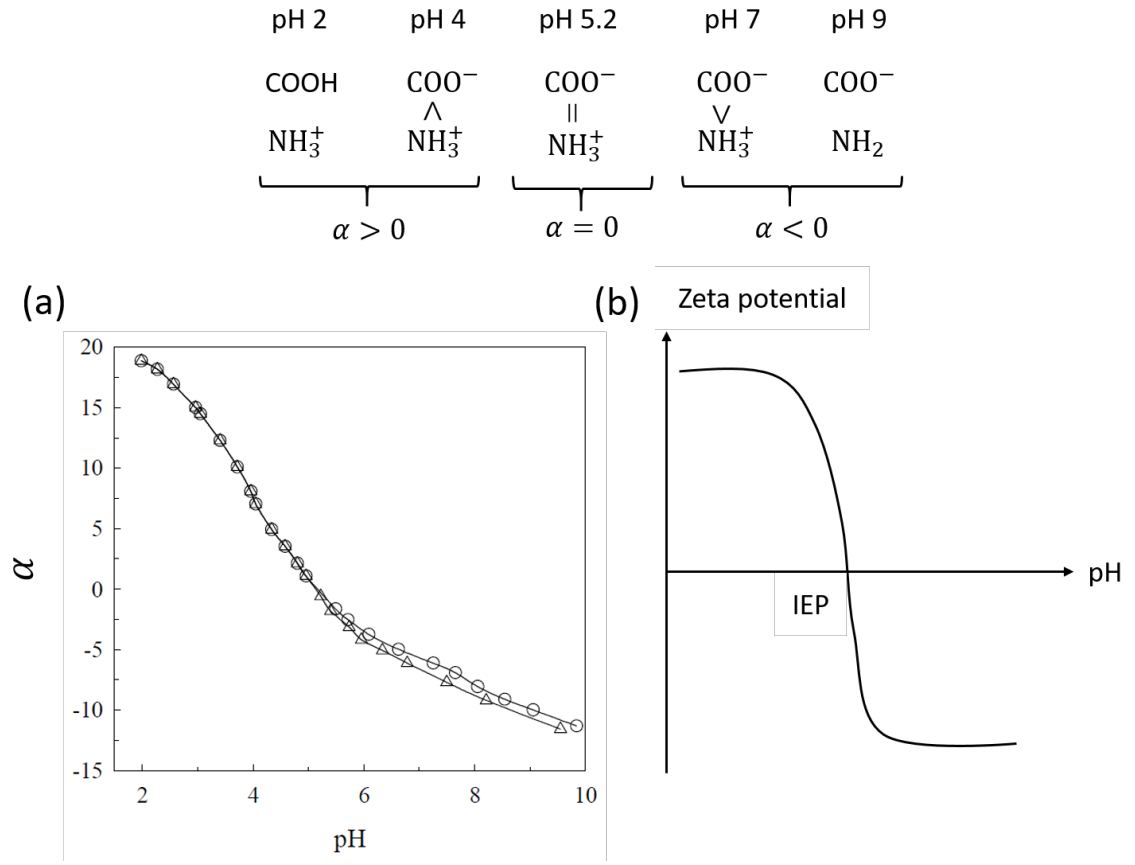

Figure 1.1: (a): Evolution of net charge α per monomer of β-lactoglobulin for genetic variants A and B in 0.25M KCl at 25°C and evolution of protonation/deprotonation of carboxylic and amino groups as a function of pH. Graph from Soraya Mehalabi's thesis (2008) and data from Basch and Timasheff (1967). (b): Evolution of the zeta potential of a charged protein as a function of pH. IEP is the isoelectric point.

the zeta potential as a function of pH is identical to the evolution of the net charge density as it results from it (Figure 1.1). An increase in the absolute value of the net charge density will induce an increase in the Debye length and consequently an increase in the absolute value of the zeta potential, a state for which repulsions are favored.

The isoelectric point is defined as the pH value at which the zeta potential is zero (equivalent to the net charge of the molecule and including the bound counterions). At the isoelectric point, electrostatic attractive forces are maximal and lead to aggregation of native proteins. At pH 7, the net charge of β-lactoglobulin will be negative with the carboxyl and amino groups in the COO^- and NH^{3+} form. The charge distribution in the protein is not symmetrical on either side of the isoelectric point, which gives it different properties.

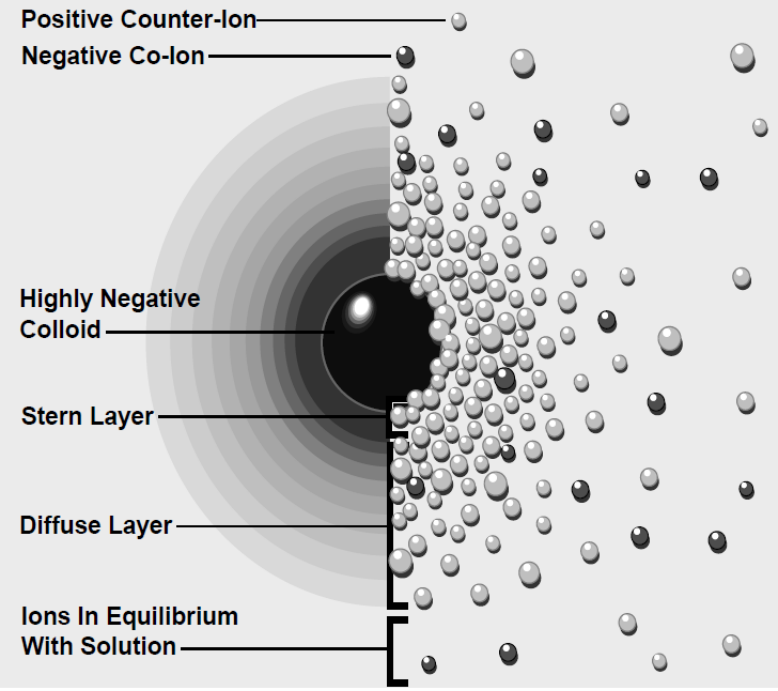

Figure 1.2: Representation of the double layer model. The left view shows the variation of the charge density around the colloid. The charge density decreases as one moves away from the charged colloid. The right view shows the distribution of positive and negative ions.

1.1.5 Influence of salt concentration and type

The concentration of salts as well as the valence of the salt change the extent of repulsive interactions and can also change the net charge of the particles by their action on the dissociation constants (pK_a). The charged residues present on the surface of proteins and aggregates will generate electrostatic interactions with ions present in solution (salts initially present in the powder or added later), of an attractive nature with counter ions of opposite charge and repulsive with co-ions of the same charge. Several models describe the distribution of ions in the vicinity of a charged surface in an ionic double layer, inducing a spreading of the charges of the charged particle over a characteristic length (the Debye length, equivalent to the thickness of this double layer), thus favoring the repulsions between particles. The ionic double layer is composed of the Sterne layer, made of counter ions strongly bound to the charged residues of the protein surface and of a diffuse layer, in which are distributed co-ions and counter ions of opposite charges, more mobile (Figure 1.2).

As the ionic strength of the solution increases, i.e. as the concentration of ions in the solution increases or as the valence of the ions in the solution increases, the distribution of ions within the diffuse layer changes. The thickness of the ionic double layer (or Debye length) decreases and becomes more compressed and the charge density decreases near the colloid. The charge density reflects the difference in concentration of positive and negative ions at a point: the smaller the difference in concentration of positive and negative ions, the lower the charge density. The

thickness of the ionic double layer represents the extent of the electrostatic forces. Thus, when the ionic strength of the solution increases, the range of the repulsive electrostatic forces decreases and the attractive forces of short range will dominate and lead to the aggregation of proteins.

It is the interference of the electronic double layers of two particles that induces the electrostatic repulsions (see salting-in). The range of electrostatic interactions are determined mainly by the net charge of the proteins and by the ionic strength of the environment affecting the double layer. Their range increases with the thickness of the double layer and the absolute value of the zeta potential.

Salt concentration also influences the net protein charge measured by potentiometric titration. According to Salis et al. (2011) at a fixed pH, the net charge increases with NaCl concentration inducing an increase in the pH value of the isoionic point. Thus at acidic pH and basic pH, the absolute net charge increases with salt concentration, thus increasing electrostatic repulsions. Taking into account the dispersion forces of the ions (non-electrostatic forces) would explain the influence of the salt concentration on the increase of the net charge. Conversely, an increase in NaCl concentration induces a decrease in absolute value of the zeta potential. The influence of the salt concentration on the values of dissociation constants of the ionized groups was also highlighted on a globular protein, the lyzozyme [66].

The valence of the ions also influences the mechanisms of the interactions. The effects of divalent ions are often not only stronger (due to the higher charge), but qualitatively different from monovalent ions. In particular, the presence of multivalent ions can induce effective charge reversals on the surface of negatively charged proteins [140]. One of the hypotheses behind this mechanism is the establishment of specific short-range interactions between multivalent ions and amino acid residues on the surface of proteins [141]. The role of Ca^{2+} in aggregation mechanisms has been studied in the case of thermal aggregation and cold gelation. Ca^{2+} ions were first suspected to induce aggregation by their ability to act as bridges between negatively charged carboxyl groups on neighboring protein molecules. This mechanism was set aside in favor of the hypothesis of a specific interaction between calcium ions and carboxylates with a threshold affinity [137], [117], [54]. Kharlamova et al. (2018) showed that Ca^{2+} ions reduced the effective negative charge density of aggregates as the number of moles of Ca^{2+} per aggregate increased (Figure 1.3). Zittle et al. (1957) also pointed to the establishment of specific interactions by Ca^{2+} ions, and found them to be analogous to pH in terms of net charge.

Increased salt concentration can also weaken the strength of ionic interactions stabilizing a molecular structure, known as salting-out. A high ionic strength can also neutralize certain ionic charges required on the surface to maintain solubility and compete with proteins to interact with water molecules in solution. The proteins are then deprived of the water molecules that hydrate them and the hydrophobic interactions lead to protein precipitation.

Conversely, at low salt concentration, proteins are surrounded by counter ions that interact with the ionic charges of the proteins and contribute to decrease the intermolecular electrostatic attractive interactions leading to stabilization. This is called salting-in.

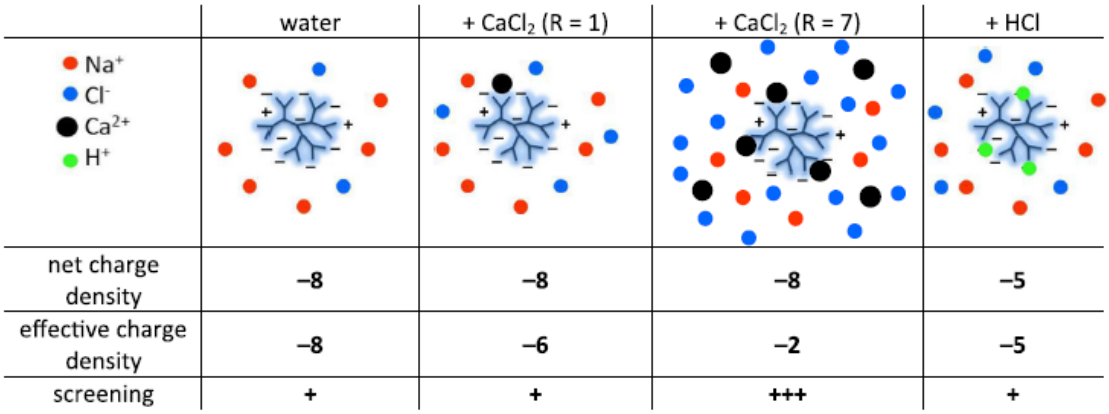

Figure 1.3: Variation of the net and effective charge density of aggregates, as well as the range of electrostatic repulsions by charge screening depending on physicochemical conditions. The figure is taken from Kharlamova et al. (2018)

1.2 Thermal aggregation and gelation

1.2.1 Thermal denaturation and aggregation of native whey proteins

In the dairy industry, denaturation and subsequent aggregation of proteins can lead to undesirable effects such as clogging of industrial pipes and have been the subject of numerous publications. In the pharmaceutical industry, the mechanisms of protein conformation change, inducing a modification of their functionality, have been intensively studied as suspected to be involved in neurodegenerative diseases.

Bovine whey globular proteins are characterized by their sensitivity to heat. At room temperature in aqueous solution, β-lactoglobulin is in equilibrium in a dimeric and monomeric form at neutral pH and low ionic strength. This quaternary structure is modified and the dimeric dissociation is favored by the increase of the temperature and of the charge density as well as by the decrease of the ionic strength [8, 131]. This is the dissociation stage. In a temperature range up to the denaturation temperature, the structure of the protein undergoes minor reversible conformational changes, allowing the exposure of some groups that are not exposed in the native state. This is the reversible denaturation step.

Above the denaturation temperature, the protein partially unfolds, its tertiary and secondary three-dimensional structure undergoes a conformational change, which is accompanied by an increase in the mobility of the peptide chain and the spatial reorganization of ionized, hydrophobic residues and free thiol functions that can form new spatial interactions [26, 76]. The resulting structure is characterized as a "molten globule state" [33, 50]. The unfolding of the proteins is accompanied by the formation of new irreversible interactions (covalent interactions between thiol groups, hydrophobic interactions), making the newly formed structure irreversible even with decreasing temperature. This is the stage of irreversible denaturation. Covalent

and/or non-covalent bonds are formed between the irreversibly denatured proteins and lead to the formation of aggregates.

Thermal denaturation can be described simply in two steps : a denaturation and an unfolding step of the first order reaction and a second aggregation step of a second order reaction [130]. Several mechanisms take place during the denaturation and aggregation of whey proteins:
1) Dissociation of dimers
2) Reversible unfolding and association
3) Irreversible unfolding and association
4) Aggregation or polymerization
5) Terminaison

Two steps can be distinguished during the aggregation process. First, primary aggregates are formed when the concentration of oligomers exceeds a critical amount. The primary aggregates are curved strands at pH 7 with a length of about 50 nm and a diameter of about 10 nm, and approximately spherical with radii up to 150 nm at pH 5.8 [89]. They remain stable at lower protein concentration but assemble into larger polydisperse self-similar aggregates during a secondary aggregation step, or a gel, at higher concentrations. Cross-links between the proteins in the aggregates involve both hydrophobic interactions and hydrogen bonding and above the iso-electric point, covalent disulfide bonds are also involved. The aggregation step can be either diffusion-limited or reaction-limited. In the case of a diffusion-limited reaction, the reaction is so fast that the rate is equal to the diffusion of the particles, each contact between the particles resulting in their binding with $d_f = 1.8$. In the case a reaction-limited aggregation rather polydisperse aggregates are formed with $d_f = 2.0$.

Many studies have focused on the kinetics of heat-denaturation and aggregation of the major whey proteins to optimize heat treatments and the subsequent formation of well designed aggregates with desired functional properties. The rate of denaturation and aggregation of β-lactoglobulin depends on several factors such as pH, ionic strength, initial protein concentration and temperature. The denaturation and aggregation kinetics of the major whey proteins (β-lactoglobulin and α-lactalbumin) and the mechanisms involved under conditions of neutral pH and low ionic strength have been studied extensively since the 1980s, over wide temperature ranges from 70°C to 150°C [28, 130] and have given rise to different models [9, 109, 127].

Previous works have shown that the formation of soluble protein aggregates can be achieved through the control and modulation of physico-chemical parameters, leading to the generation of protein aggregates with well defined structural properties (diameter and molecular weight) [148].

1.2.2 Modulation of the aggregate structure and functionality by the conditions of aggregation

Aggregates structural characterization

The characterization of the structure includes size, morphology, internal structure and also fractal dimension. The structure of aggregates can be analyzed by microscopy (optical microscopy with or without fluorescence, confocal laser scanning microscopy, transmission electron microscopy, laser scanning electron microscopy) and by scattering techniques such as static and dynamic light scattering, small angle X-ray scattering, small angle neutron scattering. The scattering techniques allow the determination of the form factor, the structure factor, the hydrodynamic radius or the radius of gyration, the fractal dimension as well as the molecular mass [9, 14, 69, 79, 101].

The hydrodynamic radius, R_h is the radius of the protein or molecule that take into account both its shape and its hydration layer. It is obtained by calculation according to the Stokes-Einstein relation after determination of the diffusion coefficient by dynamic light scattering. The hydrodynamic radius is determined from the extrapolation at zero angle and zero concentration of the diffusion coefficient.
Another often used measure of the dimension of the polymer chain is the radius of gyration R_g. Mathematically, it corresponds to the mean square distance between the atoms and the center of mass (Equation 2.5). The chains of a particle occupy the space of a sphere of radius R_g. For polymer solutions, the hydrodynamic radius measured by DLS can be related to the radius of gyration according to $R_h = 0.665R_g$ [125].

The molecular weight is defined, for a homogeneous polymer in mass, as equal to the product of the mass of its unit by its degree of polymerization. It is expressed in g/mol. Diffusion techniques give the weight average molecular weight M_w, in absolute value if it is measured at zero concentration and angle (requires the measurement of several different concentrations as well as a multi-angle study for each of the concentrations) and in apparent value if it is measured at fixed angle/concentration.

In the case of a fractal structure, characterized by an irregular shape with a geometrical property of self-similarity independent of the scale of observation, we define a parameter that links a characteristic dimension R of the object to its molecular mass M_w such as $M_w = M_p(R/R_0)^{d_f}$, with R_0 the radius of an elementary unit and M_p (Figure 1.5). d_f is the fractal dimension and its value gives an indication of how the object under study fills the space. It takes values between 1 and 3, in the case where $d_f = 3$, the object is a sphere equal to the dimension of the space. The fractal dimension can thus be deduced by plotting the mass as a function of the characteristic dimension R of the object.

These techniques are nevertheless restricted to particles smaller than a few microns. Structural data such as size, fractal dimension and molecular mass for aggregates of several tens of microns are not accessible with the current techniques presented above.

Influence of the net charge density

The structure of the aggregates formed by heat treatment can be modulated by varying the balance between repulsive and attractive forces by changing the net charge of the proteins or by charge screening [89, 148]. Jung et al. [56] formed aggregates of different size, morphology, internal structure and fractal dimension after heat treatment of a 1 % w/w solution of β-lactoglobulin at 90°C, by varying the pH from 2 to 5.8 and 7 (Figure 1.4).

When the pH is below the isoelectric point, the proteins are positively charged. Electrostatic repulsions between the positively charged groups induce the formation of fibrils with an elongated structure (Figure 1.4).
When the pH is close to the isoelectric point (pH = 4.2-6.0) the net charge density as well as the electrostatic repulsions decreased and allow the formation of roughly spherical protein particles called microgels with radii from 100 nm to 1 μm that strongly scatter light and have a milk-like appearance in suspensions [52, 81, 97, 112]. Their structure is held by hydrogen bonds, hydrophobic interactions, and also by covalent disulphide bridges. A microgel particle is thus constituted of crosslinked network and contains a large fraction of solvent [87]. Microgels can also be formed above the isoelectric point up to pH 7.5 in the presence of $CaCl_2$, or other divalent ions, for a certain range of molar ratio values between calcium ions and β-lactoglobulin [99]. The divalence of calcium ions allowed them to bind specifically to proteins, unlike monovalent ions (NaCl), and to decrease the net charge density.

When the pH is equal to 7 the proteins are negatively charged and have a high net negative charge density. Transparent solutions of smaller elongated aggregates are formed and can further aggregate into fractal (self-similar) aggregates. Fractal aggregates are characterized by a branched structure and a fractal dimension where d_f>1 and d_f<3 (Figure 1.5). The density of the fractal aggregates decreases with increasing size as $\rho \propto R^{d_f-3}$.

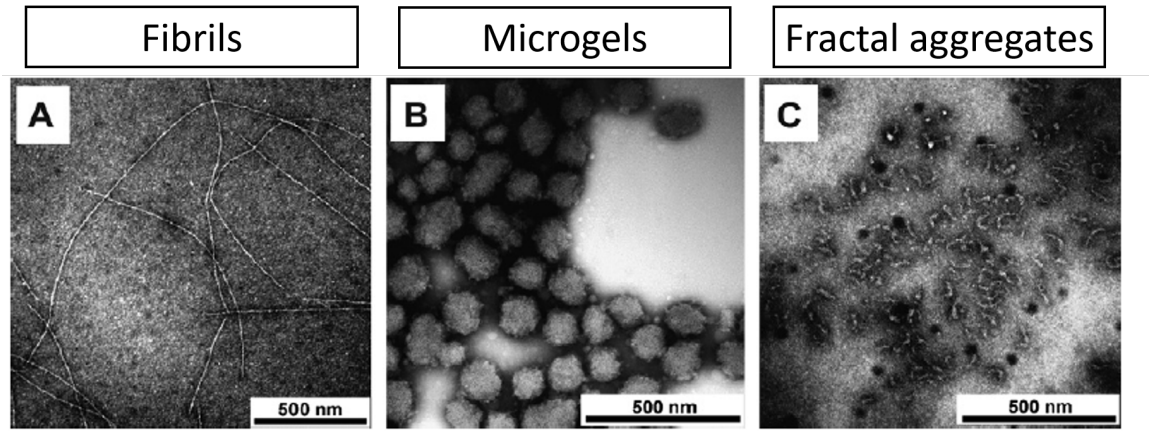

Figure 1.4: Transmission electron microscopy images of β-lactoglobulin aggregates (1% w/w) obtained after heat treatment (90°C) at different pH. (A): pH 2, (B): pH 5.8, (C): pH 7. Figure taken from Jung et al. [56]

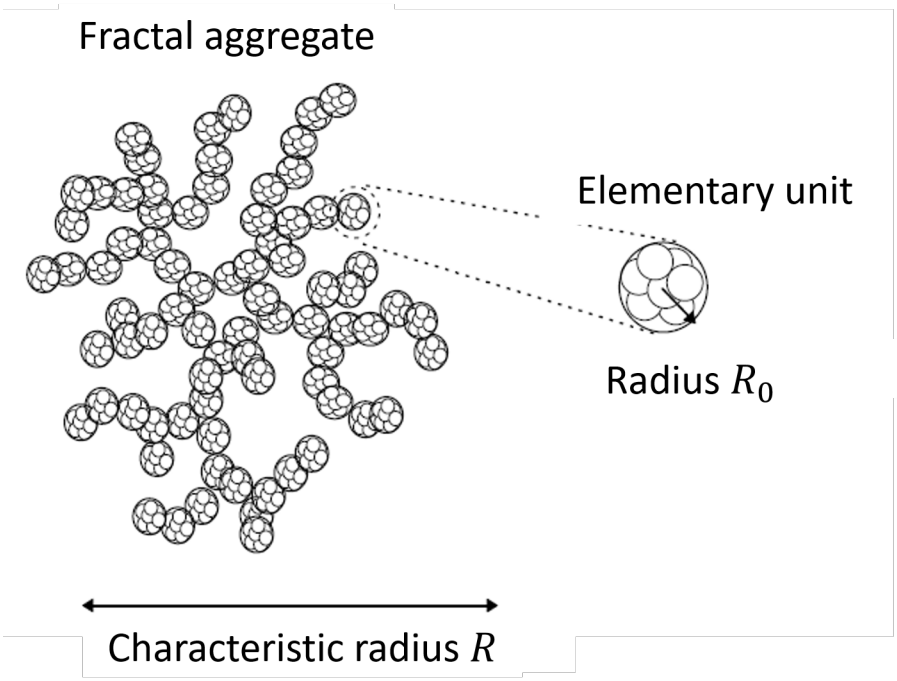

Figure 1.5: Schematic representation of a fractal aggregate of characteristic radius R, made of elementary units of radius R_0. Figure taken from Aymard et al. (1997),[10]

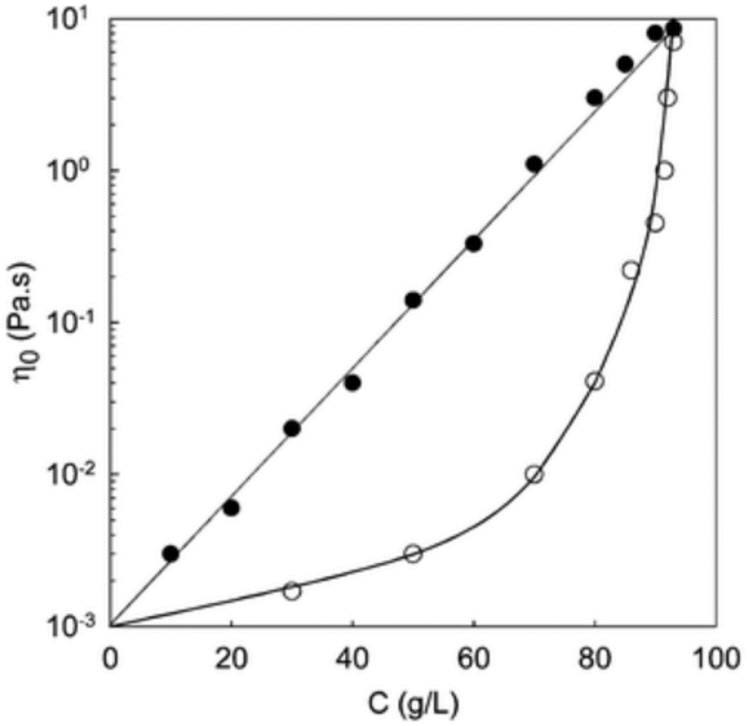

Figure 1.6: Viscosity evolution of fractal aggregate suspensions formed at different concentrations (open symbol) and formed at 93 g/L and then successively diluted. Figure taken from Inthavong et al. (2016), [52].

Influence of the native proteins concentration

A minimum concentration of native protein is required to induce aggregate formation (step 4). First, small pre-aggregates, or oligomers, are formed. If the concentration if sufficient, named critical association concentration [79], they associate into relatively monodisperse so-called primary aggregates. At higher protein concentrations the primary aggregates associate further into larger polydisperse self-similar aggregates. The effect of protein concentration on the rheological properties of fractal aggregates at constant net charge density has also been studied. Inthavong et al. [52] compared the evolution of fractal aggregate suspension viscosity as a function of β-lactoglobulin concentration depending on whether it was fixed before or after heat treatment (Figure 1.6). When the native protein concentration was varied before heat treatment, the resulting aggregate suspensions varied in aggregate size and in the concentration of aggregates formed. To vary the protein concentration after heat treatment, a suspension of aggregates was formed at a fixed concentration and then successively diluted: the aggregate size did not vary. The rheological behavior differed due to the different aggregation kinetics, which were dependent on the initial protein concentration and increased as the initial protein concentration increased. The protein concentration plays a role in the denaturation kinetics : the higher the protein concentration, the faster the denaturation reaction is.

Influence of salt concentration

The increase in salt concentration will participate in the reduction of electrostatic repulsions between charged colloids. Monovalent cations will partially or totally screen the negative charges according to their concentration. Divalent cations will generate a higher ionic force at lower concentration and will participate more efficiently in the screening of charges and also form ionic bridges between carboxylic groups [46, 47, 55]. For fractal aggregates, Le Bon et al. [69] and Pouzot et al. [101] reported a fractal dimension d_f equal to 2 for NaCl concentrations higher than 10 mM and equal to 1.6 for a NaCl concentration equal to 3 mM. Baussay et al. [14] indicated a local densification on short length scale when the NaCl concentration was higher than 0.2 M while the larger scale structure remained constant.

Influence of the temperature

The relationships of structural parameters of fractal aggregates with physicochemical conditions and heat treatment have been well studied in the low temperature regime. Below 85°C, aggregation was limited by denaturation and could proceed over several hours depending on the protein concentration [69, 89, 148]. At neutral pH between 75°C and 85°C, larger aggregates were formed, due to the prevalence of non-covalent interactions such as hydrophobic interactions. At temperatures higher than 80°C, noncovalent interactions become of increasing importance and the aggregation process is dominated by both interchange of disulphide bonds and hydrophobic interactions [40]. Between 85°C and 105°C smaller aggregates were formed by the establishment of disulfide bridges, hydrophobic interactions being limited in this temperature range [32] where the reaction was limited by aggregation.

Structure-function relation

The structure-function relationship is a crucial parameter that governs many biological processes. A function is thus determined by a particular structure. In the case of whey protein aggregates, the fractal dimension is an important structural parameter, especially in the rheological properties of aggregate suspensions and gels. Three types of structures are distinguished: fibrils, microgels and fractals. A fractal dimension can nevertheless be defined for fibrils and microgels. The elongated structures type fibrils are characterized by a fixed fractal dimension equal to 1 while the spherical structures type microgels have a fixed fractal dimension equal to 3. A fractal structure is characterized by an open structure, so the more the size increases and the more the particle will occupy space. Another interesting characteristic of fractal structures is the decrease of density with the increase of the size of the particles. Thus the larger the size of a fractal particle, the more space it will occupy with less matter. Fractal aggregates therefore seem to be well suited for food texturing applications. For the same protein concentration, the viscosity of a suspension of fractal aggregates was higher than that of a suspension of microgels and increased with the size of the fractal aggregates formed (Figure 1.6). The same viscosity value was achieved at lower protein concentrations when the size of fractal aggregates was

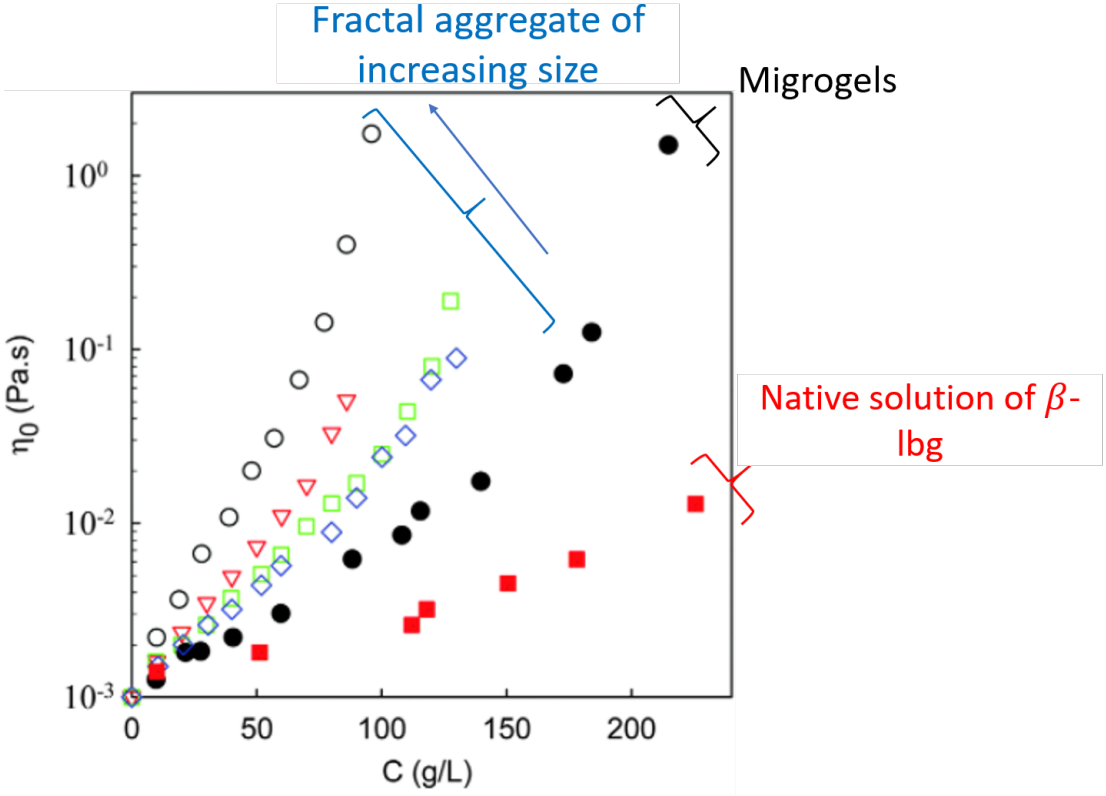

Figure 1.7: Viscosity evolution of fractal aggregate suspensions, microgels and native β-lactoglobulin solution for different concentrations. Figure from Inthavong et al. [52].

maximized. It follows that the rheological properties of gels formed from microgels or fractal aggregates will differ.

1.2.3 Gelation mechanisms

Presentation of the different gelation processes

Beyond a critical protein concentration (C_g), as the aggregation proceeds, the system changes from a dilute cluster regime to a dense cluster regime and when the cumulated volume (V_{ag}) occupied by the aggregates approach to total available space (V), the percolation of the system takes place, leading to the formation of a system spanning network (Figure 1.8). Reaction-limited aggregation forms polydisperse aggregates that can interpenetrate before being connected to the percolating network. The fraction of proteins incorporated in the network will increase until all proteins are part of the gel. The structure of the system is characterized by a correlation length, which is the average size of the aggregates when $V_{ag} \approx$ V. Below the correlation length, the structure of the gel is equal to the self-similar structure of the aggregates and is homogeneous above [86]. C_g decreases with increasing ionic strength or when the pH is close to the isoelectric point. Moreover, since the density of fractal aggre-

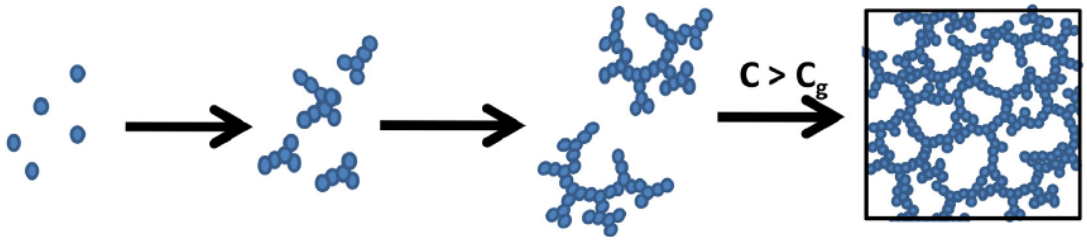

Figure 1.8: Schematic representation of globular protein aggregation and gelation. Fractal aggregates are formed by association of small strands and form a fine-stranded percolating network if the concentration is larger than the critical gel concentration. Figure from Nicolai et al. (2019) [86].

gates decreases with their size, gelation should occur even at low concentrations but at this point the gel strength could not be sufficient to resist gravity.

A gel can first be formed by heat treatment following denaturation and aggregation of proteins. The value of C_g is a function of the net charge and thus of the pH and the ionic strength (concentration and valence of the ions). These two physico-chemical parameters will modulate the net charge density and the effective charge density of proteins and aggregates and allow to induce gelation. Increasing the salt concentration increases the size of the aggregates by decreasing electrostatic repulsions and decreases C_g. Decreasing the net charge of proteins or aggregates reduces the extent of repulsive interactions and decreases C_g.

The gelation can also be decoupled and induced after the formation of a stable suspension of aggregates. This decoupling allows the gelling of a suspension of aggregates, previously thermally formed, by subsequent decrease of electrostatic repulsions, with or without heat treatment. A thermal treatment will increase the speed of gelation [46]. In this second stage we distinguish the gelation induced by acidification and the gelation induced by addition of salts.

It was shown that gels formed in one step by thermal treatment and gels formed in two steps with the same physico-chemical conditions exhibited different structures and mechanical properties. This result was not surprising and resulted from different intra- and intermolecular bonding mechanisms.

Veerman et al. [128] pointed out that the method used to induce gelation of pre-formed aggregates could lead to differences in gel formation for the same salt concentrations. Indeed, different methods of cold gelation by addition of salts are employed in the literature. The gels can be formed by progressive addition of the salt solution and under constant agitation but can also be formed by dialysis and thus resulted from the diffusion of ions towards the dialysis bag containing the suspension of aggregates. Depending on the diameter of the dialysis tubes, the diffusion time of the calcium ions can reach several hours [67], [47]. The gelation by dialysis resulted from a mechanism of diffusion reaction, the gelation reaction starting at the periphery of the coil could also influence the structure of the gel. The choice of the method can

thus influence the contact between the ions and the aggregates and the study of the gelation kinetics at short times.

Cold gelation induced by the addition of salts

Influence of the pre-aggregation step Studies have been conducted to investigate the effect of the first denaturation and aggregation step on the mechanical properties and the resulting structure of the gels. The concentration of aggregates, their size, their structure, the fraction of remaining native proteins are all parameters that can be modulated by the heat treatment, the salt concentration, the initial concentration of native proteins, the pH.

Many studies thus studied the effect of these parameters on the mechanical properties of the gels and compared the values once the steady state was reached. Increasing the heating time and temperature as well as increasing the initial concentration of native proteins increased the strength at break, elastic modulus, and water holding capacity of the gels as well as the size and concentration of aggregates [55], [67], [13]. At low initial protein concentration, intermolecular forces would have less effect on stabilizing the three-dimensional network than at high protein concentration.

The study of the influence of pre-aggregate size has often been correlated with the influence of aggregate concentration. Increasing the concentration of native protein before aggregation led both to the increase of the size but also to the increase of the concentration of aggregates. On the other hand, depending on the heat treatment and the concentration of native protein, the residual fraction of native protein can also vary. In order to study the effect of aggregate size by decoupling the two effects, gels should be formed at an equal aggregate concentration by diluting suspensions of aggregates formed at different native protein concentrations. Similarly, in order to study the effect of aggregate concentration, gels should be formed with a fixed aggregate size by diluting or concentrating a suspension of aggregates formed at a single native protein concentration. Kharlamova et al. [60] varied the aggregate concentration for different aggregate sizes and showed that a minimal protein concentration was required to induce gel formation in the second step (a heat treatment of 80°C was applied in the second step, Figure 1.9).

By decreasing the size of the aggregates, gels can be formed at lower protein concentrations (Figure 1.9) when heat treatment is applied during the second gelation step.

The influence of the structure of the aggregates after the thermal pre-aggregation step was also studied. Thus, at the same initial protein concentration, fractal aggregates will form a mechanically stronger gel with a more homogeneous structure compared to a gel formed from microgels, due to their fractal density: they are less dense and occupy a higher volume fraction [36, 61]. The size of the fractal aggregates did not influence the rigid component, nor the structure of the gels [61]. According to Ako et al. [2], the size of the pre-aggregates played a kinetic role in gel formation. Thus, forming larger aggregates would be equivalent to starting the cold gelation process at a later stage.

Two-step gelation by addition of salts has also been studied from fibrillar ag-

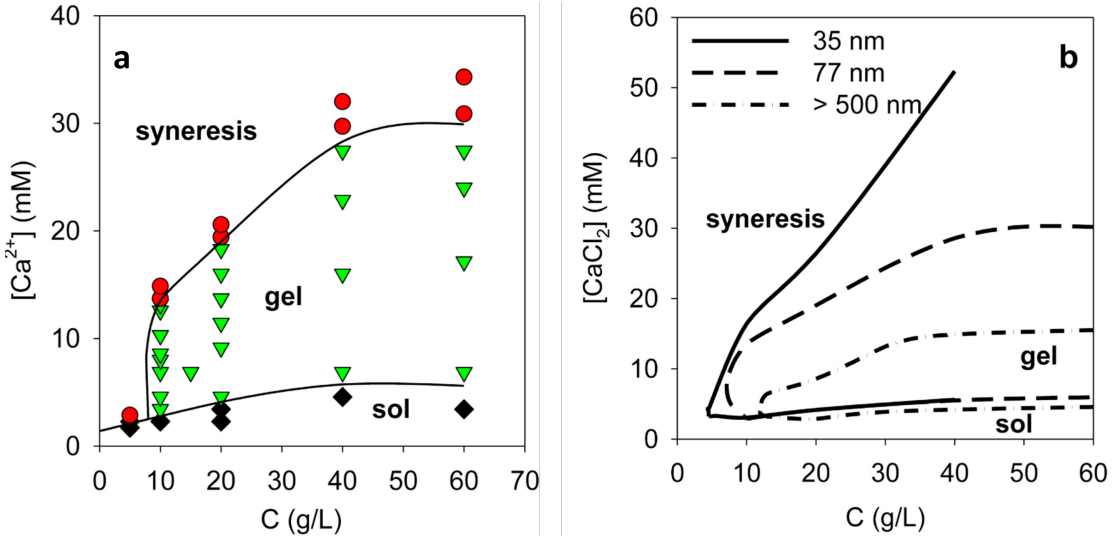

Figure 1.9: State diagram: solution, gel, and syneresis, function of protein concentration for aggregates of size set at $R_H = 77$ nm (a), and for different aggregate sizes shown in the figure (b). Figure from Kharlamova et al. (2018), [61].

gregates formed at acidic pH for which the "effective amount of structure" required to form a network when using fibrils was less than that of the "conventional cold gelation method" [128].

However, few studies have investigated the kinetics of gelation. In order to overcome the problem of short time for the study of gelation kinetics, the second step being a thermal activatable process, the progressive addition of the salt solution under constant agitation to the aggregate suspension can be performed at low temperature. The follow-up of the gelation over time can be quantified from a mechanical properties point of view by oscillatory shear tests (evolution of the elastic modulus) or structurally by light scattering techniques [2].

The effect of the concentration of constant size aggregates ($R_h = 35$ nm) on the elastic modulus of the forming gel was measured over time by Kharlamova et al. [61] after the addition of $CaCl_2$ at a fixed molar ratio equal to 6 and under a heat treatment of 80°C. Under these thermal and physico-chemical conditions, the evolution over time of the elastic modulus increased with the protein concentration with a first clear and rapid increase and then evolved more gently after about 300 second (Figure 1.10). As the concentration of aggregates increased, G' increased. The first values of G' were measured from about 60 second.

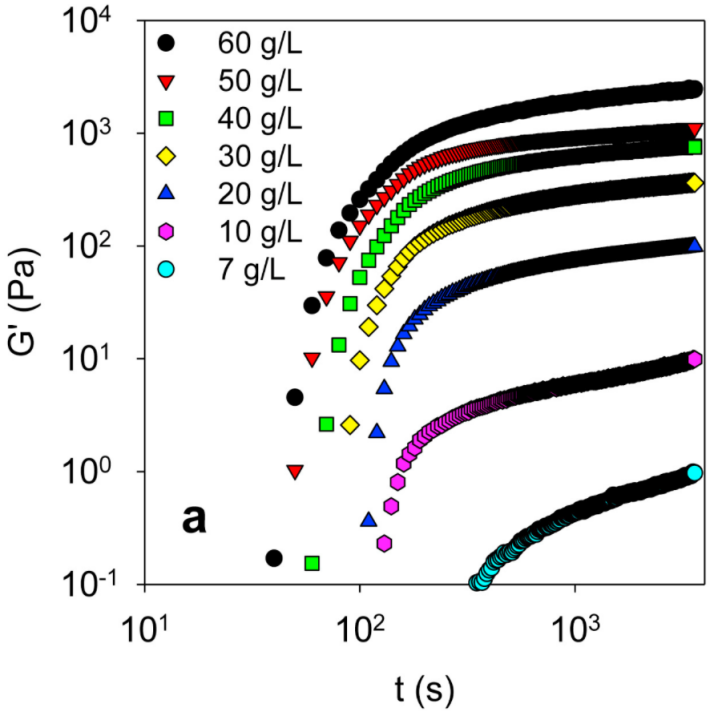

Figure 1.10: Evolution of elastic modulus over time at a temperature of 80°C for several solutions of WPI aggregates (R_h = 35 nm, R = 6) of different protein concentrations. Graph from Karlamova et al. (2018), [61]

.

Effect of the type of salts, the concentration and the molar ratio Monovalent salts such as NaCl or divalent salts, such as $CaCl_2$, can be used to induce gelation of pre-formed WPI aggregates. The valence of the ions is an important parameter in determining the type of interactions (electrostatic and non-electrostatic i.e. dispersion forces) with charged particles. The gelation induced by the addition of NaCl and $CaCl_2$ has therefore been the subject of several comparative studies. Ako et al. studied the effect of NaCl for different concentrations up to 1 M on the gelation of β-lactoglobulin aggregates of R_g = 65 nm at a concentration of 50 g/L and a temperature of 60°C and showed that increasing the NaCl concentration increased the gelation rate (Figure 1.11). The aggregate suspension gelled within 3 min after the addition of 1 M NaCl. Ako et al. concluded that the gel structure did not vary with the type of salt. Bryant and McClements [20] indicated that the rate of gelation and final gel strength increased with salt concentration and was greater for $CaCl_2$ than for NaCl at the same concentration, because the former was more effective at screening electrostatic interactions and can form ionic bridges. Also according to Bryant and McClements, increasing the salt concentration resulted in greater scouring of negatively charged whey protein aggregates, resulting in faster gelation and a stiffer gel structure." Similarly, Marangoni et al. (2000) stated that "the rate of aggregation in the presence of $CaCl_2$ is higher than in the presence of NaCl probably due to the cross-linking effect of Ca^{2+}. Marangoni et al. (2000) described $CaCl_2$-induced gelation as a two-step mechanism, rapid aggregation of larger

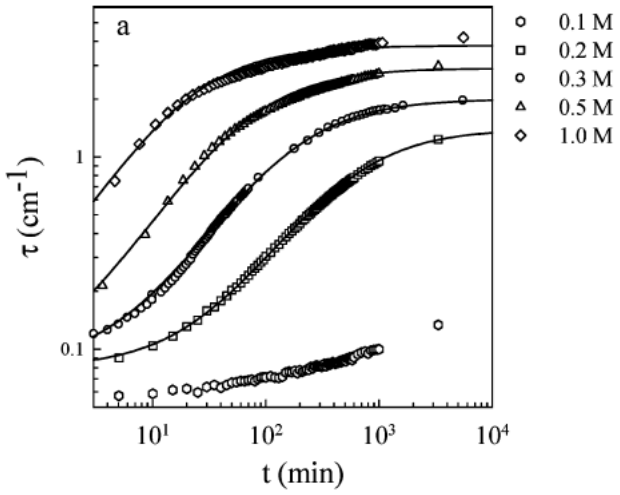

Figure 1.11: Evolution of turbidity of an aggregate suspension (R_g = 65 nm, concentration of 50 g/L) over time at T=60°C for different added NaCl concentrations.

.

aggregates, followed by slower aggregation of smaller ones and NaCl-induced gelation as a one-step mechanism.

The physical properties of salt-containing gels were strongly related to salt concentration. Hongsprabhas and Barbut [46, 47] showed that there was a concentration of $CaCl_2$ (30 mM) above which the young's modulus of the gel decreased for different protein concentrations. They hypothesized that the $CaCl_2$ concentration could modify the association/dissociation equilibrium of Ca^{2+} to proteins. Salt concentration would influence the structure and spatial organization of aggregates. At low salt concentrations, the low gelation rate would lead to the formation of solid, ordered gels with a filamentous microstructure. High concentrations of salts would lead to a faster formation of gel with a less ordered, more opaque and mechanically weaker structure [13, 46, 47]. Some authors nevertheless pointed out that the variable to be taken into account when analyzing the influence of $CaCl_2$ concentration and protein concentration was the molar ratio between $CaCl_2$ concentration and protein concentration because of specific interactions between calcium ions and proteins [55]. The divalence of calcium ions was thought to decrease the extent of electrostatic repulsions more effectively by charge screening, but calcium ions could also form ionic bridges between two COO^- carboxylic groups [46, 47]. However mechanisms such as local charge reversals were not assumed.

Several studies thus varied the protein concentration for a $CaCl_2$ concentration, thus investigating both the effect of protein concentration and molar ratio. It should also be noted that many studies apply a heat treatment during the gelation step induced by the addition of salts. The kinetics was thus shifted and the studied molar ratios were thus lower.

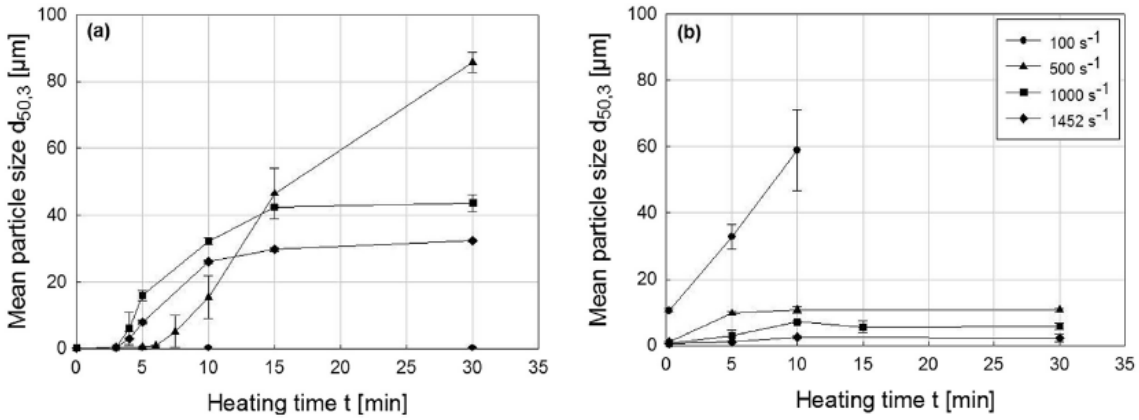

Figure 1.12: Evolution of aggregate size formed during 80°C heat treatment over time for different shear gradients for 5% (a) and 30% in WPC. Figure from Wolz et al. (2016), [136].

1.3 Aggregation processes

1.3.1 Effect of shear during aggregation

Since denaturation and thermal aggregation of whey proteins were mostly performed at the laboratory scale under static conditions, the effect of shear or more broadly of flow during aggregation has been little studied. Shear stresses can have different effects on the size and structure of proteins and aggregates. They can induce denaturation of proteins, break them or induce their aggregation [74, 78]. Due to the increased collision rate during shearing, increased aggregation can be achieved. However, at high shear rates, the encounter time between the particles was also reduced. The contact time would thus be insufficient to induce aggregation of the particles and they would therefore be more likely to remain as individual particles [147].

Wolz et al. [136] studied the influence of shear (100-1452 s^{-1}) and whey protein concentrate (WPC) concentration on aggregate size during aggregation at 80°C and showed that at low WPC concentration (5%), the aggregate size increased with shear (100-750 s^{-1}) after 5 min of heat treatment and then stabilized after 15 min for higher shear (750-1420 s^{-1}). On the other hand, at higher protein concentrations (30 %), the size of the aggregates decreased with shear. The increase in protein concentration accelerated the rate of denaturation and aggregation of proteins. When a shear gradient is imposed, the increase in viscosity induced an increase in shear stress. The increase in the denaturation and aggregation rate and the resulting increase in viscosity and shear stress would induce a decrease in the size of aggregates at high protein concentration.

Simmons et al. (2007) included the influence of temperature (70-90°C) to the effect of shear (111-625 s^{-1}) on whey protein aggregation. When the temperature was higher than 80°C, the aggregates formed were denser and more rigid due to the predominance of covalent disulfide bonds. They showed that the shear rate influenced the denaturation kinetics and the growth of the particles due to an increase

in the collision rate but concluded that the influence on the size remains complex to interpret.

Erabit et al. (2014) also studied the effect of shear(0-400 s^{-1}) on aggregation kinetics (0-240 s) for different temperatures (67-95°C) and showed that shear exerted an impact on the size distribution but not on the native residual fraction of proteins. Shear exerted an influence on the collision between aggregates larger than 1 μm.

1.3.2 Shaping by flow

Shaping of gelled spherical particles

Beyond the physico-chemical conditions and the thermal treatment, the process has been studied in order to open new ways of structuring the aggregation and gelation of proteins. The formation of spheres is interesting in problems of encapsulation of bioactive molecules and controlled release but also in problems of replacement of fats while maintaining a suitable texture. In the context of a flow, spheres can be generated in a T-shaped geometry, by coflow or in a stagnation point geometry. The spheres were generated between two immiscible fluids (a dispersing phase and a dispersed phase) and the control of their size was based on the viscosities of the phases and the flow rates imposed. Andoyo et al. [6] have thus formed gelled spheres of WPI up to 10 μm in diameter by heat treatment of spheres produced under flow.

Fiber shaping

The formation of elongated structures characterized by a fractal dimension equal to 1 and by a surface/volume ratio higher than that of spheres is interesting for applications of controlled release of bioactive molecules where one seeks to maximize the surface/volume ratio but also when one seeks to modulate the rheology of suspensions in particular and to increase the viscosity of the media [41], [145]. Fiber formation can be achieved by electrospinning [82], extrusion [108], but also by microfluidic processes [48], [49], [17]. Electrospinning produced continuous, long, ultra-fine fibers with diameters ranging from a few micrometers to a few nanometers, using an electric field. The formation of fibers usable in the food field was however limited by the use of additional chemicals that were potentially non-food or even toxic. An alternative for the application to the food field was the use of the extrusion process but the size of the produced fibers was of the order of the millimeter [108] and remained little adapted to the formation of fine fibers (tens or hundreds of micrometers).

Fiber formation by microfluidic processes relies on hydrodynamics and the use of co-flow. Bohomme et al. (2012) studied the formation of fibers under flow whose gelation relied on a diffusion reaction mechanism between calcium ions and alginate. Fiber formation in a Poiseuille flow depends on two joint conditions. The first condition is the shaping of the material by means of a laminar coflow between two Newtonian fluids in a cylindrical microfluidic geometry, governed by the laws of hydrodynamics. The use of a microfluidic device allows to properly control the flow and transport properties. The second key condition is the controlled solidification of

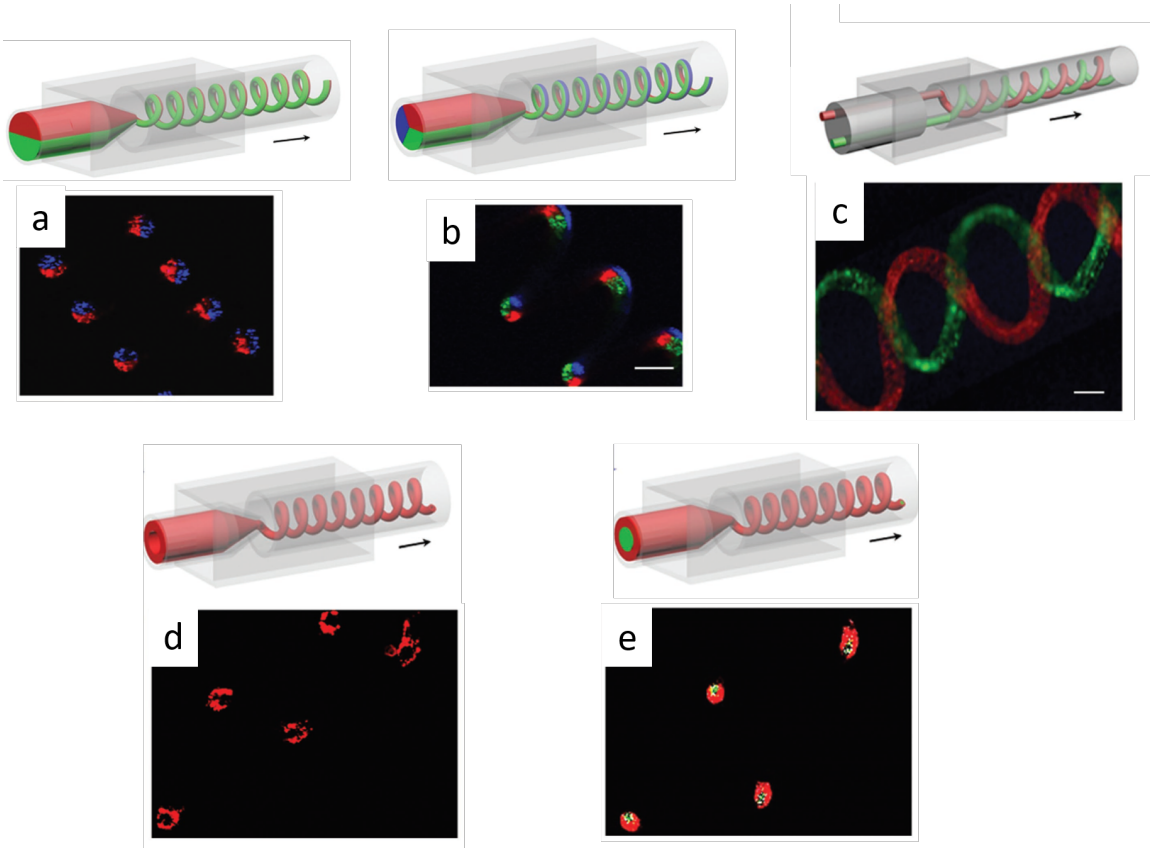

Figure 1.13: Schematics and microscopic images of helical fibers with a two-stranded (a), triple-stranded (b), double helix (c), hollow (d) and core-shell (e) structure. Figure from Yu et al. [138].

the internal jet during the flow by chemical reaction during the transverse molecular diffusion of calcium ions.

Hollow and solid fibers of different diameters were spun by simply manipulating the ratio of input rates from the same geometry [48]. The number of co-flow can be varied and fibers comprising multiple layers with hierarchical structures can be produced [25]. Yu et al. (2017) used a microfluidic coaxial capillary to form helical fibers with controllable length, diameter, and pitch of the helical micro-fibers by adjusting the flow rates. Due to the very high gelation rate, the formed helical fibers maintained the same cross-sectional structures as the injection flows, and adopted different types of structures such as a two-stranded helix, a three-stranded helix, a core-shell structure, and even a double helix (Figure 1.13).

Whey proteins can be used to form hydrogels, defined by a three-dimensional structure with the ability to swell and retain a significant fraction of water in its structure due to the presence of hydrophilic groups. Hydrogels have swelling and dissolving properties. These properties are interesting for applications of controlled release of encapsulated molecules of interest.

1.4 Objectives

In this literature review, we have summarized the main physico-chemical parameters that control the formation and structure of WPI aggregates and gels. In the framework of the industrial collaboration with the Nestlé Research Center (Lausanne) developed in this thesis, an important objective of this understanding was to be able to use protein aggregates as a natural food texturizer. While the physio-chemical pathways for the formation of milk protein aggregates have been extensively studied, the industrial process pathways such as the control of flow and thermal conditions have not yet been fully explored. These avenues are generally used in materials science to create new structures at microscopic scales, such as biopolymer fibers. Could microfluidic tools allow the creation of milk protein aggregates with improved texturing properties or even new functionalities?

The general objective of this thesis was to study new aggregation and gelation processes in order to produce new aggregate structures to improve their texturing capacity.

In view of the interesting rheological properties of fractal structures for the texturing of products, this thesis focused on the use of fractal aggregates. Several questions arise from this industrial problem and are studied in the following chapters.

Under industrial conditions, aggregates are formed at high temperatures in a continuous process. This process potentially offers new ways to control the aggregate structure through flow, residence time and heat exchange. The first objective of this thesis was therefore to study the influence of these parameters on the kinetics of aggregate formation and their resulting structure. A process of aggregation under flow was developed whose millifluidic scale allowed to decouple and study the effect of shear and aggregation temperature by neglecting the thermal gradients at high temperature (92°C) on the aggregation kinetics. The structural study was mainly performed by X-ray scattering at the ESRF in Grenoble on sub-micrometric aggregates which gave access to both the aggregate and the protein scale. The results are presented in Chapter refchap:3.

Still in an industrial context, it is much more advantageous to use fractal aggregates with a size greater than a hundred micrometers, in order to maximize their texturing rheological properties. Beyond that, the aggregates are perceived sensorially by the consumer. However, there are no dedicated techniques to characterize the structure of these aggregates. Radiation scattering techniques are limited to objects of the order of a few micrometers, at most. The second objective was therefore to develop a method to characterize the structure of aggregates based on quantitative fluorescence microscopy. In Chapter 4, we characterized the size, mass and density of aggregates for objects ranging in size from a few nanometers to a few hundred micrometers. In addition, these results provided important formulation leads for optimizing the texturing properties of the aggregates.

The third objective presented in Chapter 5 was to study an innovative structuring of fractal aggregates at the micrometer scale thanks to controlled flows and cold gelling mechanisms. The aggregates have been shaped into fibers of about 100 microns in diameter and several centimeters long. We studied in particular the formation and stability of these objects according to hydrodynamic and physico-chemical conditions. We thus obtained a new texturizing structure in the form of core-shell fibers from fractal aggregates. These fibers were also sensitive to physico-chemical conditions and can release their contents, thus giving them a controlled release functionality.

In order to understand the origin of the core-shell structure of the fibers, we presented in Chapter 6 an experimental approach in a simplified geometry aiming at quantifying the mechanisms coupling diffusion and cold reaction that took place during fiber formation.

Chapter 2

Materials and methods

Contents

2.1 Materials

Whey protein isolate Prolacta 95 (batch 30916B) was purchased from Lactalis Ingredients (Bourgbarré, France). The composition of the WPI (Nx6.38) was (in g/100g powder wet basis): protein 88.5 (of which β-lactoglobulin 65%, α-lactalbumin 20%, soluble caseins 10% and almost 5 % of bovine serum albumin and immunoglobulin, ash 1.9, moisture 5.6, carbohydrates 0.14, fat 0.5). The mineral composition was (g/100g powder wet basis): Ca 0.35, Mg 0.06, Na 0.15, K 0.35, P 0.21, Cl 0.01.

A WPI stock solution of 15% w/w was prepared by dispersing of the WPI powder into demineralized water (σ = 0.5-0.9 μS/cm, pH = 5.5-6.5). Sodium Azide (0.02% w/w, Sigma-Aldrich CAS 26628-22-8) was added to the solution to prevent bacterial growth and gently stirred for 12 hours at 4°C for complete dissolution of the WPI powder. The stock solution was either dialyzed against salt-free demineralized water containing 0.02 % w/w sodium azide or not dialyzed. The concentration of WPI solution was measured by UV absorption at 280 nm with an extinction coefficient of 1.02 L/g/cm. pH was adjusted at 7.0 by the addition of sodium hydroxyde (1M). Stock solution of NaCl was prepared at 1 M by dissolving the powder into demineralized water.

2.2 Denaturation and thermal aggregation of WPI

2.2.1 Static aggregation process

To induce denaturation and subsequent aggregation of native WPI, a heat treatment is performed. After adjustment of WPI and salt to desired values and adjustment to a neutral pH value, 10 mL pyrex test tubes (10 cm height and 1.6 cm diameter) are filled with the protein solution under nitrogen flow until the edge of the tube to prevent thiol oxydation. The test tubes are immersed in a water bath with the temperature set at 92°C or 80°C and left for variable times. Once the holding time is complete, test tubes are immersed in a ice bath and allowed to cool down at 4°C for further analysis. Aggregate suspensions are then filtrated with a 5 μm pore size filter to remove any oxidized film. They are kept at 4°C and used within the week for analysis. During the test tube aggregation process, thermal establishment time depends on the characteristic length of the tube and on the thermal gradient between the water batch and the WPI solution. Natural convection is the dominant shear parameter during test tube aggregation process.

2.2.2 Millifluidic aggregation process under flow

A millifluidic continuous aggregation process has been designed to aggregate WPI solutions and decrease the characteristic time of heat transfer, so that aggregation occurred in isothermal conditions (Figure). This set-up allowed us to study the effects of the mean residence time t of WPI in the tube and the mean shear rate $\dot{\gamma}$ on the aggregation process. This section was further detailed in chapter 4, in

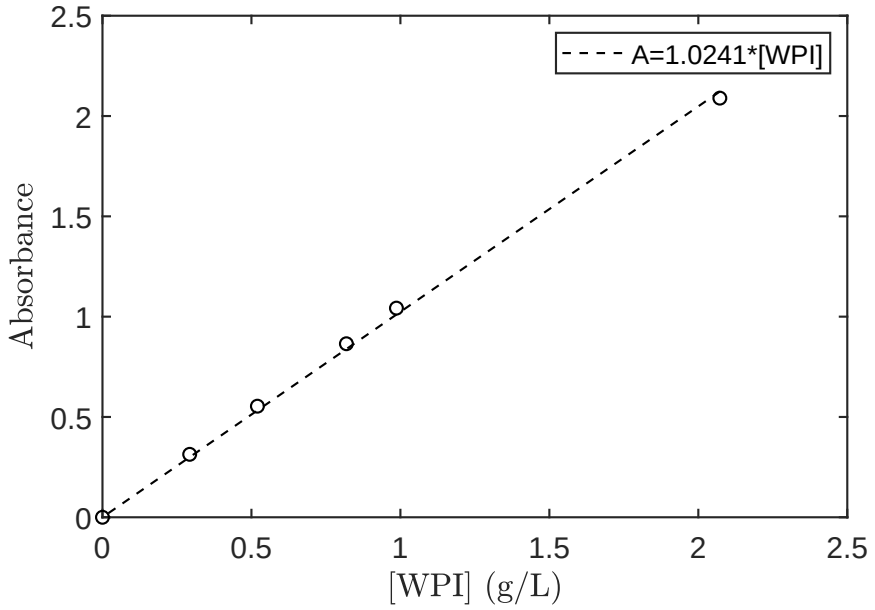

Figure 2.1: Absorbance measured at $\lambda = 280$ nm, for different WPI concentrations

the Millifluidic continuous aggregation process section. Aggregates were collected in small tubes, immersed in a ice bath and kept at 4°C until analysis.

2.3 Characterization of native WPI solutions

2.3.1 Determination of native protein concentration

The protein concentration of a native WPI solution was determined by UV absorption at $\lambda = 280$ nm using a spectrophotometer (UVmini-1240 spectrophotometer, SHIMADZU). A calibration curve was performed on a range of concentrations of native WPI solutions (0-2 g/L), prepared from the WPI powder (Figure 2.1). A blank measurement is performed on water prior each measurement. The molar extinction coefficient ϵ of the calibration curve was determined according to the Beer-Lambert law

$$A = \epsilon \times l \times C \tag{2.1}$$

with l the thickness of the quartz cell used (cm), C the protein concentration (g/L). Thus *epsilon* = 1.0241 L/g/cm is determined. Any native WPI solution is diluted to a concentration of C = 1 g/L prior to measurement by UV absorption in order to be within the range of the calibration curve.

2.3.2 Determination of the residual fraction of native proteins after aggregation

Determining the fraction of residual native protein after aggregation allows the determination of the aggregation reaction advancement. For whey proteins, thermal denaturation results in a decrease in solubility at pH 4.6 ([34]). By adjusting the pH of a suspension of WPI aggregates to 4.6 with 0.1M HCl and centrifuging for 20 min at 20.000 g, aggregated and denatured proteins sediment and the residual native proteins remain in the supernatant. The supernatant is then collected and its protein concentration, $C_{residual}$, measured by UV absorption, as described above. The initial native WPI concentration, C_{native} is determined prior aggregation using the same procedure of pH adjustment.

2.3.3 State diagram

The combined effect of protein concentration and salt concentration was studied at neutral pH in order to delimit the areas of formation of stable suspensions of aggregates from the areas of gelation when submitted to a heat treatment during the test tube aggregation process. Un-dialyzed native WPI solutions were used for the establishment of the state diagram. The concentration of NaCl is therefore indicated as an added concentration, independent of the composition of the powder. WPI concentration was varied from 4% w/w to 10% w/w and NaCl concentration was varied from 0 mM to 80 mM. WPI solutions were heated at 92°C from 30 min to 60 min. The WPI gelation concentration, indicated by the red symbols, decreases with increasing NaCl concentration (Figure 5.1) and we note an effect of the heating time on C_g for protein concentration below 6% w/w were aggregation rate is a function of protein concentration.

2.4 Structural characterization of WPI aggregates

2.4.1 Light diffusion

Light scattering is a non-destructive characterisation technique for colloidal solutions, based on the analysis of the interaction between a monochromatic light wave and the solution under study. Local information is obtained on the scale of the wavelength used. Light scattering and X-ray scattering are therefore similar, except for the difference in scale probed.

Small angle X-ray scattering

Principle Small angle X-ray scattering (SAXS) is a non-destructive small angle scattering technique using a monochromatic X-ray source, where the elastic scattering of X-rays, by the constituent electrons of a sample that exhibits inhomogeneities in the nano range, is recorded at very low angles (0.1 - 10°)

This technique is used to study the structural properties of materials on a scale of 1 to 100 nm and to determine the average quantities that characterise their size, shape and interactions. As any scattering process is characterised by a reciprocity law that gives an inverse relationship between object size and scattering angle, the sizes of particles or structures that can be resolved can be extended on both sides by measuring at smaller (ultra-small angle X-ray scattering, USAXS) or larger (wide angle X-ray scattering, WAXS) angles than the typical 0.1° to 10° of SAXS. When subjected to X-rays, the so-called soft matter scatters a part of the incident radiation of wave vector k and wavelength λ, with a small deflection (at small angles, typically between 0.1 and 10°).

This incident beam forms a scattering angle 2θ with the scattered beam k'. The characteristic scale at which the sample heterogeneity is probed by the radiation is defined by the modulus q of the scattering wave vector and is, typically, 1/q, with $q = 2k sin\theta = \frac{4\pi}{\lambda} \sin\theta$. The scattered intensity is collected on a two-dimensional detector, placed perpendicularly and at a variable distance from the sample, in the centre of which is placed a beamstop preventing the transmission of the direct beam.

Random orientation of the particles in solution leads to an isotropic scattering spectrum, where the intensity is constant for each value of the angle θ. The variation of the intensity of the deflected beam as a function of the scattering angle will depend on the global and internal structure of the molecule but also on the intermolecular interactions. To increase the signal to noise ratio, the intensity is averaged for each value of θ (radial integration) and a spectrum is obtained representing the intensity variations I as a function of the wave vector q. The scattered intensity of a solution is defined as :

$$I(q) = n \triangle \rho^2 V^2 P(q) S(q) \tag{2.2}$$

with n being the number density of the particles, where n = N/V, N being the number of particles in a volume V, $\triangle \rho$ the difference in electron density between the solvent and the particles, V the volume of a particle, P(q) being the form factor and S(q) the structure factor. The form factor describes the structure of the particles. The structure factor describes the diffusion interference between the particles and describes the types of interactions between the particles. For dilute solutions where the particles are spaced far enough from each other not to interact, the structure factor is equal to 1. The total scattering intensity is then the sum of the scattering of each particle:

$$I(q) = nP(q) \tag{2.3}$$

The scattered intensity is thus proportional to the particle concentration. It will then be appropriate to place oneself in a dilution range for which the scattered intensity is directly proportional to the form factor and the particle concentration.

Device and procotole The SAXS experiments were conducted at the ESRF (Grenoble), on the ID02 beamline, providing an energy of 12.46 keV and a wave vector range q from 3×10^{-3} to 4 nm^{-1}. The scattering spectra were obtained for a

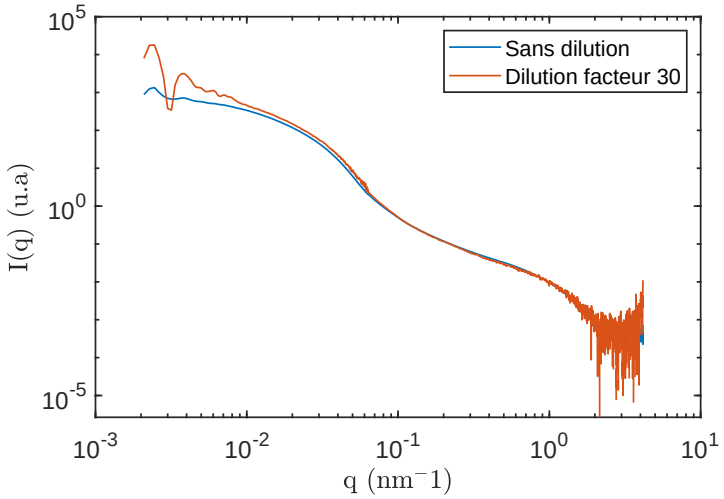

Figure 2.2: Diffusion spectra of a 4% w/w 10mM NaCl pH 7.0 WPI solution aggregated under flow during 60 s at 92°C, undiluted and diluted 30 times before SAXS measurement.

distance d = 30 m and d = 2 m between the sample and the detector. The samples were analyzed in static conditions in a 2 nm diameter glass capillary, which was the same for all measurements to minimize background variations. In order to minimize X-ray damage to the sample, the exposure time was fixed at 0.5 s and the filling of the capillary was controlled by a syringe pump that moved the sample after each acquisition. For each sample, the spectrum of the water contained in the capillary was acquired as well as the acquisition of four spectra for the same sample. The final spectrum of the particles contained in the sample was obtained by averaging the four spectra of the sample and subtracting the spectrum of the solvent.

For each sample, several dilutions were performed in order to find the appropriate dilution range, allowing the scattered intensity to be assimilated to the form factor and thus neglecting the structure factor. The dilutions were performed with demineralized water. Several spectra of different dilutions were made and their scattering intensity were plotted as a function of q (Figure 2.2). By multiplying the spectrum of the diluted dilution by its dilution factor we deduced that linearity between the scattered intensity and the concentration is obtained without dilution, in the full range of wave vectors studied. The decrease of the scattered intensity at low q for the spectrum of the thirty times diluted solution is due to the background subtraction. The scattered intensity can therefore be assimilated to the form factor.

Results and analyse The particles studied are WPI fractal aggregates, characterized by the repetition of the same geometrical pattern at all scales. A mass fractal aggregate is thus constituted of primary particles grouped in primary units, forming ramifications and reticulations and creating a tridimensional network (Fig.1.5).

The Guinier regime is defined in the low wave vector range for $R_g q \ll 1$ (Figure 2.3 (b) I). In the range of intermediate wave vectors the scattered intensity is expressed

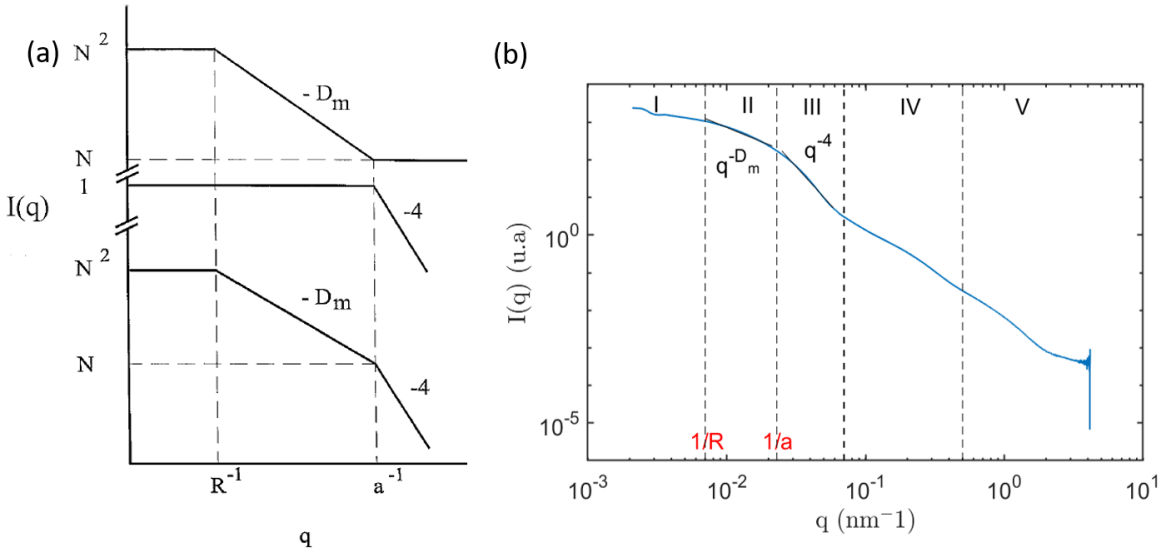

Figure 2.3: *a:* Scattering intensity of a fractal aggregate of radius R, of fractal dimension D_m and with a radius of elementary units a. From top to bottom, scattering spectrum of a fractal aggregate, of a sphere, of the product of both. Figure and notation from [120]. *b:* Scattering intensity of a solution of fractal aggregates of WPI of radius R, consisting of spherical elementary units a.

as a power law and is related to the fractal structure of the aggregate (Figure 2.3 (b) II). We define as the Porod regime the range of large wave vectors (Figure 2.3 (b) III) for which the scattered intensity follows a power law in q^-4 in the case of spherical particles. This decay of scattered intensity in q^-4 signs a variation of scattering length located at the interface between particle and solvent [84]. The exponent of this power law can be used to understand the shape of the particles (spheres, rods or flat plates), as well as whether the interface between the particles and the surrounding environment is sharp or diffuse. Different power laws over ranges of wave vectors thus indicate a change in structure at different scales. In order to quantitatively analyze the structure of objects at different scales, adapted representations of the Guinier regime, the Porod regime as well as the Kratky representation at very large q (Figure 2.3 (b) V) will be realized. We will detail them below.

Guinier regime: determination of the size of the aggregates

In the case of a dilute system consisting of randomly oriented particles of similar sizes, the particle size can be determined. In the Guinier regime (regime I, Figure 2.3), at the smallest angles ($R_g q \ll 1$), the scattering curve of particles in dilute solution can be approximated by the following relation

$$I(q) = \frac{I(0)}{1 + q^2 R_g^2/3} \tag{2.4}$$

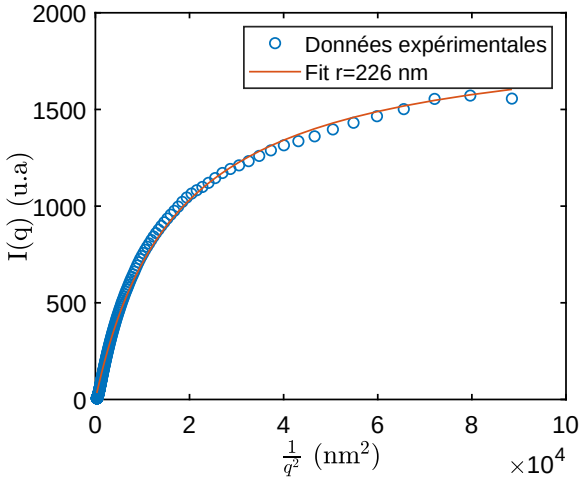

Figure 2.4: Determination of the radius of gyration and $I(0)$ by a least squares fit performed on a 4% w/w 10mM NaCl pH7.0 WPI solution aggregated under flow for 15 min at 92°C

With R_g, the radius of gyration defined as

$$R_g = \sqrt{\frac{\sum_{i=0}^{\infty} m_i(r_i - r_c m)^2}{\sum_{i=0}^{\infty} m_i}} \tag{2.5}$$

where $r_c m$ is the position of the center of mass, r_i is the position of the atom i and m_i its mass. The radius of gyration is defined as analogous to the radius of inertia in mechanics with the difference that here the electrons replace the mass element of the latter.

And with $I(0)$, the scattered intensity extrapolated to the zero angle is defined as

$$I(0) = n(V \triangle \rho)^2 C_{ag} M_w \tag{2.6}$$

with C_{ag} the mass concentration of aggregated proteins, M_w the molar mass. It appears that the value of I(0) is particularly sensitive to the volume of the particles.

$I(0)$ and R_g are obtained by a least-squares fit of I as a function of $1/q^2$ (Fig.2.4).

Since the mass concentration of the aggregated proteins is unknown, the molar mass cannot be deduced from the value of I(0) determined by the fit. We will present later an experimental technique to access the protein mass of the aggregated particles.

Porod regime

In the Porod regime, the decay of the signal in q^{-4} is a characteristic signature of the presence of sharp interfaces in the system [84]. A representation of the Porod regime in $q^{-4}I(q) vs. q$ makes the 1/a scale oscillations visible.

Monitoring of protein conformational changes: Kratky plot

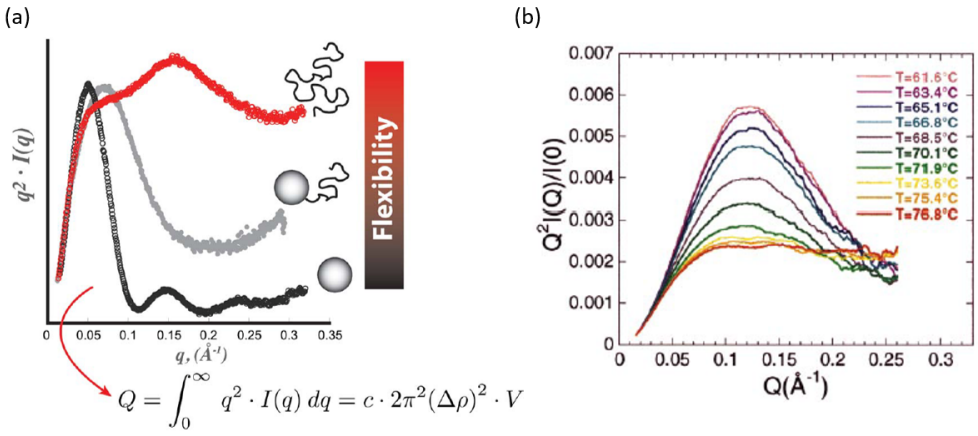

Figure 2.5: *a: Representation q^2I vs q illustrating the variations of the curves for spherical, partially folded and fully unfolded particles. Figure from [105] b: q^2I vs q representation of neocarzinostatin for different temperatures. Figure taken from [93]*

The range of very large q probes the structure of the primary particles composing the aggregate, here the proteins. The Kratky representation: q^2I *vs* q gives access to the folding/unfolding state of the primary particles. This representation allows to follow conformational changes or to highlight qualitatively the existence of disordered domains [63], [105]. A bell-shaped curve indicates a globular conformation of the proteins (Figure 2.5 (a)) and the decrease in peak intensity reflects the unfolding of the proteins during thermal denaturation (Figure 2.5 (b)). Thanks to this feature and the fact that the form factor is a linear combination of the form factors of the different states of the protein in solution (native, unfolded, and aggregated), it is possible to quantitatively follow the denaturation kinetics of the proteins.

We will present here this method, used for the quantitative monitoring of the denaturation kinetics of a solution of aggregated proteins at 4% 10 mM NaCl pH7.0 at 92°C for 15 minutes from the Kratky representation (Figure 2.8).

We make the assumption and consider that at this temperature, the species present in solution at each time t are the native proteins and the aggregated proteins. This assumption will be validated later. We can thus express the form factor at each time t of aggregation as a linear combination of the form factors of an initial solution of native ($I_{nat}(q)$ at $t = 0$ min) and final aggregated proteins ($I_f(q)$ at $t = 915$ s)

$$I(t,q) = \alpha(t) I_{\text{nat}}(q) + [1 - \alpha(t)]\, I_{ag}(q) \tag{2.7}$$

with $\alpha(t) = C_{nat}(t)/C_0$. Determination of the fraction of residual native protein contained in the final aggregated protein solution ($t = 915s$) by the acid precipitation test allows to write $I_f = 0.95 I_{ag} + 0.05 I_{\text{nat}}$. Hence

$$I(t,q) = \alpha(t) I_{\text{nat}}(q) + \frac{1 - \alpha(t)}{0.95}(I_f(q) - 0.05 I_{nat}(q)) \tag{2.8}$$

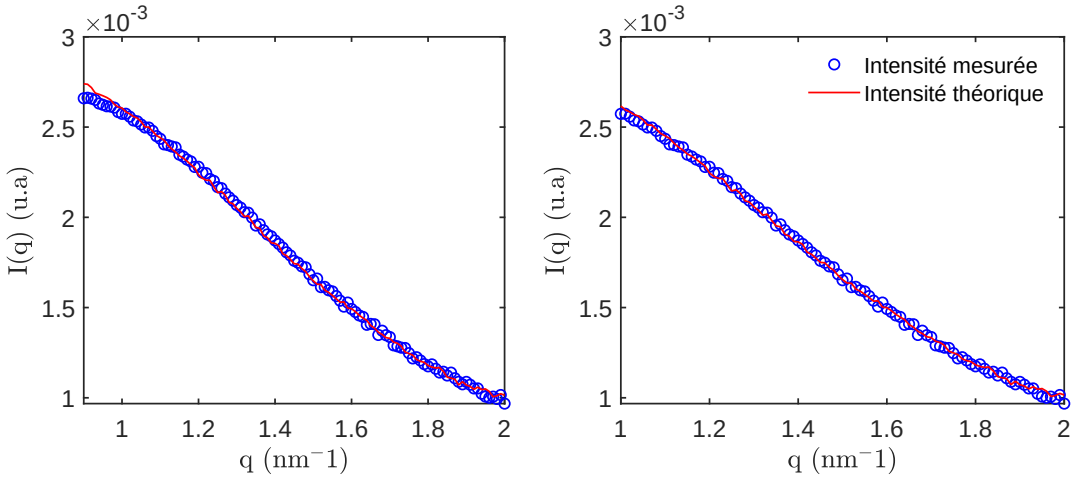

Figure 2.6: Experimental and theoretical scattered intensity plotted over two ranges of wavevectors for t = 180 s. The theoretical intensity is calculated from the equation 2.8 with α minimizing E over the respective q ranges.

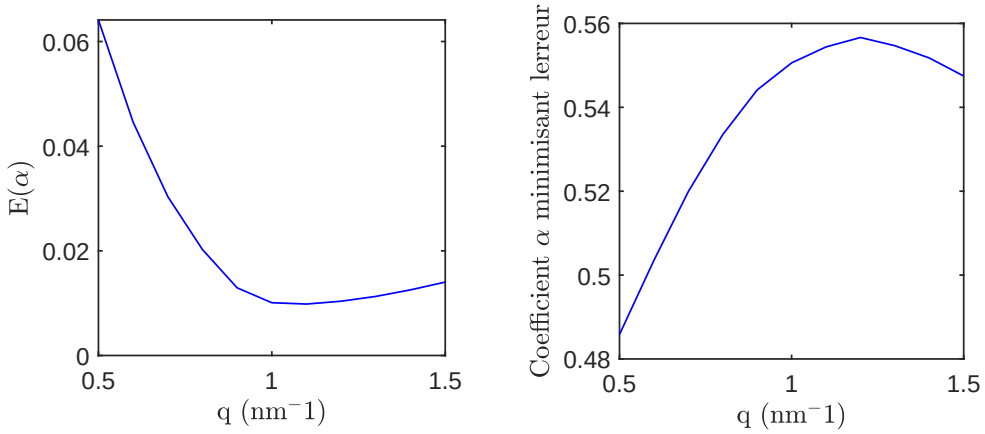

Figure 2.7: *Left*: Computed error for different q_{min} values. *Right*: Coefficient α minimizing the calculated error for different q_{min} values.

$$E(\alpha) = \sqrt{\frac{\sum_q (I_{exp}(t,q) - I(t,q))^2}{\sum_q I_{exp}(t,q)^2}} \tag{2.9}$$

It will be a matter of finding the range of wave vector over which this linear regression is verified. According to the figure 2.8 (a) it is possible to make a first estimation of this range of wave vector between 0.5 and 2. Linear regression will be performed on different wave vector ranges, whose minimum value q_{min} varies from 0.5 nm^{-1} to 1.5 nm^{-1} with a step of 0.1, up to 2 nm^{-1}. Figure 2.6, for $t = 180$ s, the experimental scattered intensity, as well as the theoretical scattered intensity calculated from the equation 2.8, are plotted for two ranges of wave vector, starting respectively at 0.9 nm^{-1} and 1 nm^{-1} and going up to 2 nm^{-1}.

The coefficient α is calculated to minimize the error on the linear regression

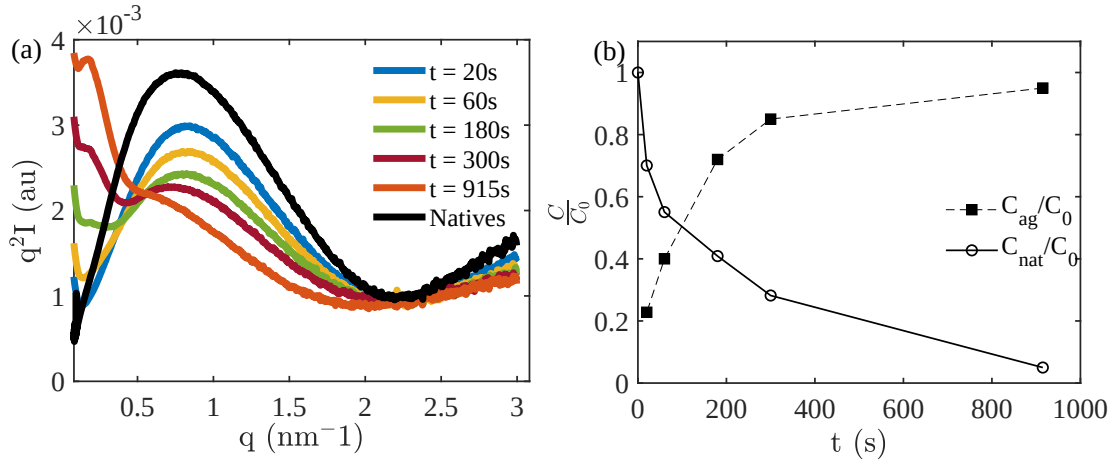

Figure 2.8: a : q^2I *vs* q for different aggregation times (t = 0 s to t = 915 s) of a 4% w/w 10mM NaCl pH7.0 aggregated WPI solution at 92°C. b : Residual fraction of native proteins during aggregation, calculated over the range 1-2 nm^{-1}

(Equation 2.8 and 2.9) for each range of wavevectors probed (Figure 2.7). The decay of the calculated intensity for values of $q_{min} < 1\ nm^{-1}$ (Figure 2.6) shows us that the range of wavevectors over which to perform the linear regression starts at 1 nm^{-1}. Figure 2.7, the error on the linear regression is minimized for a coefficient α computed over a wave vector range starting at $q_{min} = 1\ nm^{-1}$.

We can thus express the form factor at each time t of aggregation as a linear combination of the form factors of an initial solution of native ($I_{native}(q)$ at $t = 0$ min) and final aggregated proteins ($I_{final}(q)$ at $t = 915s$) over 1 - 2 nm^{-1} and thus plot $\alpha(t) = C_{native}(t)/C_0$ (Figure 2.8).

Let us return to the starting hypothesis, according to which the species present in solution at each time t are the native proteins and the aggregated proteins. In order to validate this hypothesis, we will follow the kinetics of aggregation from the intensity $I(0)(t)$, proportional to the concentration of aggregated proteins $C_{ag}(t)$ according to 2.6, knowing that M_w is constant (result demonstrated in Chapter 3)

$$\frac{C_{\mathrm{ag}}(t)}{C_0} = 0.95\frac{I(0)(t)}{I(0)(t = 915s)}. \tag{2.10}$$

$C_{ag}(t)/C_0$ is thus computed independently of $C_{native}(t)/C_0$, because it is computed over a different range of wave vectors. At each time t, $(C_{\mathrm{ag}}(t) + C_{\mathrm{nat}}(t))/C_0 = 1 \pm 0.15$ (Figure 2.8). The denaturation rate is thus equal to the aggregation rate.

2.4.2 Resonant mass measurement

The Archimedes device (Malverne) is based on the resonant mass measurement technique (RMM). Each particle is detected, quantified and characterized (size and mass). The device measures masses of at least 4.5 10^{-16}g and calculates particle sizes be-

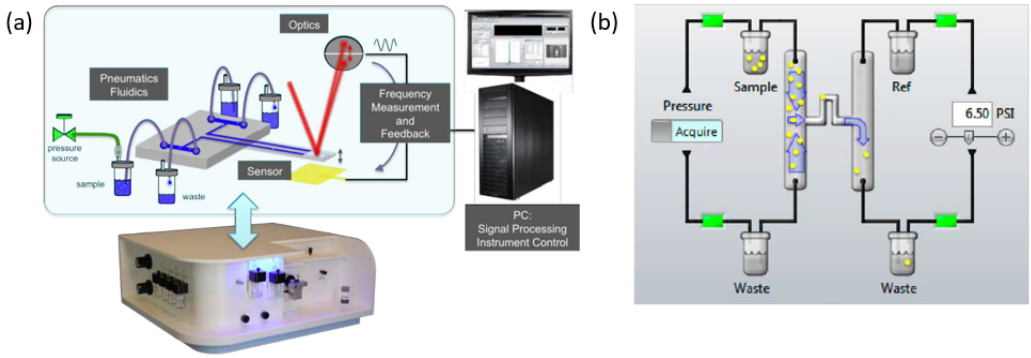

Figure 2.9: *(a)* : Schematic diagram of the Archimedes and the resonant mass measurement technique. *(b)* : Characterization of each particle contained in the sample passing through the micro cantilever.

tween 50 nm - 5 μm. The mass measurement of the Archimedes thus makes it possible to overcome the small angle X-ray scattering which did not allow us to have access to it, the concentration of aggregated proteins being unknown.

The measuring device is equipped with a MEMS (Micro Electro-Mechanical Systems) sensor composed of a microfluidic circuit at the heart of which is implanted a micro cantilever, whose resonance frequency is calibrated (2.9 (a)). A very diluted solution of particles is injected into the microfluidic circuit by applying a pressure difference between the sample and the reference sample (D_2O) characterized by a fluid density lower than that of the sample containing the particles (2.9 (b)).

Each time a particle passes through the micro cantilever, the resonance frequency varies according to the mass of the particle. The variation of the resonance frequency is analyzed after transformation into an electrical signal by the joint action of a laser focused on the sensor and a photodetector. The buoyant mass (M_B) is proportional to the variation of the resonance frequency $\triangle f$:

$$M_B = \triangle f S \tag{2.11}$$

with S the calibration constant (mHz/fg) of the micro cantilever determined during the calibration procedure. The conversion from buoyant mass to mass (M_w) involves the protein density ρ_{WPI} (1.32 g/mL) and the fluid density (rho_f) [135].

$$M_w = \frac{M_B}{1 - \frac{\rho_f}{\rho_{WPI}}} \tag{2.12}$$

A calibration of the MEMS sensor is performed before each set of measurements on a calibrated solution of latex particles. A detection limit is set to establish the minimum detection value of the particles. Decreasing the detection limit increases the sensitivity of the measurement to small sizes, but may also increase the noise of the measurement. The detection limit is set at 0.04 in order to optimize the measurement. A few thousand aggregates are analyzed per sample and allow the establishment of a probability density function of the mass of the aggregates weighted by their mass (Figure 2.10).

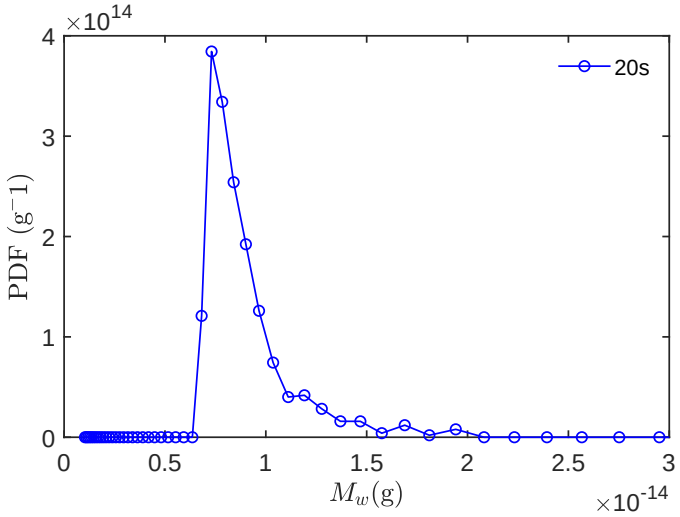

Figure 2.10: Mass-weighted probability density of aggregates. Solution of aggregated proteins at 4% 10 mM NaCl pH7.0 under flow for 20 s at 92°C under an average shear of 32 s^{-}1.

Chapter 3

Kinetic and structural characterization of whey protein aggregation in a millifluidic continuous process

In industrial conditions, WPI aggregates are obtained in continuous processes at high temperature ($\geq 75°C$) in few minutes. When studying the kinetics of WPI aggregation at high temperature and under flow, one major issue is to develop a process in which heat transfer does not limit aggregation. To this end, we used a down-scaling approach in which a WPI solution flows in a heated capillary tube. The kinetics of aggregation and the structure of aggregates was characterized by resonant mass measurement and small-angle X-ray scattering. We discuss the effects of shear, temperature on aggregates structure and their kinetics of formation.
This chapter has been published in Food Hydrocolloids [132].

Contents

3.1 Introduction

Whey protein isolates (WPI) are of interest because of their nutritional and functional properties in food applications. Heat-induced aggregation coupled with the process conditions of whey proteins gives them new functional properties that can be used to impart the specific structural and physical properties of food products. Therefore, a thorough understanding and control of the aggregation process is required in order to design specific functional whey protein aggregates. The heat-induced aggregation process of whey protein (WP) is a complex multi-stage process but despite numerous studies, there are still many open questions that have not yet been resolved. [30, 80, 89].

The rate of denaturation and aggregation of WPI depends on several factors such as pH, ionic strength, concentration and temperature. The measurement of apparent reaction rates of β-lactoglobulin and α-lactalbumin denaturation (the major component of WPI) on a wide range of temperature (70 - 150 °C) showed an abrupt change of the rate constant at 90 and 80°C, respectively [28]. Subsequent studies have found that the overall aggregation process was limited by unfolding at low temperature (< 85°C) and aggregation reaction was the rate limiting step in the upper temperature range (> 100°C) [121, 130]. Beyond kinetics studies, conformational changes of WPI have also been investigated to explain the rates of denaturation and aggregation [32, 106]. While most of these studies did not make a distinction between unfolding limited from nucleation limited reaction, general mechanistic descriptions of heat-induced aggregation of WPI recognize an initiation, a propagation and a termination step [109, 127] by analogy with polymer radical chemistry [83, 107]. More specifically, heat-induced aggregation of WPI involves the reversible self-association of two or more "reactive" monomers to form reversible non-native oligomers. The unfolding of these chains creates the smallest net irreversible aggregate, the nuclei, from which aggregates grow by covalent and/or noncovalent interactions and condensate. One main limitation of the kinetics studies cited above is that they based their analysis on the consumption of native proteins undergoing aggregation in order to measure the global kinetics constant, whereas it would also be valuable to measure the concentration of aggregated proteins to precisely determine the mechanism which limits the reaction. In this regard, X-ray scattering techniques can be used to simultaneously follow the concentration of native and aggregated proteins [94] and also to gain insight on the structural properties of the aggregates [81].

The structure of aggregates can be modulated by varying the balance between repulsive / attractive forces [89, 148]. One striking feature is the transition from fibrillar aggregates to microgels and fractal aggregates by changing the pH from 2.0 to 7.0 [56]. The relationships of structural parameters of fractal aggregates with physico-chemical conditions and heat-treament have been well studied in regime of low temperature. Below 85°C, aggregation is limited by unfolding and takes place over several hours [69, 89, 148]. According to [69], the structure of fractal aggregates is independent of the concentration of β-lactoglobulin and the effect of the temperature is purely kinetic in the range 60 - 87°C. [148] studied the effect of pH and holding time on the formation of thermally-induced β-lactoglobulin aggregates at 80°C and

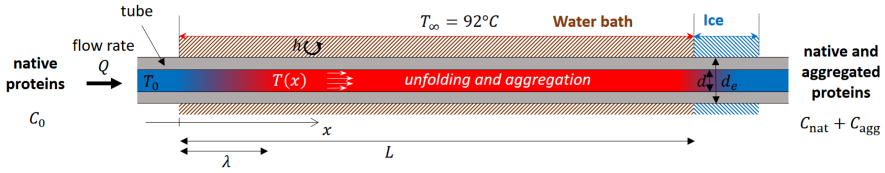

Figure 3.1: Diagram of the millifluidic continuous aggregation process. WPI solution flowed in 0.81 mm internal diameter tube at a flow rate Q and a temperature T_0. The tube was immersed in a heated water bath at temperature T_∞. From the time the tube was immersed ($x = 0$), the fluid temperature quickly rose along a characteristic length λ. The mean residence time t is directly proportional to the length L of the tube.

showed that the size of the aggregates saturated for a holding time ranging from 50 to 200 s, depending on the pH (6.0 - 6.8). However, these conditions are far from most industrial processes, in which a high temperature-short time UHT treatment is applied, reaching close to 140°C, and aggregation takes place over a few tens of seconds [35]. This rather fast aggregation is naturally combined with heat transfer in cases aggregation occurred in large-sized containers, such as batch reactors or test tubes. A simple way to increase the rate of heat transfer is to reduce the characteristic size of the sample down to the millimeter scale or below, as in a millifluidic continuous process [28]. Coupling this kind of set-up with X-ray scattering techniques should also give us new insights into the kinetics of native and aggregated proteins, for example on the change of structural properties of the aggregates with the heating time. This kind of continuous process of aggregation also offers an extra control parameter, which is the flow rate. It has been reported that the shear rate could affect the final aggregate size [29, 115, 121, 136], but this control parameter has not been widely studied and conclusions are conflicting.

Our objective was to study the kinetics of growth of WPI (4% w/w, 10 mM NaCl) at high temperature (92°C) in a regime which should correspond to the transition between unfolding limited and aggregation-limited reactions [28, 30]. Structural characterizations were done by X-ray scattering and resonant mass measurement and also covered the length scales of both the aggregates and the proteins. Both methods gave us complementary insights about aggregation and unfolding mechanisms. In the same way as [28] determined reaction rates of WPI at high temperature, we used a millifluidic continuous process to maximise the rates of heat transfer. This approach allowed us to accurately control the residence time, temperature history and shear rate.

3.2 Materials and methods

3.2.1 Materials and sample preparation

Whey protein isolate Prolacta 95 (batch 30916B) was purchased from Lactalis Ingredients (Bourgbarré, France). The composition of the WPI (Nx6.38) was (in g/100g

powder wet basis): protein 88.5 (of which β-lacotglobulin 65%, α-lactalbumin 20%, soluble caseins 10% and almost 5 % of bovine serum albimin and immunoglobulin, ash 1.9, moisture 5.6, carbohydrates 0.14, fat 0.5). The mineral composition was (g/100g powder wet basis): Ca 0.35, Mg 0.06, Na 0.15, K 0.35, P 0.21, Cl 0.01.

WPI stock solution of 10% w/w was prepared by dispersing of the WPI powder in deionised water. Sodium Azide (0.02% w/w, Sigma-Aldrich CAS 26628-22-8) was added to the solution to prevent bacterial growth and gently stirred for 12 hours for complete dissolution of WPI powder. The stock solution was then dialyzed against salt-free deionised water containing 0.02 % w/w sodium azide. The concentration of the dialyzed solution of WPI was measured by UV absorption at 280 nm with an extinction coefficient of 1.186 L/g/cm. Finally, deionised water and sodium chloride was added to obtain a 4 % w/w WPI solution with an ionic strength of 10 mM, and pH was adjusted at 7.0 by the addition of sodium hydroxyde (1M).

3.2.2 Millifluidic continuous aggregation process

A continuous small scale process was designed to aggregate WPI solutions and decrease the characteristic time of heat transfer, so that aggregation occurred in isothermal conditions. The setup is presented in Fig. 3.1. WPI solution was injected at a constant flow rate Q with a syringe pump (low pressure neMESYS, Cetoni GmbH) at 22°C through a PTFE tube of internal and external diameter $d_i = 0.81$ mm (or $d = 0.25$ mm for the largest shear rates investigated, concerning the data displayed in Fig. 3.6) and $d_e = 1.59$ mm, respectively. The tube was immersed in a stirred and heated water bath at temperature T_∞ and fixed at 92°C for the entire study. The aggregates were collected for a few minutes in a tube immersed in ice and kept at 4°C until analysis.

We studied the effects of the mean residence time t of WPI in the tube and the mean shear rate $\dot{\gamma}$ on the aggregation process. Both parameters were varied by changing the tube length L and the flow rate Q. They are defined by

$$t = \frac{\pi d^2 L}{4Q} \tag{3.1}$$

$$\dot{\gamma} = \frac{64}{3\pi}\frac{Q}{d^3} \tag{3.2}$$

We investigated variations of t and $\dot{\gamma}$ from 20 s to 15 min and from 53 to 2666 s^{-1}. Consequently, Q and L ranged from 15 to 150 mL/h and 16.2 to 750 cm, respectively (d= 0.81 or 0.25 mm). The exact experimental conditions are given in the key of each figure. The flow was assumed to be laminar given that the range of Reynolds numbers, $Re = du/\nu$ was between 20.7 and 207, where $\nu = 3.2\times10^{-7}$ m^2/s the kinematic viscosity of water at 92°C and $u = 4Q/\pi d^2$ the mean velocity in the tube.

The range of Peclet numbers investigated was always larger than 10^3. Thus, the effective diffusion coefficient of proteins along the longitudinal axis of the tube was greater than the molecular coefficient because of the parabolic velocity profile (i.e. Taylor-Aris dispersion, [7, 27, 124]), and we expect a dispersion of the residence time

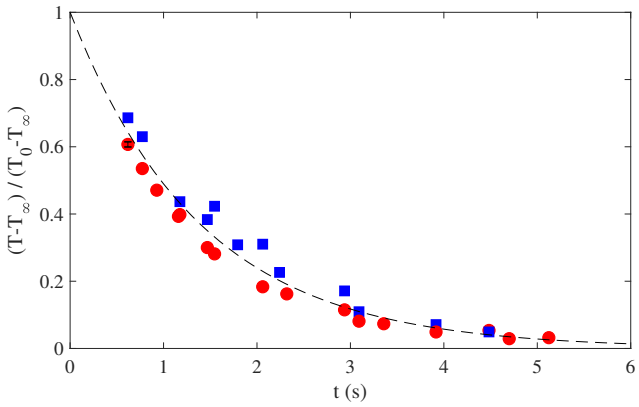

Figure 3.2: Reduced temperature $(T - T_\infty) / (T_0 - T_\infty)$ as a function of the residence time t (Eq. 3.5) in a tube of 0.81 mm internal diameter for various Q (60 to 300 mL/h) and L (10 to 30 cm). The temperature of the water bath, T_∞, was set at 80°C (squares) and 90°C (circles). The dashed line is the fit of Eq. 3.4 with the thermal characteristic time $\tau = 1.30$ s (Eq. 3.5) that is independent of Q.

of the proteins around the mean value t. Based on the scaling laws of [23, 24] and Latini and Bernoff [68], we estimated that the standard deviation of the residence time ranged between ±11 s and ±3 min for mean residence times t of 20 s and 15 min, respectively.

The rate of heat transfer is of crucial importance in order to study aggregation at short times scales. A simple heat balance on an elementary volume of the liquid makes it possible to relate the temperature gradient along the tube length to the global heat transfer coefficient h accounting for internal and external convection as well as heat conduction through the tube walls. The mean temperature T at abscissa x from the point where the tube was immersed is given by

$$\frac{T(x) - T_\infty}{T_0 - T_\infty} = \exp\left(-\frac{x}{\lambda}\right), \tag{3.3}$$

where $\lambda = \frac{\rho c_p Q}{\pi d h}$ is the thermal entrance length and ρ and c_p are the density and specific heat of the aqueous solution. By substituting Eq. 1 in Eq. 3 with $x = L$, T can be expressed as a function of the residence time t

$$\frac{T(t) - T_\infty}{T_0 - T_\infty} = \exp\left(-\frac{t}{\tau}\right), \tag{3.4}$$

where the thermal characteristic time τ is given by

$$\tau = \frac{\rho c_p d}{4h}. \tag{3.5}$$

In the range of Re investigated ($Re \lesssim 1000$), the heat transfer coefficient is independent of the flow rate [51], so that this characteristic time remains unchanged when the flow rate is varied.

This simple heat transfer model was tested experimentally by measuring the temperature at the outlet of the tube for various flow rates and tube lengths, Fig. 3.2. The data superimposes remarkably on an exponential decay law, as predicted, with a characteristic time of 1.30 s for the 0.81 mm tube. This strongly indicates that the model is adequate to describe the thermal history and that the heat transfer coefficient is independent of the flow rate. From this characteristic time value, the heat transfer coefficient is about $h \simeq 640$ W/K/m^2 and is similar to the coefficient that could be estimated assuming that transfers were limited by heat conduction through the tube walls. Importantly, this value of the thermal characteristic time allowed us to approximate the exponential function by a step function for times longer than a few tens of seconds. The heating rate was slower for the 0.25 mm tube, as it was thicker. From the thermal resistance of this tube, we estimate a thermal characteristic time of 3.38 s. This tube was only used for experiments at shear rates and residence time of more than 2000 s^{-1} and 60 s, respectively.

The residence time was limited to 15 min as the quantification of the fraction of remaining native-like WPI at this time showed that 5% of native WPI were remaining. This quantification was achieved according to the loss of solubility of the denatured protein at pH 4.6 [28]. Non-native like proteins and aggregates were precipitated by pH adjustment and the solution was then centrifuged at 20.000 $\times$ g for 20 min. The concentration of remaining native-like WPI in the surnageant was determined by UV absorption at 280 nm.

3.2.3 Test tube aggregation process

Aggregation under static conditions was induced in a polypropylene "test tube" of 5 mL (Eppendorf tube). This aggregation process is referred to as test tube process later on in this article and was used as a control with shear rates limited by natural convection. In this setup, isothermal conditions were reached after 3 minutes.

3.2.4 Small-Angle X-Ray Scattering

SAXS experiments were performed at ESRF (Grenoble) on beamline ID02 which offered an energy of 12.46 keV and a wide range of wave vector q, from 3×10^{-3} to 4 nm^{-1}. Samples were analyzed under static conditions in a glass capillary of 2 mm diameter. This method serves to measure the scattering of several samples within the same capillary, without handling it, and thus to accurately subtract the contribution of the tube and the solvent from the scattering spectra. To minimize X-ray damage of the sample, the exposition time was set at 0.5 s. For each experimental condition tested, the background of the cell containing water and 4 spectra were acquired. Spectra of aggregates were obtained by averaging the 4 data sets and subtracting the background. For each condition, the sample was diluted up to a factor 100 with demineralized water to ensure that the spectrum could be assimilated to the form factor of the suspension of aggregates, i.e. the scattered intensity was linear with respect to the WPI concentration, in the whole range of wave vector. Diluting the sample with a solution of equivalent pH and ionic strength had no effect on the

spectra (data not shown).

In particular, we focused on two ranges of wave vectors. In the Guinier regime ($q \ll 1/R_g$), the scattered intensity I of a dispersion of aggregates is given by

$$I(q) = \frac{I_0}{1 + q^2 R_g^2/3} \tag{3.6}$$

where R_g is the radius of gyration of the aggregates and

$$I_0 = KC_{\text{agg}}M_w, \tag{3.7}$$

where K is a constant, C_{agg} is the concentration aggregated proteins and M_w is their mass. I_0 and R_g were obtained by a least-square fitting of I as a function of $1/q^2$. Conformational changes in the structure of the proteins were detected in the high range of wave vector (0.5-3 nm^{-1}) by plotting Iq^2 as a function q^2 (Kratky plot, Pérez et al. 94), which allowed us to follow the kinetics of denaturation.

3.2.5 Resonant Mass Measurement

The mass of individual aggregates M_w and its distribution were measured independently from SAXS analysis by resonant mass measurement (RMM, Archimedes, Malvern). A highly diluted dispersion was injected in a microfluidic channel with a micro-cantilever (Hi-Q Micro Sensor), for which the resonant frequency was calibrated. When a particle goes through the channel, the resonant frequency of the cantilever changes depending on the buoyant mass of the particle.

The buoyant mass (M_B) is proportional to the frequency shift Δf

$$M_B = \Delta f S \tag{3.8}$$

where S is the sensitivity of the resonator. The conversion of M_B into dry mass of aggregates M_w is based on the density of whey protein ρ_{WPI} (1.32 g/mL) and the density of water ρ_w [135]

$$M_w = \frac{M_B}{1 - \frac{\rho_w}{\rho_{WPI}}} \tag{3.9}$$

An archimedes device could detect particles with a mass of at least 4.5×10^{-16}g. A few thousands of aggregates were analyzed per sample, which enabled us to determine the probability density function (PDF) of aggregates mass weighted by their mass.

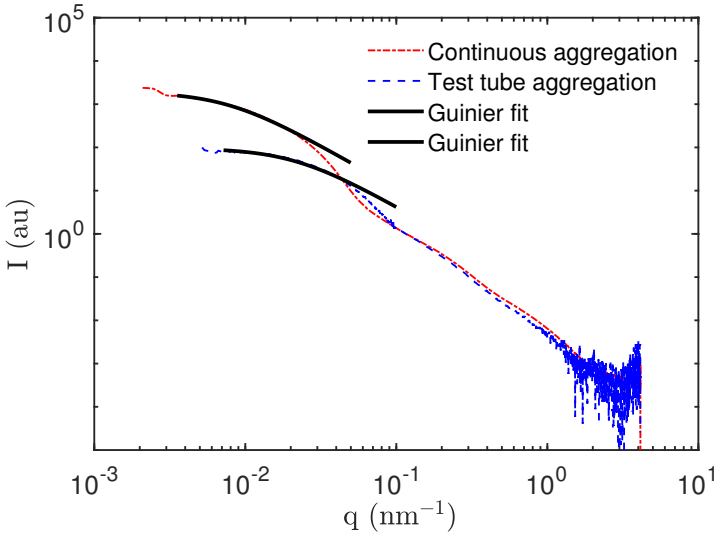

Figure 3.3: SAXS intensities $I(q)$ of the WPI aggregates obtained after 15 min of heat treatment at 92°C in a test tube (dashed line) and our millifluidic continuous process ($\dot{\gamma} = 53$ s^{-1}, $d = 0.81$ mm, $Q = 15$ mL/h, $L = 7.3$ m) (dashed-dotted line). Large differences at low q were obvious, whereas the spectra superimposed at high q. Guinier fits (solid lines) gave R_g of 74 and 225 nm for test tube and continuous processes, respectively.)

3.3 Results and Discussion

3.3.1 Comparison with aggregation in test tube

The main advantage of our millifluidic process of aggregation was to heat the solution of proteins at 92°C in few seconds and to control shear rates in laminar conditions (Figure 3.2). For a residence time of 15 min, we first compared the aggregates produced using the continuous millifluidic process ($\dot{\gamma} = 53$ s $^{-1}$) and those using a more standard process in a test tube of 5 mL. In this second case, shear rates were limited to some natural convection and isothermal conditions were reached after 3 min.

The aggregates showed large differences on length scales larger than 10 nm, whereas there was no difference at smaller length scales (Fig. 3.3). For q larger than 0.1 nm^{-1}, the scattered intensities superimposed, meaning that the small scale structures of the aggregates were similar for both conditions. Moreover, quantification of the fraction of native WPI by pH adjustment to 4.6 [34] showed that the aggregation was almost complete at the end of the thermal treatment for both processes; the residual quantity of native WPI being only 5%. This statement was supported by the strong similarities of I in the q range of 0.5-2 nm^{-1}.

However, large differences were evidenced at lower q in the Guinier regime with striking differences in terms of radius of gyration R_g and scattered intensities I_0 (Eq. 3.6). R_g in test tube was 74 nm, i.e. three times lower than in the case of the millifluidic process (225 nm).

I_0 of aggregates obtained by millifluidic continuous process was 21 times bigger than the value of I_0 of aggregates obtained by test tube process. As C_{nat}/C_0 was about 0.05 at 15 min, we concluded that aggregation is almost complete for both processes after 15 min. Thus, the variation on the value of I_0 between the two conditions reflected directly the variations of mass of the aggregates ($I_0 \sim M_w$, Eq. 3.7). We inferred their relative density, $\rho^b/\rho^c \sim I_0^b/I_0^c \left(R_g^c/R_g^b\right)^3$, where ρ is the density in WPI of the aggregates and b and c refer to test tube and continuous conditions, respectively. We did not find any significant density differences between the two processes, $\rho^b/\rho^c \sim 1.3$. At first sight, this result does not fit with the findings of Spiegel [121] of an increasingly compact aggregate structure with temperature. However, the thermal history was characterized by a slow heating across the range of temperature in our test tube, whereas isothermal conditions were achieved in the tubular process used by Spiegel [121].

Two main differences between the two processes could be put forward to explain these contrasts: the thermal history and the fact that the continuous process involved a flow. The temperature strongly affects the various stages of WPI aggregation, their kinetics, their size [29, 95, 121] but also the protein conformations [94, 127]. However, we did not observe significant differences in the high q range of the spectra between the two conditions, where protein conformation changes could be observed (see next section). In the continuous process, aggregation kinetics took place in a Poiseuille flow, which exhibited a gradient of velocity. Few studies showed that the shear rate could influence the size of large aggregates [29, 115, 136]. The shear rate was also non-zero in the test tube due to natural convection, but should be smaller than the mean shear rate investigated in the small scale continuous process (53 s^{-1}). At this stage, it seemed difficult to further interpret the above result without the additional experiments that are detailed hereafter.

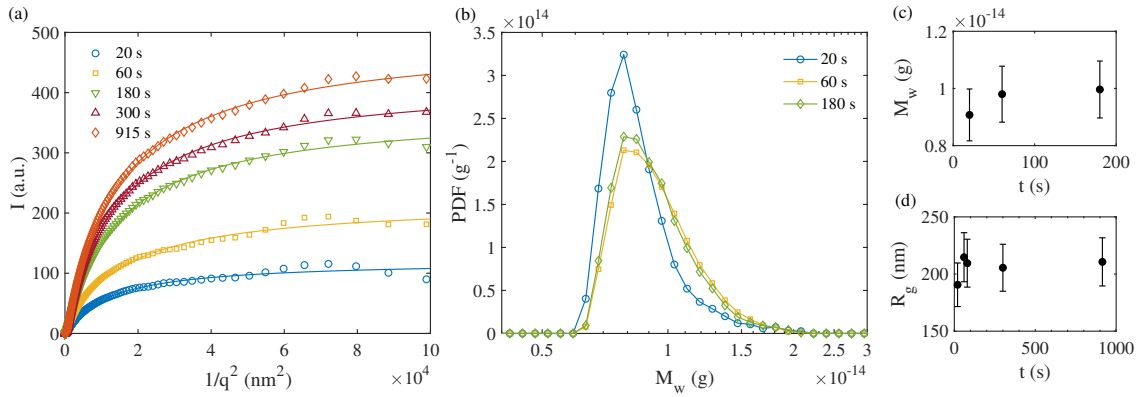

Figure 3.4: Kinetics of WPI aggregation. *a:* Guinier plot of SAXS intensity of aggregated WPI solutions for various residence times t at $\dot{\gamma} = 53$ s^{-1} Solid lines are the fit of Guinier equation, Eq. 3.6. d = 0.81 mm, Q = 15 mL/h, L = 16.2 - 740 cm. *b:* Probability density function (PDF) of the mass of aggregates M_w for various t at $\dot{\gamma} = 32$ s^{-1} as determined by RMM. d = 0.81 mm, Q = 9 mL/h, L = 10 - 87 cm. *c:* Mean value of M_w as a function of t, as determined by RMM. *d:* Radii of gyration R_g, which were obtained by the Guinier fit, as a function of t. Error bars represent ±10% of the mean value.

3.3.2 Kinetics of aggregation in isothermal conditions

The reaction and aggregate formation kinetics was studied using the millifluidic continuous process. We studied these kinetics along a range of residence time t (20 s - 15 min), for which the thermal history was approximated by a step function from 22 to 92°C (Figure 3.2).

R_g and M_w evolution of WPI aggregates with t for fixed values of $\dot{\gamma}$ (32 and 53 s^{-1}) were determined by SAXS and RMM, Figure 3.4. The results showed unambiguously that R_g and M_w remained almost constant from 20 s to 15 min of aggregation, with $R_g \simeq 205$ nm and $M_w \simeq 10^{-14}$ g. The slight increase of M_w remained in the order of the measurement uncertainty. We were also aware that the continuous process tended to average the tendencies over time due to diffusion and hydrodynamic dispersion in the longitudinal direction of the flow (see Section 3.2.2). The probability density functions (PDF) of M_w revealed that the suspension of aggregates had a polydispersity with a standard deviation of 30% of the mean value. Our results were in line with those of [29] who studied WPI aggregation under similar physico-chemical parameters. The main differences were the thermal history and flow conditions, which were more complex (laminar and turbulent conditions) than those of this work. They also revealed the existence of a second population of WPI aggregates of smaller size by field-flow fraction. However, RMM could not detect masses smaller than 4.5×10^{-16} g. The aggregation number, which depicts the number of protein particles making up an aggregate, was about of $N_{\text{agg}} \simeq 3.3 \times 10^5$. The fractal dimension being 2 at pH 7.0 [29, 43, 79], we estimated the size of the aggregates, as $R_g = b\sqrt{N_{\text{agg}}}/6$, with b the size of the β-lactoglobulin [81], the main component of WPI. We found 220 nm, in very good agreement with the value estimated from the Guinier regime.

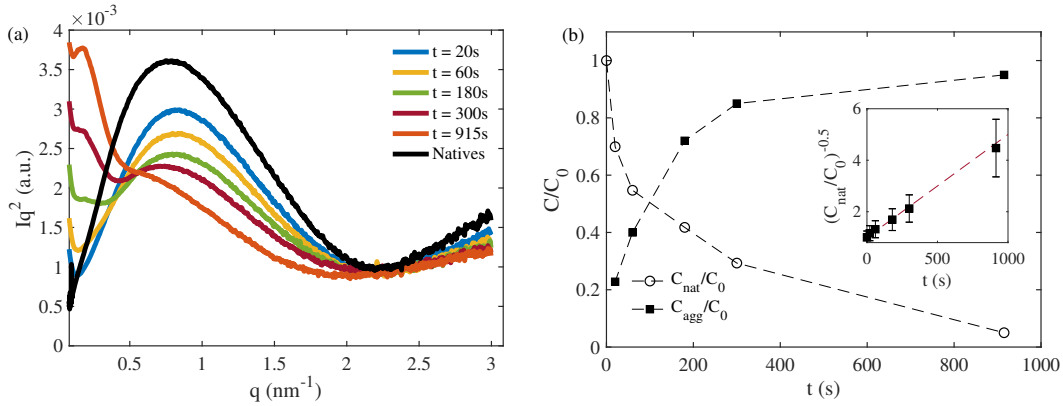

Figure 3.5: *a:* Kratky plots showing the change of WP conformation with the residence time t. . *b :* the fraction of native WP, C_{nat}/C_0 was determined from high q-range of spectra (∘, Eq. 3.10, 3.11) and was calculated from a linear combination of the spectra of natives and aggregated WPI in the q-range 1-2 nm^{-1} (dashed lines), see text for details. The fraction of aggregated WP, C_{agg}/C_0, was determined independently from the low q-range of spectra (■, Eq. 3.12). Dashed lines are guide for the eyes. In insert, kinetic plot $(C_{\text{nat}}/C_0)^{1-n}$ versus t with reaction order n= 1.5. $\dot{\gamma}$ = 53 s^{-1}, d = 0.81 mm, Q = 15 mL/h, L = 10 - 87 cm

In contrast with the size, the scattered intensity at low q, I_0, increased progressively with t. Since the aggregate mass was roughly constant, I_0 was directly proportional to the concentration of aggregates C_{agg} (Eq. 3.7). Therefore, the aggregate concentration increased significantly from 20 to 915 s, by a factor of about 4.

This first set of results showed that the aggregate growth happened at short time scales (less than 20 s) and their size was limited, whereas WPI were continuously aggregated on time scales of few tens of minutes. These observations were consistent with previous studies [29, 109, 148], except that at lower temperature the aggregates grew at time scales of a few minutes.

The kinetics of proteins unfolding was studied by focusing on the high q range of SAXS spectra, which is sensitive to the protein conformation. The Kratky plots displayed in Fig. 3.5 exhibited a significant change as a function of t. For the native proteins ($t = 0$), a bell-shaped curve was seen, whose the peak position corresponded to the length scale of β-lactoglobulin. The peak intensity decreased when the residence time increased. For the longest residence time (915 s), this peak was very weak. This bell-shape curve is a signature of a globular protein [15, 105], and the decrease of its intensity reflects the unfolding of the proteins upon heating [94]. Taking advantage of this feature and the fact that the form factor is a linear combination of the form factors of the different states of the protein in solution [94], i.e. native, partially unfolded and irreversibly aggregated, we estimated the progress of the unfolding process.

In the range 1-2 nm^{-1}, and as evidenced in Fig. 3.5, all the spectra were described by a linear combination of the spectrum of the native protein solutions (I_{nat}, at $t = 0$)

and of the final spectrum (I_f, $t = 915$ s), i.e the presence of partially unfolded proteins was neglected,

$$I(t,q) = \alpha(t) I_{\rm nat}(q) + [1 - \alpha(t)]\, I_{agg}(q) \tag{3.10}$$

with $\alpha(t) = C_{nat}(t)/C_0$. The acid precipitation test carried out on the final solution (at $t = 915$ s) revealed that it contained about 5% of native proteins. Thus, $I_f = 0.95 I_{\rm agg} + 0.05 I_{\rm nat}$, where $I_{\rm agg}$ is the intensity of a fully aggregated solution. The remaining fraction of native proteins was inferred from the value of α for a given aggregation time, as

$$\frac{C_{\rm nat}(t)}{C_0} = 0.95\alpha(t) + 0.05. \tag{3.11}$$

The fraction of native proteins decreased in the first 60 s, a time at which half of the proteins were unfolded (Fig. 3.5). Note that the estimation of $C_{\rm nat}$ by the test of the loss of solubility of the denatured protein at pH 4.6 was coherent with the values obtained by SAXS.

This kinetics of unfolding was compared with that of aggregated WPI, $C_{\rm agg}(t)$. Since the aggregate mass was approximately constant, the fraction of aggregated proteins was directly inferred from the time evolution of the low-q SAXS intensity I_0:

$$\frac{C_{\rm agg}(t)}{C_0} = 0.95 \frac{I_0(t)}{I_0(t = 915s)}. \tag{3.12}$$

Note that this quantification of $C_{\rm agg}$ was independent of that of $C_{\rm nat}$, which was inferred from high-q SAXS intensity plot.

The symmetry between $C_{\rm agg}/C_0$ and $C_{\rm nat}/C_0$ is striking (Fig. 3.5). Moreover $(C_{\rm agg}(t)+C_{\rm nat}(t))/C_0$ varied by $\pm 15\%$ around 1 during the entire aggregation process. This clearly shows that the rate of protein unfolding was that of protein aggregation. This result highlights the self-consistency of our approach and confirms that WPI aggregation occurs as soon as a nucleus is present. it is worth mentioning that the above analysis in the high-q range assumes only two states for the protein conformation, which was an oversimplified picture. However, the fact that $(C_{\rm agg}(t) + C_{\rm nat}(t)) \simeq C_0$ justifies *a posteriori* this assumption.

The order of the reaction n is defined as $dC_{\rm agg}/dt = kC_{\rm nat}^n$, where k is the reaction rate constant, which is supposed to be a function of temperature and solvent composition. Reaction orders n were reported to vary between 1 and 2 [28, 31, 39, 97, 109, 136, 148]. From kinetic models of β-lactoglobulin that recognized that the rate of nucleation (initiation) is much smaller than the rate of propagation (aggregation), we expected a n of 1.5 [109, 127]. $n = 1.5$ was also predicted theoretically for rapid aggregation theory of colloidal solutions [118]. Our results were consistent with an order of 1.5 (subpanel in Fig. 3.5-b) and confirm that nucleation is the limiting step.

A simplified reaction scheme for the aggregation may consist in two main steps, the first one is a nucleation step, where one or a few (n_0) native proteins N undergo conformational change and irreversible association to form a precursor P for

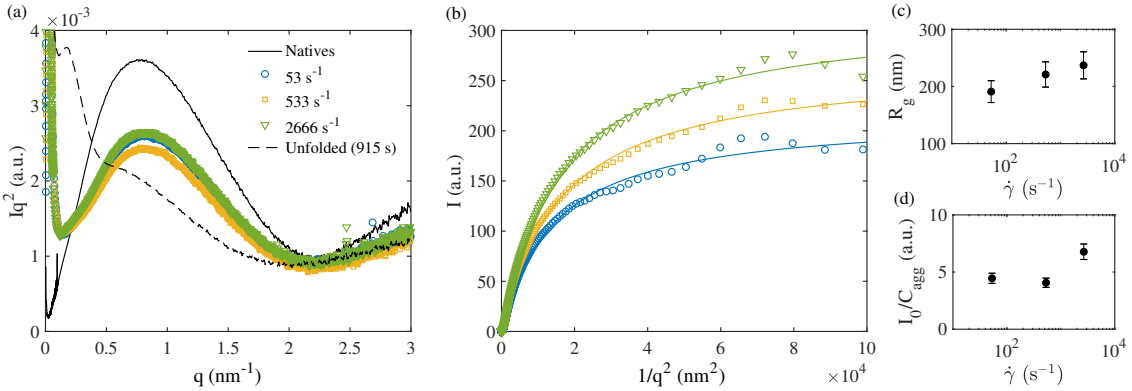

Figure 3.6: Effect of shear rate on denaturation and aggregation. *a:* Kratky plot showing the invariance of WP conformation for the different shear rates investigated for $t = 60$ s . Solid and dashed black lines correspond to the native and fully aggregated solutions (i.e. $t = 915$ s), respectively. *b:* Guinier plot of SAXS intensity for various shear rates at $t = 60$s. Solid lines are the fits using the Guinier equation (Eq. 3.6). *c:* Radii of gyration R_g as a function of $\dot{\gamma}$. *d:* I_0/C_{agg} as a function of $\dot{\gamma}$. $C_{\text{agg}} = 1 - C_{\text{nat}}$ was determined from the Kratky plot and is almost constant for the the different shear rates. I_0/C_{agg} was proportional to M_w (Eq. 3.6). d = 0.81 mm and 0.25 mm for $\dot{\gamma} = 2.5 \times 10^3 \text{s}^{-1}$, Q = 15 - 150 mL/h, L = 48.6 - 750 cm.

subsequent aggregation in aggregates A_i made of i proteins

$$\begin{aligned} n_0 N &\rightarrow P \\ P + N &\rightarrow A_{n_0+1} \\ A_{n_0+i} + N &\rightarrow A_{n_0+i+1} \end{aligned}$$

This scheme is that of a standard nucleation and growth process. It does not detail the initial conformational changes leading to the first irreversible precursor P, but since these are reversible with a very short characteristic time [107], they have limited impact on the aggregation scenario except concerning the dependency with initial concentration C_0, which is not studied here. It also ignores possible combinations between aggregates. To fully model the above results, this reaction scheme should involve a kind of termination step in order to limit the growth of the aggregates to a given size [107, 109]. The possible mechanisms are discussed hereafter.

The above detailed experimental results might be summarized as follows: *(i)* Denaturation and aggregation occurred consequently, since intermediate states of WPI (i.e. unfolded but not aggregated) were negligible at all times, *(ii)* Aggregates were formed within a few seconds, much faster than the global reaction rate, and their concentration kept growing over time with constant size and mass. The second one implied two features: on the one hand aggregation is not the limiting step and on the other hand there exists an additional mechanism which limits the growth of the aggregates when they have reached a given size. Other scenarios are not compatible

with these two key observations. In particular, if aggregation was the limiting step, then the aggregate size would have increased significantly during the process.

We could only speculate on the scenario which limits the growth of the aggregates to a given size (for the studied experimental conditions, about 200 nm). Based on analogy with radical polymerisation chemistry, [109] suggested that the polymerization process of β-lactoglobulin stopped when one reactive intermediate A_{n_0+i} reacted with another one forming an aggregate without a reactive sulhydryl group. Under this assumption, they predicted that $M_w \sim C_0^{0.5}$. Their reaction scheme was consistent with their kinetics of aggregation at low temperature (65°C). However, [148] moderated this concept, as their experiments at 80°C insinuated that small molecular weight intermediates were cross-linked by disulfide bonds and formed larger aggregates via noncovalent bonding (e.g. by hydrophobic interactions). Competition between short-range depletion attraction and long-ranged electrostatic repulsion also leads to equilibrium clusters of finite-size whose number of aggregation N_{agg} is proportional to C_0 [21, 22, 123]. However, some of our preliminary results would invalidate the above-mentioned mechanisms as we found that R_g was constant for C_0 ranging from 0.4 to 4% w/w at 92°C and residence time t of 60 s, in agreement with [79, 97](pH 7.0, no added salt, 85°C and $C_0 \leq 7$ g/L). Alternatively, our results could be explained by the mechanism introduced by [97] in which a self-stabilization effect could appear due to spontaneous increase of the pH during aggregate formation that should lead to an increase of their surface charge density and inhibits secondary aggregation. Similarly to the association of charged amphiphilic polymers [144], counterions should be partly repelled from the aggregates and may lead to this electrostatic repulsion. At this stage, we have no experimental evidence that could validate or not one of these mechanisms. Additional studies varying the ionic force and the concentration of WPI would be interesting to test these various hypotheses.

3.3.3 Effect of shear rate

The flow rate Q was one of the important control parameters of the millifluidic continuous process that allowed us to increase the production rate, but also the mean shear rate $\dot{\gamma}$ (Eq. 3.2) in laminar conditions. The general picture depicted by previous studies is that shear rate could be a control parameter of the aggregate size. For low and moderate shear rate, the size should increase as the rate of collision between monomers and oligomers increases. At higher shear rates, the size should decrease as shear forces could break down the aggregates. An optimum could exist [115, 136]. However, this picture is not clearly established for thermal denaturation of proteins due to the difficulty of uncoupling thermal history from flow conditions [29, 39]. We studied a range of shear rates $\dot{\gamma}$ which extended from 50 s^{-1} to 2.66×10^3 s^{-1} (Fig. 3.6). The comparison was made for an intermediate residence time t of 60 s for which one half of native WPI were aggregated and so Kratky plots were sufficiently distinct from native and fully aggregated proteins. This particular choice had no major consequences since we reported that the structural properties of the aggregates (mass and size) did not significantly depend on the residence time.

The Kratky plots for the three shear rates investigated superimpose in the high-q

range (Fig. 3.6-a). This feature showed unambiguously that the aggregation kinetics was not changed when $\dot{\gamma}$ was increased. For very high shear rates, the flow could influence the frequency of the collisions between reactants and thus increase the reaction rate. The relevant Péclet number for this effect is $\mathrm{Pe} = \dot{\gamma} l^2/D$, where l is a characteristic distance between the considered reactants, which was of the order of 10 nm for the proteins, but significantly higher for the aggregates. For the highest shear rate tested, this Péclet number remained lower than unity ($\mathrm{Pe} \simeq 0.2$), meaning that diffusion remained the dominant mechanism. It is thus not surprising that the shear rate did not influence the aggregation rate, provided that the nucleation stage is the limiting one.

In the Guinier regime, the data plots in Fig. 3.6-b exhibit a small trend. Both I_0 and R_g slightly increased when the shear rate was increased. R_g increased by about 10% for variations of $\dot{\gamma}$ of almost two orders of magnitude. From the values of I_0 obtained by the best Guinier fits and the value of $C_{\mathrm{agg}} = 1 - C_{\mathrm{nat}}$ inferred by a linear combination in the Kratky plots (see previous section and Fig. 3.5), we calculated the aggregate mass $M_w \sim I_0/C_{\mathrm{agg}}$ (Eq. 3.7). M_w increased slightly with $\dot{\gamma}$, similarly to the radius of gyration. We were aware that these variations are of the order of magnitude of the measurement uncertainties, whereas $\dot{\gamma}$ varied by almost two orders of magnitude. We concluded that the shear rate had no significant influence on the aggregation or on the denaturation in isothermal conditions.

We returned our attention to the marked size differences between aggregates prepared using the millifluidc continuous process and the ones prepared in test tube (Fig. 3.3). We inferred that the shear rate was not responsible for this large increase of the aggregate size when switching from test tube to continuous process for the physico-chemical conditions investigated. The difference in heating rate was more likely to be responsible for the difference between test tube and continuous process. As in most processes, the scales are of a few millimeters, it is impossible to separate thermal from flow conditions. In light of the above results, our opinion was that some effects attributed to the influence of shear rate in previous studies [115, 136] could be in fact attributed to large differences of thermal history. Additional studies varying the thermal history could be of interest to confirm that the latter could be used to tune the size of the aggregates.

3.4 Conclusions

In this paper, we studied the denaturation and aggregation of whey protein isolates under flow and at high temperature (92°C) for a single physicochemical condition leading to sub-micrometric aggregates (neutral pH, 10 mM NaCl,WPI 4 % w/w) with a well-controlled thermal history. We showed unambiguously that the size and mass of aggregates reached a steady state value within a few seconds, whereas the time scale associated with the kinetics of aggregation was of a few minutes. Moreover, we calculated from the Kratky plots the kinetics of consumption of native proteins, which was symmetrical to the kinetics of aggregated proteins. It means that partially unfolded proteins were virtually absent and WPI aggregated as soon as they are un-

folded. The order of the reaction was consistent with 1.5, typical for rapid aggregation of proteins [109, 127]. All these results lead us to conclude that the aggregation at 92°C is limited by the nucleation and there is a mechanism that limits the size of the aggregates. The underlying mechanism is an open issue [97, 109, 123, 148]. Different scenarios could be tested by varying protein concentration and / or ionic strength.

Moreover, we observed that the size of the aggregate and the denaturation is almost invariant with the shear rate (for variations covering almost two orders of magnitude) in isothermal conditions. We concluded that shear rate does not influence aggregation for the conditions tested and thermal history can be reasonably considered as responsible for the huge difference in terms of aggregate size between our millifluidic process and test tube conditions. This latter finding highlights the interest of studying growth of aggregates and unfolding with various thermal kinetics. The approach that we used in this work makes it possible to simultaneously characterize denaturation, nucleation and aggregation. We think it could be of great interest to extend it to other temperatures, especially higher ones which have been described as aggregation limited conditions [28].

3.5 Annexe: Study of the temperature of aggregation

The effect of the temperature of aggregation on the structure of WPI aggregates formed at 4% w/w 10mM pH 7.0 during 300 s under an average shear of 53 s^{-1} was studied by SAXS on a temperature range of 75-95°C. Concerning the lowest temperatures of the studied range (75°C - 86°C) (Figure 3.7-a), the range of wave vectors studied in SAXS did not allowed to reach the Guinier regime. The size of these aggregates could not have been determined, contrary to the highest temperature of the range, 92°C, for which a radius of gyration R_g = 230 nm of the aggregates was defined. Decreasing the temperature of aggregation, from 92°C to 75°C, increased the size of the aggregates for the same aggregation time. The Kratky plot (Figure 3.7) shows a change of the conformational state of the proteins which depended on the temperature of aggregation. Without access to the fully aggregated spectra at each temperature, it was not possible to analyse the denaturation kinetics, although the literature concludes that the denaturation rate increases with increasing temperature. WPI aggregates formed at temperatures below 92°C show a less unfolded conformation and a larger radius of gyration than WPI aggregates formed at 92°C at the same aggregation time. The study of kinetics at these different temperatures of aggregation was not carried out, so it was difficult to analyse these results in more details. However these results were consistent with other studies which concluded that larger aggregates were formed at lower temperature due to increasing hydrophobic interactions rather than chemical interactions ([32]).

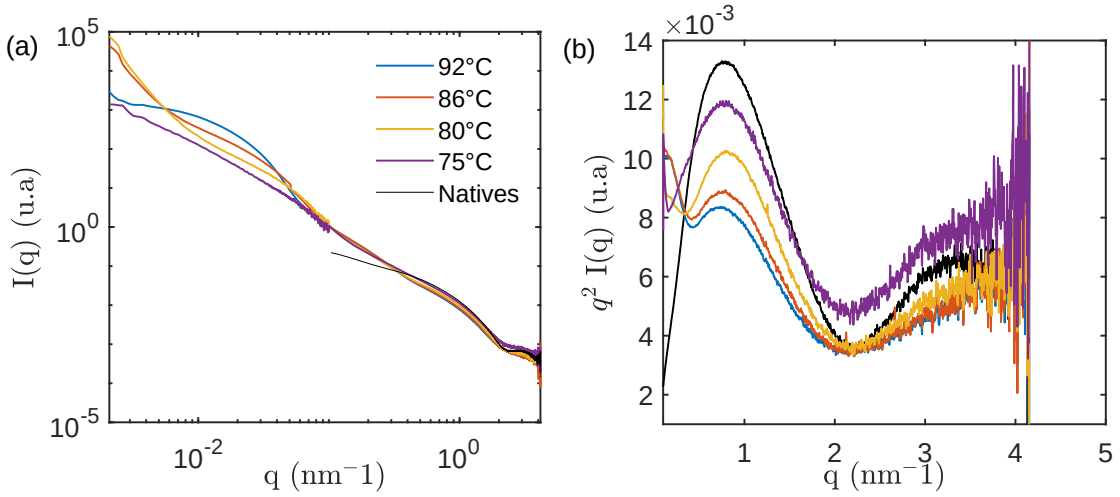

Figure 3.7: a: SAXS intensities I(q) of the WPI aggregates formed at 4% w/w 10 mM pH 7.0 after heat treatment at different temperature of aggregation and t = 300 s. b: Kratky plot showing the evolution of WP conformation for the different temperature of aggregation investigated for t = 300 s, $\dot{\gamma}$ = 53 s^{-1}, d = 0.81 mm, L = 246 cm, Q = 15 mL/h.

- Thanks to the millifluidic process, we studied both the kinetics of aggregation after few seconds and its dependence with the mean shear rate in isothermal conditions.
- Size and mass of aggregates reached a steady-state value in a few seconds at 92°.
- The kinetics of aggregation and denaturation had a characteristic time of few minutes.
- The shear rate had no significant effect on the size of the aggregates, or on the aggregation kinetics.
- WPI aggregation at 92°C is limited by a step of nucleation.
- The thermal conditions have a major influence on the size of the aggregates.

Chapter 4

Quantitative structural analysis of heat-induced WPI aggregates by covalent labelling and fluorescent microscopy

Kinetics of heat-induced aggregation of WPI have been studied using Small-Angle X-ray Scattering at low WPI and salt concentration and submicrometric aggregates where formed under continuous aggregation process. In this section we discuss the characterization of large aggregates (1-100 μm) where no dedicated techniques enables their structural characterization. A covalent labelling reaction between β-lactoglobulin with RITC is performed with the aim to relate the fluorescence intensity of RITC to the protein concentration and thus to the mass of protein. This relation will therefore allow the quantification of the mass of proteins contained in aggregates. This technique, based on microscopic image analysis, will therefore enable the structural characterization of micron-sized aggregates, including their mass, density, size and shape anisotropy.

Contents

4.1 Introduction

The behavior of whey proteins upon heating as a function of the environmental conditions (protein concentration, salts concentration, pH) were widely studied and resulted in a comprehensive approach of heat-denaturation and aggregation and gelation mechanism. The structure-function relationship at different scales has been the center of several studies. The characterization of the structure is necessary for a full understanding of the aggregation and gelation process with resulting structure and mechanical properties.

The structure of an aggregate can be described in terms of its size (hydrodynamic radius, radius of gyration), density, mass (g) or weight average molar mass (g/mol) and can be assessed by different techniques such as microscopy with Transmission Electron Microscopy or cryo-TEM [11, 37, 44, 129, 134] or optical microscopy, light scattering with dynamic, static, SAXS, SANS [69, 133] and size exclusion chromatography. These techniques are useful tools for characterising submicrometric aggregates but are not fully effective for characterising aggregates of few tens of micrometres.

Thus, there is no dedicated method to measure their mass and density in proteins. Quantitative analysis of gel structure have been done on confocal laser scanning microscopy images, in terms of pair correlation function of the protein concentration fluctuations [1]. Cross-correlation dynamic light scattering have also been used to overcome the effect of multiple scattering on the scattered light intensity for characterizing the structure of turbid Heat-Set Globular Protein Gels [88].

The technique developed and presented below will allow us to overcome the size limitation of the cited techniques and quantify the relation between the aggregates proteins mass to their gyration radius. A covalent labelling reaction between β-lactoglobulin with RITC is performed with the aim to relate the fluorescence intensity of RITC to the protein concentration and thus to the mass of protein. This relation will therefore allow the quantification of the mass of proteins contained in aggregates. This technique, based on microscopic image analysis, will therefore enable the structural characterization of micron-sized aggregates, including their mass, density, size and shape anisotropy. From the literature, this kind of method has not been developed, expect some methodologies to covalently labeled proteins with a fluorescent probe [65, 72, 111].

4.2 Material and methods

4.2.1 Whey Protein Isolate

Whey protein isolate Prolacta 95 (batch 30916B) was purchased from Lactalis Ingredients (Bourgbarré, France). The composition of the WPI (Nx6.38) was (in g/100g powder wet basis): protein 88.5 (of which β-lactoglobulin 65%, α-lactalbumin 20%, soluble caseins 10% and almost 5 % of bovine serum albumin and immunoglobulin, ash 1.9, moisture 5.6, carbohydrates 0.14, fat 0.5). The mineral composition was (g/100g powder wet basis): Ca 0.35, Mg 0.06, Na 0.15, K 0.35, P 0.21, Cl 0.01. WPI stock solution of 15% w/w was prepared by weighting the required amount of WPI powder and added to demineralized water. Sodium Azide (0.02% w/w, Sigma-Aldrich CAS 26628-22-8) was added to the solution to prevent bacterial growth. The solution was gently stirred for 12 hours for complete dissolution of WPI powder at 4°C. WPI concentration was measured by UV absorption at 280 nm using extinction coefficient of 1.0241 $\mathrm{Lg^{-1}cm^{-1}}$.

4.2.2 Rhodamine B isothiocyanate

Rhodamine B isothiocyanate (RITC, CAS number 36877-69-7) as well as the solvent Dimethyl sulfoxide (DMSO, CAS number 67-68-5) was purchased from Sigma-Aldrich. A stock solution of RITC was prepared in percent by weight to reach the concentration of 0.118 % w/w in DMSO and wrapped in aluminium paper. The density of DMSO was 1100 g/L. Dilutions were prepared from the RITC stock solution (1300 ppm) with addition of demineralized water and measured by UV absorption at 555 nm and 280 nm with a quartz cuvette of 10 mm. The blank was done on deionised water. We found an extinction coefficient of 0.0912 $\mathrm{Lg^{-1}cm^{-1}}$ for $\lambda = 555$ nm.

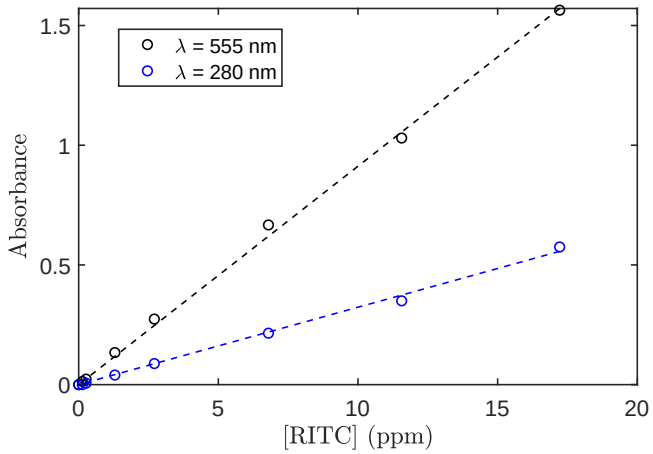

Figure 4.1: Absorption curve of RITC molecules dissolved in DMSO

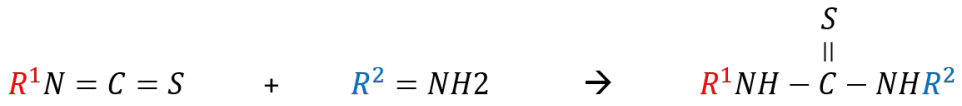

Figure 4.2: Chemical acylation reaction between an isothiocyanate group and a primary amino group

4.2.3 Covalent labelling

Principle

A fluorophore is a fluorescent molecule that can absorb energy from electromagnetic radiation in its own wavelength range (excitation light) and return some of it as emission light. The emission wavelength range is higher than the excitation range as the molecule returns to the ground state from the lowest vibration level of the excited state. The energy of an incident photon, characterised by an absorption (excitation) wavelength $\lambda_{absorption}$, moves an electron of the fluorophore from a ground state to an excited state. This electron progressively loses energy by passing through various excited states before returning to its basal state by releasing the remaining energy in the form of a photon at an emission (fluorescence) wavelength $\lambda_{emission} > \lambda_{absorption}$. For each fluorophore we can thus establish a spectrum of wavelengths capable of exciting it as well as a spectrum of fluorescence wavelengths, and define a wavelength of maximum absorption and emission. A fluorophore is also characterised by its molar extinction coefficient, its quantum yield and its fluorescence lifetime. Various fluorescent labels are used for protein labelling (ANS, FITC, Nile red, Nile blue, Rhodamine) for contemplative microscopy. In our study we chose to use rhodamine isothiocyanate (RITC) with an isothiocyanate group involved in the conjugation reaction. RITC molecules are excited between 532 and 555 nm and emit between 570 and 613 nm (Figure). The isothiocianate group, of formula —N═C═S, characterised by the strongly electrophilic nature of its central carbon ([142]), specifically reacts by covalent bonding with primary amine groups and with thiols ([104]) to produce a fluorescent conjugate (Figure 4.2). β-lactoglobulin contains 16 potentially reactive amine groups, including the N-terminal group and the ϵ amine group of the 15 Lysine amino acid residues, as well as a free thiol functions. The free thiol Cys121 and the ϵ amine group of the lysines have a pKa of 8.3 and 10.8 respectively. At basic pH and above the pKa of the species, thiol and amine are deprotonated and can react with the isothyocianate group.

A covalent labelling reaction between β-lactoglobulin with RITC is performed with the aim to relate the fluorescence intensity of RITC to the protein concentration and thus to the mass of protein. This relation will therefore allow the quantification of the mass of proteins contained in aggregates. This technique, based on microscopic image analysis, will therefore enable the structural characterization of micron-sized aggregates.

Labelling procedure

To analyse quantitatively aggregates by fluorescence, an optimal molar ratio between

RITC molecules and proteins must be determined in order to obtain a good fluorescence signal without interfering in the functionality of the proteins. The labelling procedure was carried out according to the procedure used by [65, 71, 111]. With an extent of labelling of 0.02 mol of RITC per mol of β-lactoglobulin (1 RITC per 50 β-lactoglobulin), 2% of the proteins and about 0.13% of the lysines should be labelled, considering 15 lysines per molecule of β-lactoglobulin. A 10% w/w of labelled WPI concentration was prepared from the stock solution with a final concentration of RITC dye of 1.14×10^{-4} mol/L. A 2.43×10^{-3} mol/L RITC stock solution was prepared by dissolving the powder in DMSO and wrapped in aluminium paper. The pH of the WPI-RITC solution was adjusted to 9.5 for the amine groups to be deprotonated with a 2M NaOH solution. After 10h of incubation at room temperature under gentle stirring and wrapped in aluminium paper, the reaction was stopped by addition of equal molar concentration of ethanolamine, 1.14×10^{-4} mol/L, (purchased from Sigma-Aldrich CAS number 141-43-5) to bound the remaining free RITC molecules. The labelled WPI-RITC solution was then dialyzed to remove the unbound fluorescent dyes against demineralized water with 200 pm sodium azide. Before dialysis, concentrations were measured by UV absorption (Figure 4.1 and 2.1): 10.3% w/w of native WPI and 54.3 ppm of RITC. Dialysis tubing cellulose membrane (Spectra/Por 1 Dialysis Tubing, 6-8 kD MWCO) were first boiled twice during 15 min to remove glycerines, sulphur compounds and heavy metals that protect the membrane. Dialysis membranes were filled with the labelled protein solution and immersed into demineralized water with 200 pm sodium azide. The ensemble was agitated with a magnetic stirrer and kept refrigerated to prevent the formation of a concentration gradient around the dialysis tubing. The counter-dialysis fluid was renewed frequently to accelerate the disappearance of diffusible substances in the dialysis tubing and to maintain the concentration gradient between the two media. It was recommended to immerse the dialysis tubing in a volume hundred times bigger than the total volume to dialyse. The ensemble was kept at 4°C and to compensate the counter-dialysis volume the counter-dialysis solution was renewed three times a day during 5 days. During the first moments of the dialysis, unbound dyes were first diffusing to homogenise the chemical potential of the two media as proteins were prevented from diffusing due to the membrane cut-off value. However, the difference in the volume of the labelled solution before and after dialysis indicated a dilution factor of 1.8 whereas the difference in the measured WPI concentration indicated a dilution factor of 4.25 (after dialysis, concentrations were measured by UV absorption (Figure 4.1 and 2.1): 2.4 % w/w of native WPI and 11 ppm of RITC, with a molar ratio of 0.015 (we consider an average molar mass of 1.75×10^4 g/mol for WPI and 536 g/mol for RITC)). This variation suggests that osmotic pressure difference leads to a progressive distortion of the pores and a certain degree of protein loss. The dialyzed labelled solution was then concentrated using a tangential filtration cell (Merck Millipore Amicon™ Stirred Cells, Biomax 10kDa Ultrafiltration Discs PES 76 mm) and the final concentration of the labelled stock solution reached was 8.4% w/w WPI and 38 ppm RITC with a final molar ratio of 0.0147.

4.2.4 Thermal aggregation of labelled WPI

Labelled WPI solutions were prepared from the dialyzed and concentrated stock solution of labelled WPI to reach a final WPI concentration of 6% and 3%. The NaCl concentration respectively was adjusted to 100 mM and 120 mM from a NaCl stock solution of 0.8 M. A labelled WPI solution was also prepared at 3% w/w, 40 mM NaCl and 20 mM $CaCl_2$. pH was adjusted to 7.0 for all the solutions. Pyrex glass tubes of 10 mL were filled completely with the solutions and heated at 92°C in a water-bath between 3 min and 45 min. Samples were then cooled in ice-bath and hand-sheared to break the protein gel. Through all the steps, samples were protected from light.

4.2.5 Quantitative image analysis method

Principle

A fluorescence image analysis methodology was developed to analyse the structure (size, protein density) of micron-sized aggregates (from 0.2 to 50 μm). The image analysis technique relies on the existence of a sufficient intensity contrast between the labelled aggregates and the background, allowing the definition of their contour and size and the quantification of their density. The images were acquired with an Olympus IX72 microscope and a Hamamatsu ORCAFLASH high sensitivity camera (12 bits). The light source was a white light LED. In order to specifically excite the RITC and to recover only the wavelengths that the excited conjugate will have emitted, we used a fluorescence filter consisting of an excitation and emission filter and a dichroic mirror. In order to keep the sample thickness constant, a gene frame of 250 μm thickness was placed on a glass slide and covered with a transparent coverslip. In order to use this experimental technique, several intermediate steps need to be validated and are presented below.

Characteristic time of photobleaching

Photobleaching is the degradation of fluorescence intensity over time due to structural instability of the fluorophore during its excited lifetime. This mechanism is deleterious to the quantification of fluorescence intensity, which was used to quantify the mass of proteins within protein aggregates. In our study, the sample was scanned along the x- and y-axis and the images were recorded continuously. A shutter system allows the light source to be switched on for the duration of the image acquisition, thus avoiding photobleaching of the edges of each scanned image. The decrease in RITC fluorescence intensity over time was compared to the time used for image acquisition. The fluorescence intensity normalised by the maximum intensity was plotted as a function of time (Figure 4.3). The measurement was performed with a lamp power of 100%. During 1 s of exposure, a decrease in fluorescence intensity of 4% was noted. Since the exposure times used were less than one second, photobleaching can be neglected.

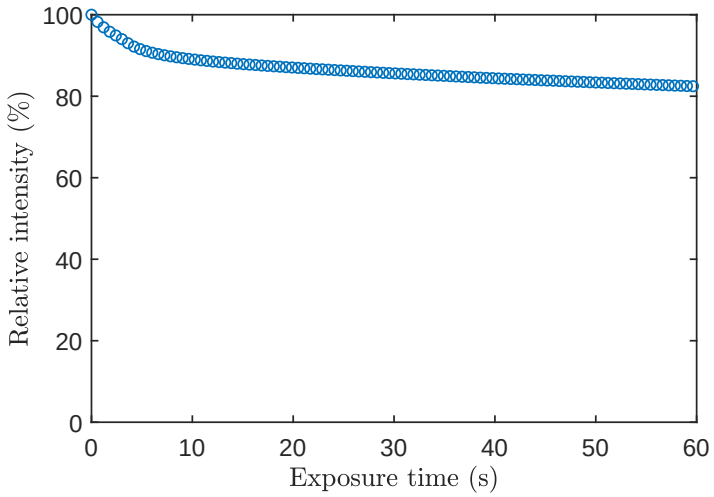

Figure 4.3: Photobleaching of a solution of labelled native WPI during 60 s of exposure

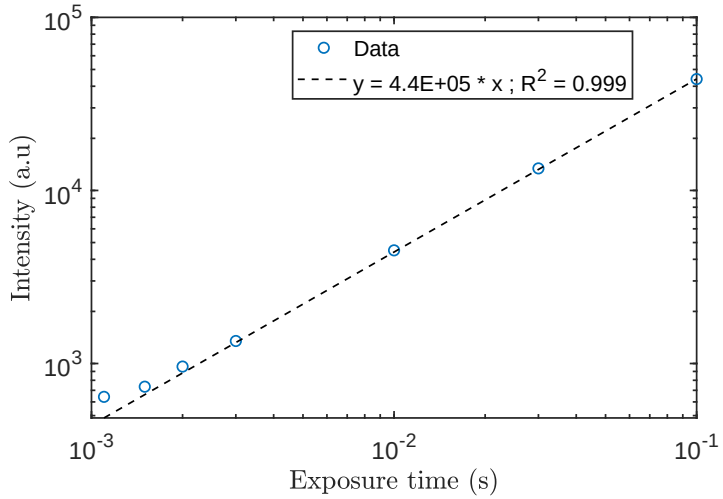

Figure 4.4: Linearity of fluorescence intensity of a labelled native WPI solution with exposure time

Linearity between fluorescence intensity and exposure time

Different exposure times were used during image acquisition, depending on the concentration of fluorescent label or labelled WPI used, in order to have a good signal to noise ratio and to avoid pixel saturation. In order to normalise the intensity by the exposure times, linearity was demonstrated from 1 to 100 ms (Figure 4.4) on a solution of labelled native WPI.

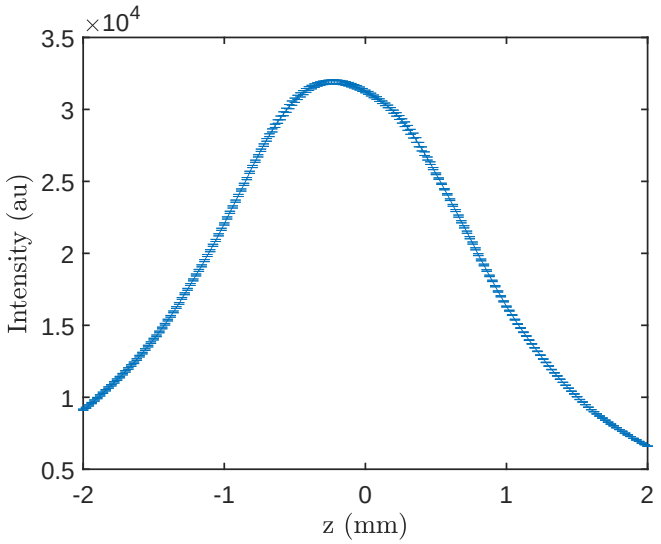

Figure 4.5: Fluorescence intensity of a RITC solution integrated on different thicknesses, plotted for different height values z with an Olympus objective 20x (NA 0.5)

Integration of fluorescence intensity over the thickness of the sample

In order to quantify the fluorescence intensity of a sample, the total intensity must be integrated over the entire thickness of the sample, which must be constant. A gene frame of 250 μm thickness was used and covered with a transparent coverslip. This integration depends on the optical properties of the objective. The evolution of the fluorescence intensity was studied for different focal plane positions in the sample and for different objectives. The result shows that magnifications of 20 $\times$ and 10 $\times$ allows the fluorescent signal to be integrated over the entire thickness of the sample, i.e. $I(x,y) = K \int_0^h c(x,y,z)dz$, where $I(x,y)$ was the fluorescence intensity collected on a pixel of the camera sensor at location (x,y), K a proportionality constant, $c(x,y,z)$ the local RITC concentration in the sample, and h the sample thickness. We need to ensure that the thickness over which the intensity signal was integrated (the depth of field) was greater than the thickness of the sample (250 μm). An Olympus objective with 20x magnification (NA 0.5) was chosen and we measured the fluorescence intensity of a RITC solution with varying the height z between z = -2 mm and z = 2 mm, z = o being the middle of the sample (Figure 4.5). The thickness of the sample is therefore probed for the range of z varying from -125 to +125 μm. We ensured that the intensity was constant from -125 to +125 μm, over the range of z accounting for the thickness of the sample. The thickness over the fluorescence signal is integrated is therefore greater than the thickness of the samples.

Calibration curve and protein mass quantification

The fluorescence intensity emitted by the fluorescent dye bounded to WPI was used to quantify the mass of proteins within an aggregate. A calibration curve was established by measuring the fluorescence intensity of successive dilutions of a highly concentrated solution of labelled native proteins. A calibration curve was made for

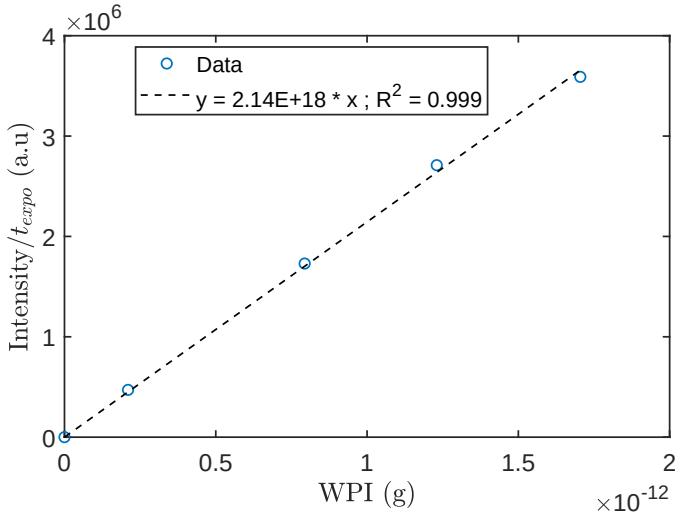

Figure 4.6: Calibration curve relating the intensity of fluorescence to the protein mass

each labelled WPI stock solution used prior aggregation. The fluorescence intensity was measured over the entire thickness of the sample. A set of images for each dilution was acquired and averaged. The resulting image for each dilution was analysed to extract the average intensity value. Each image was a set of pixels (x,y) containing an intensity value, $I(x, y)$, which are averaged to obtain an average intensity value per image. The average intensity value divided by the exposure time was plotted against the protein concentration. The linear coefficient relates the intensity to the protein concentration. To relate the intensity to the protein mass, the protein concentration must be multiplied by the volume of a pixel with $V_{pixel} = A_{pixel} * H_{integration}$. The integration height corresponds to the thickness of the gene frame and the area of a pixel was calculated according to the resolution of the objective used ($V_{pixel} = 2.02 \times 10^{-14}$ L with a x20 objective). The linear coefficient, a, relating the intensity to the protein mass will be used to convert the intensity of each pixel contained in the aggregates into protein mass (Figure 4.6).

4.2.6 Structural image analysis

Sample preparation

After heat-induced aggregation of labelled WPI solutions and subsequent gel formation, samples were cooled down and hand-sheared. A dilute solution of the sheared gel was performed. Several droplets of the diluted solution were deposited on a gene frame previously fixed on a glass slide, then sealed with a transparent coverslip.

Image analysis

On a sample, several hundred images were analyzed and several thousand aggregates were characterized. The sample contained in a 250 µm thick gene frame was thus

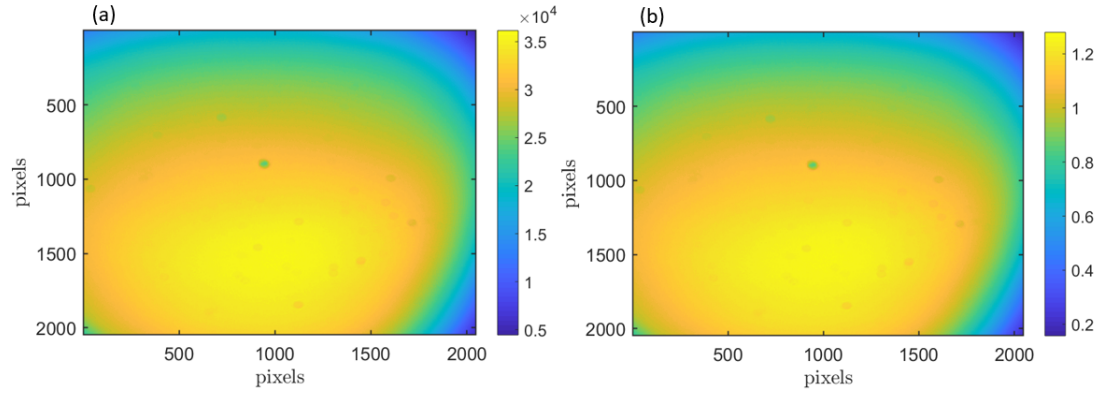

Figure 4.7: Averaged image of several images of a given labelled native WPI concentration solution (a) normalized by its mean value (b)

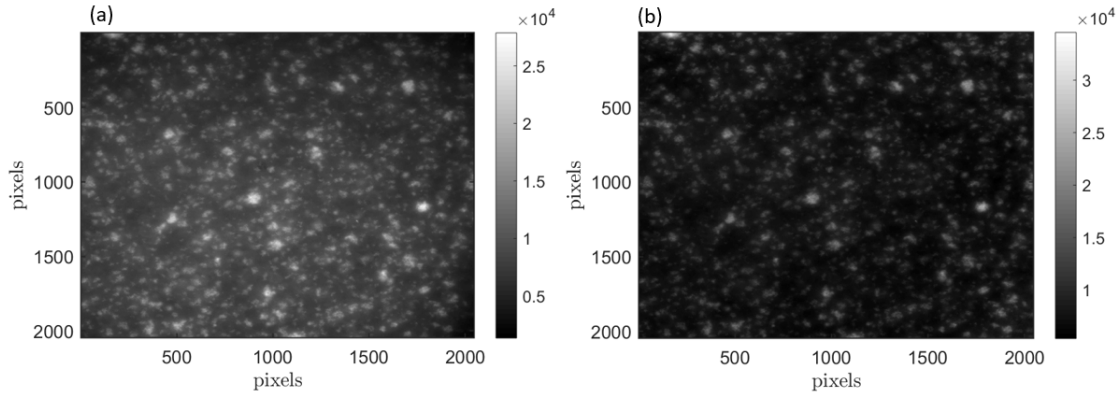

Figure 4.8: Image containing fluorescent aggregates (a) corrected from heterogeneity of illumination

scanned, along the x and y axes, by acquisition of images by fluorescence microscopy (Olympus IX 72). A sequence of several hundred images was then obtained, each image being a set of pixels whose intensity varied according to the concentration of labelled proteins. To correct the heterogeneity of the fluorescence intensity due to the illumination, each image containing aggregates was normalized. For this normalization step we used an image of the calibration curve averaged over several images and normalized by its mean value (Figure 4.7-b). The heterogeneity of fluorescence intensity was thus corrected (Figure 4.8).

Structural analysis

Based on the intensity difference between the labelled aggregates and the background, a threshold of the normalized image allowed its binarization and the detection of the aggregates' borders. The level of threshold should allow the detection of small aggregates and ensure the proper detection of their boundaries. Based on the boundaries detection, several parameters were thus determined as the minimum and maximum ellipsoidal length L_{min} and L_{max}, the aggregate perimeter, the area A and the coor-

dinates (x_c, y_c) of the centre of mass weighted by the protein mass contained in the pixel (x,y), $m(x, y)$. The radius of gyration R_g, the protein mass m contained in the aggregate, its density $\rho_{aggregate}$ and the anisotropy A_s were calculated based on their following expression.

The radius of gyration R_g is given by

$$R_g = \sqrt{\frac{\sum I(x,y)((x-x_c)^2 + (y-y_c)^2)}{\sum I(x,y)}}, \tag{4.1}$$

with $x_c = \frac{\sum m(x,y)x}{\sum m(x,y)}$, $y_c = \frac{\sum m(x,y)y}{\sum m(x,y)}$ and $I(x, y)$ the pixel (x,y) intensity.

The mass of proteins m in an aggregate:

$$m = \sum m(x,y) = \frac{\sum I(x,y)}{at_{expo}}, \tag{4.2}$$

where a is the coefficient obtained from the calibration of the fluorescence intensity.

The density in proteins $\rho_{aggregate}$:

$$\rho_{aggregate} = \frac{m}{\frac{4}{3}\pi R_g^3} \tag{4.3}$$

The shape anisotropy A_s:

$$A_s = \frac{L_{min}}{L_{max}} \tag{4.4}$$

All these properties, and in particular the radius of gyration, were defined so that they do not significantly depend on the particular threshold intensity value used to binarize the images, provided that the latter is small enough. Indeed, on the boundaries of the aggregates, the fluorescence intensity tends to zero. In fact, the image threshold is only useful to distinguish between an aggregate and another.

We have checked that the threshold level indeed did not significantly change the value of the radius of gyration. When varying the threshold level of ± 35% from the mean value (green line on (Figure 4.9), R_g values varied from 20.1 μm to 21.2 μm and protein mass varied from 1.68×10^{-9} g to 1.55×10^{-9} g. We can conclude that the threshold level, which is set by hand, leads to uncertainties which are less than 10%.

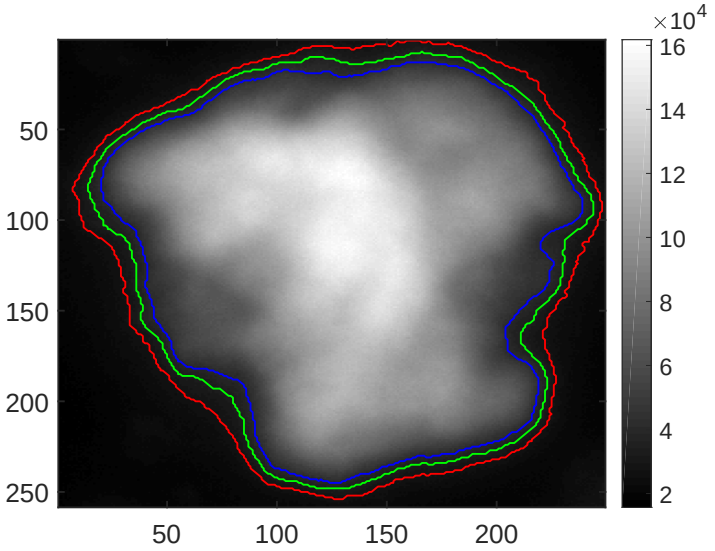

Figure 4.9: Fluorescent image of an aggregate with boundaries identified according to three different threshold levels (red: low threshold level, green: mean threshold level, blue: high threshold level). The scale bar gives the value of the pixel intensity normalized by the exposure time.

4.3 Results and discussion

4.3.1 Effect of RITC labelling on native protein and aggregate structure

The fluorescent dye concentration need to be sufficiently high to give a significant signal, but not too high in order to not modify the structure of aggregates. The structure of native proteins and aggregates after covalent labelling were compared to those without labelling and assessed by SAXS. Complementary information on the performed SAXS experimentation are provided in the section Small-Angle X-Ray Scattering in Chapter 4. We compared the effect of the covalent labelling on the scattering intensity spectra of native non-labelled dialyzed WPI and native labelled dialyzed WPI solutions (Figure 4.10-a). We did not have access to the Guinier regime for the native labelled WPI curve but we can deduced from a fit in the Guinier regime, as described in Materials and methods section, the size of the native WPI protein and we found $R_g \sim 10$ nm. The Kratky plot representation (q^2 I vs q) provides in turn insights on the internal structure (Figure 4.10 (a)). A bell-shaped curve is the signature of the globular conformation of proteins [93] and we found that the covalent labelling did not induce conformational changes in the structure of native proteins (Figure 4.10 (b)). Moreover, if we now compare the spectra of labelled aggregates and non-labelled aggregates of WPI, both dialyzed and aggregated in the same physico-chemical conditions in test tube (4% w/w WPI 10 mM NaCl 10mM $CaCl_2$ pH 7.0 during 15 min at 92°C), both representations (Figure 4.10 (c) and (d)) show no differences in the scattering intensity. The labelling procedure therefore did

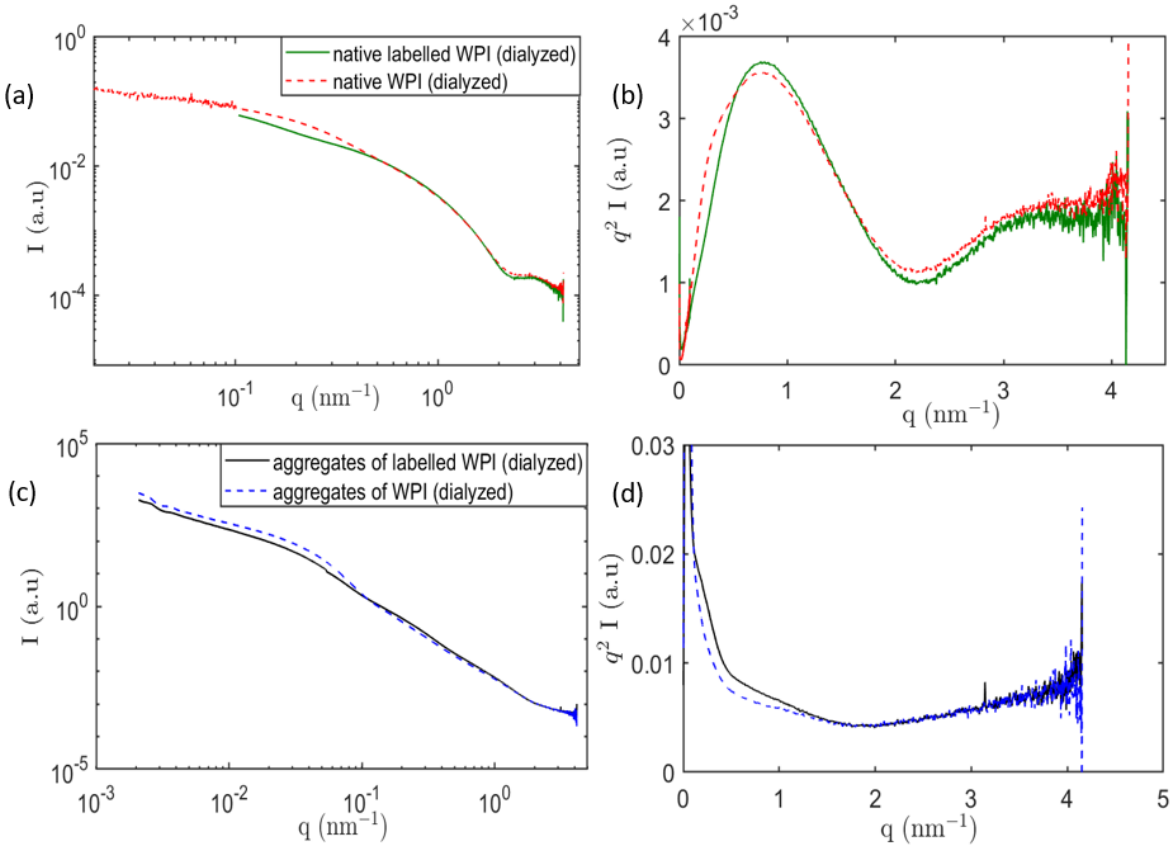

Figure 4.10: q-dependence of the scattering intensity normalized by the protein concentration and Kratky plot representation (q^2 I vs q) for native WPI solutions (a) and (b), labelled represented by a straight line and non-labelled represented by a dotted line, and for WPI aggregates (c) and (d), labelled represented by a straight line and non-labelled represented by a dotted line.

not result in structure variation for both native and aggregated proteins.

4.3.2 Heat-induced gelation of labelled WPI

The aim of the procedure was to characterise large WPI aggregates bigger than one micron in size. To produce large size WPI aggregates, a WPI gel was formed under heat treatment and then hand-sheared after samples were cooled down in an ice-bath. WPI gels were formed only above a critical protein concentration ($[WPI]_g$), which depended on the concentration of salts added. $[WPI]_g$ can therefore be lowered with increasing salt concentration [100]. $[WPI]_g$ was determined by visual observation after heating by the absence of flow when tilting the samples. Labelled WPI gels were formed under different physico-chemical (protein and NaCl concentrations) and heat treatment conditions to assess the consistency of the developed analysis technique. We investigated the structure of labelled WPI aggregates formed by heating labelled WPI solutions at pH 7 at $[WPI]$=6% w/w in the presence of 100 mM NaCl for 3 min at 92°C, at $[WPI]$=3% w/w in the presence of 120 mM NaCl for 45 min at

92°C and at $[WPI]$=3% w/w in the presence of 40 mM NaCl and 20 mM $CaCl_2$ for 3 min at 80°C (Table 4.1). It was reported that gelation temperature decreased with increasing protein concentration and increasing salt concentration [102], and that the rate of gelation and the gel strength were strongly dependent on the temperature, pH, protein concentration, and ionic strength [100]. Heat treatment have thus been varied according to the physico-chemical condition used. The gel formed at 3% w/w WPI in the presence of 120 mM NaCl for 45 min at 92°C (condition 2) was characterized by a more pronounced ability to flow compared to the others conditions and was in between a "liquid-like" system and a "gel-like" one. The physico-chemical condition used for this system was most likely just below the boundary with $[WPI]_g$.

Table 4.1: Conditions of heat-induced gel formation.

Condition	$[WPI]$	[NaCl]	[$CaCl_2$]	pH	Temperature	Heating time
1	6 % w/w	100 mM	0 mM	7.0	92°C	3 min
2	3 % w/w	120 mM	0 mM	7.0	92°C	45 min
3	3 % w/w	40 mM	20 mM	7.0	80°C	3 min

4.3.3 Statistical features of the protein aggregates

After the heating step, the protein gels were cooled down then hand sheared and diluted, which led to isolated aggregates of various size. We analyzed the properties of these aggregates, and in particular their radius of gyration, mass, density and shape anisotropy. Results were obtained from sequences of images containing approximately 5000, 8000 and 42500 aggregates respectively from condition 1, 2 and 3 (Table 4.1). We identified aggregates from 300 nm up to 100 μm with mass in proteins (M_w) ranging from 10^{-5} ng to 10 ng.

Figure 4.11 displays the probability density functions (PDFs) of the aggregate size. For the three condition tested, the PDFs were very similar, and were approximately described by an exponential distribution, of mean value of 4 μm. The very simple form of these PDFs indicated that the fragmentation of the gel was a Poisson point process (the fragmentation events occur continuously and independently of one another). This is surprising as it is likely that the fragmentation was more efficient for bigger aggregates than for smaller ones. However, it should be noticed that the PDF might not be exactly exponential, but was (at least for conditions 1 and 2) better fitted by a Weibull distribution, which can account for a size-dependent fragmentation [18]. When considering volume (or mass, not shown) averaged PDFs, they were will-fitted by a log-normal distribution. The average radius of gyration of the aggregates lied between 20 and 30 μm, and small differences between the experimental conditions could be observed.

The main interest of the present experimental approach was to determine the mass of the aggregates simultaneously as their radius. From these measurements, we computed the aggregate density. The PDFs of the density as displayed in Figure 4.12. The density distributions exhibited systematically a large peak between a few and one hundred g/L, depending on the experimental conditions, and on the type of averaging made (number, mass or volume weighted). This order of magnitude

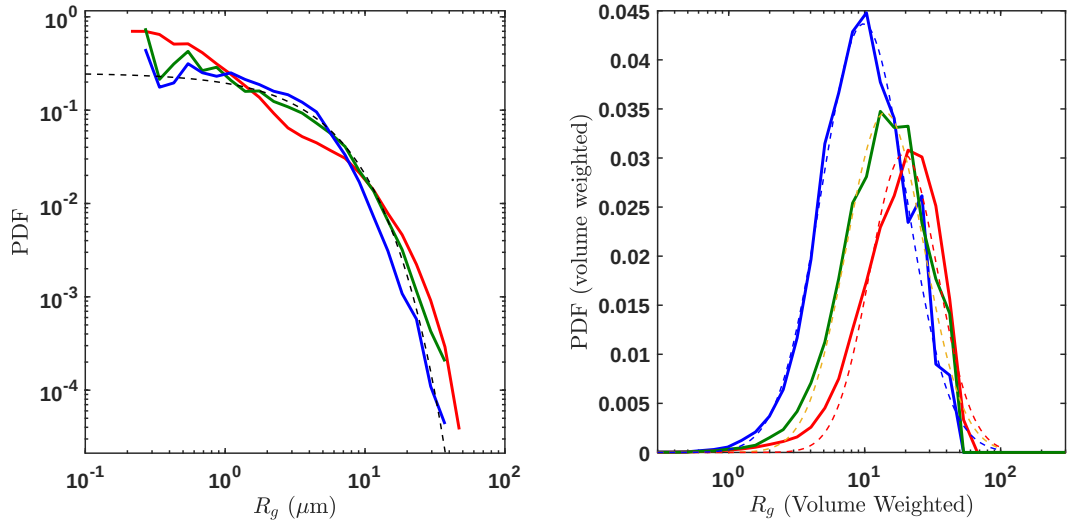

Figure 4.11: Probability density functions of the radii of gyration of protein aggregates formed at 6% w/w 100mM NaCl 3 min 92°C (cond. 1, blue), 3% w/w 120mM NaCl 45 min 92°C (cond. 2, green), 3% w/w 40mM NaCl 20mM $CaCl_2$ 3 min 80°C (cond. 3, red). *Left:* number weighted PDFs, fitted by an exponential law, of mean value 4μm. *Right:* volume weighted PDFs, fitted by log-normal distributions. Condition 1: mean-value 21.3 μm, standard deviation 16.7μm; condition 2: mean-value 27.0 μm, standard deviation 20.3μm; condition 3: mean-value 31.8 μm, standard deviation 22.7μm;

typically corresponded to the initial protein concentration, which is not surprising since the conditions used are in the vicinity of the sol-gel transition. As it will be discussed in the next section, these PDFs of the density hide a strong correlation between size and mass.

To finish with the statistical features of the aggregates, PDFs of the anisotropy parameter are displayed in Figure 4.13. They exhibited a large peak centered around 0.7. No significant correlation was found between this parameter and the aggregate size.

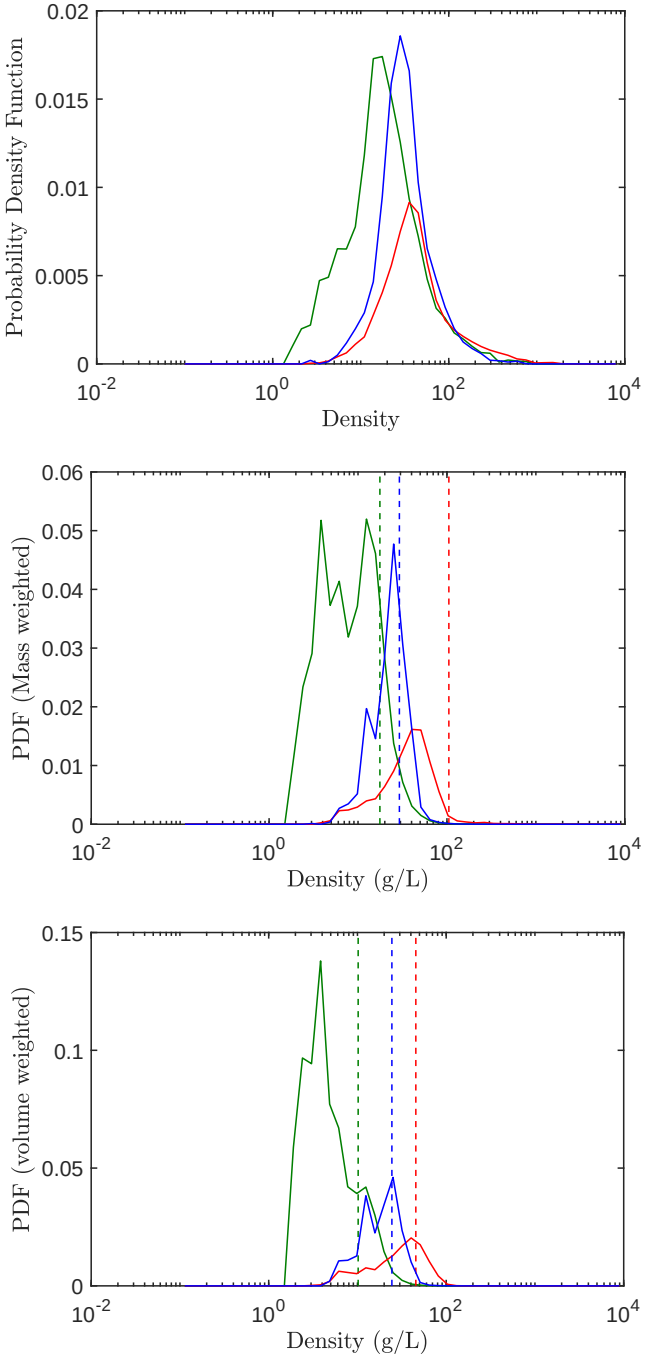

Figure 4.12: Probability density functions of the density of protein aggregates formed at 6% w/w 100mM NaCl 3 min 92°C (cond. 1, blue), 3% w/w 120mM NaCl 45 min 92°C (cond. 2, green), 3% w/w 40mM NaCl 20mM $CaCl_2$ 3 min 80°C (cond. 3, red). The dashed lines indicate the mean value.

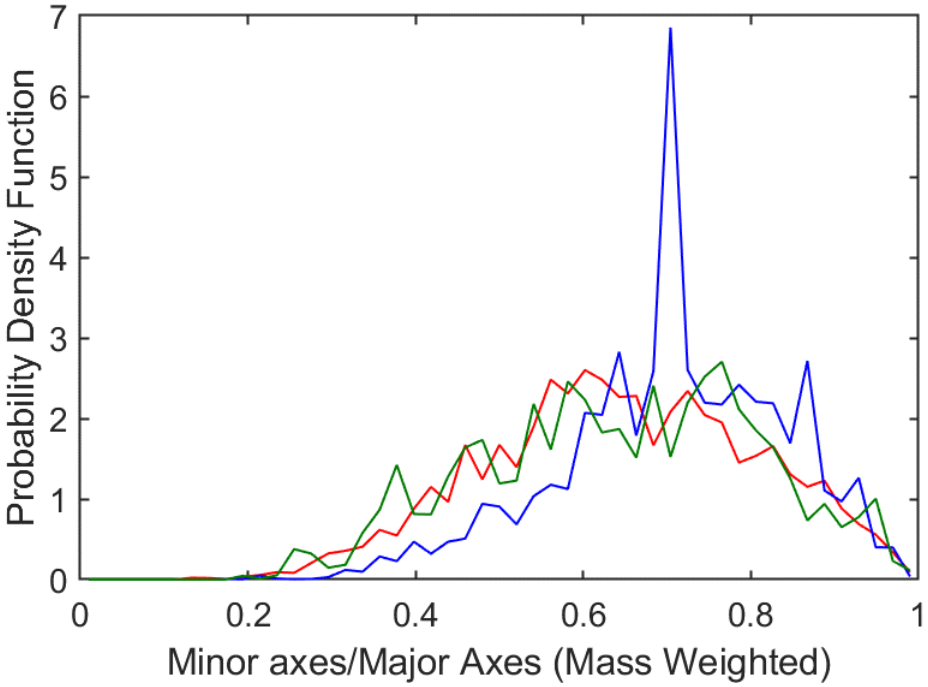

Figure 4.13: (a) : Probability Density Function of the anisotropy parameter (minor axis length over major axis length of an equivalent ellipsoid) of aggregates formed at 6% w/w 100mM NaCl 3 min 92°C (blue), 3% w/w 120mM NaCl 45 min 92°C (green), 3% w/w 40mM NaCl 20mM $CaCl_2$ 3 min 80°C (red).

4.3.4 Mass and size correlation

Fractal aggregates are featured by a branched structure and characterized by a power law relationship between their average molar mass (M_w) and radius (R_g) with $M_w = M_p(R_g/R_0)^{d_f}$, where d_f is the so-called fractal dimension, M_p the mass of a protein and R_0 the characteristic size of the structural elementary unit. The radius of gyration is one of the most commonly used sizes because it is a purely geometrical property of the cluster and can be easily determined by static scattering methods. The determination of the protein mass of each aggregate and of their radius of gyration was therefore used to ascertain the fractal dimension by plotting the protein mass versus the radius.

Figures 4.14 and 4.15 highlight the strong correlation between the size and mass of the protein. When considering an ensemble of aggregate of a given size, the standard deviation of their mass was greatly reduced, and when plotting their averaged mass with respect to the radius of gyration, a clear power law was evidenced below 10 micrometers, as expected for a fractal structure. For the three tested conditions the fractal dimension d_f equals to 2, consistently with previous studies [69, 75]. M_w of sub-micron aggregates ranged between 10^{-14} g and 10^{-12} and were consistent with M_w determined by Resonant Mass Measurement for fractal aggregates of $R_g \simeq 205$ nm [132]. In addition, we found $M_w \simeq 10^9$ g for $R_g \simeq 300$ nm of WPI aggregates, which is coherent with molar mass of β-lg aggregates found by Inthavong et al. [52].

For condition 2 (which is just below the sol-gel transition), the fractal dimension of 2 hold over the whole range of radius of gyration investigated, i.e. over three decades. By contrast, the two other ones exhibited a clear kink at $R_g \simeq 7\mu$m. Above this value the fractal dimension significantly increased. The best power-law fit to the data led to $M \sim R_g^{2.7}$, a value which is close to 3, i.e. that of a dense assembly. By construction, and using the same data, the aggregate density displayed in Figure 4.15 decreased when increasing the radius of gyration with a -1 power law. For condition 1 and 3, the density saturates for $R_g > 7\mu$m, and reached a value of 25 and 10 g/L, respectively.

Let us now discuss these results.

The fact that there existed a cut-off length scale for the aggregation conditions which were above the sol-gel transition can be interpreted as the result of the percolation of the aggregates. Indeed, in dilute conditions, aggregation leads to fractal aggregates. Upon heating, proteins are first denatured, then associate to form well-defined primary aggregates which further associate randomly to form aggregates with a self-similar structure characterized by a fractal dimension, if electrostatic repulsions are lowered down by increasing salt and protein concentrations [88]. If the concentration is high enough, the aggregates grow in size and start to interconnect with one another until they fill up the whole volume and the colloidal system may percolate to form a gel network. A "liquid-like" system is turned into a "gel-like" one, characterized by the divergence of the system's viscosity.

When increasing either the protein concentration or the salt concentration and varying heat treatment (condition 1 and 2 Table 4.1), a a two-slope behavior was established with a cut-off length around 10 μm (Figure 4.14). Aggregates below 10

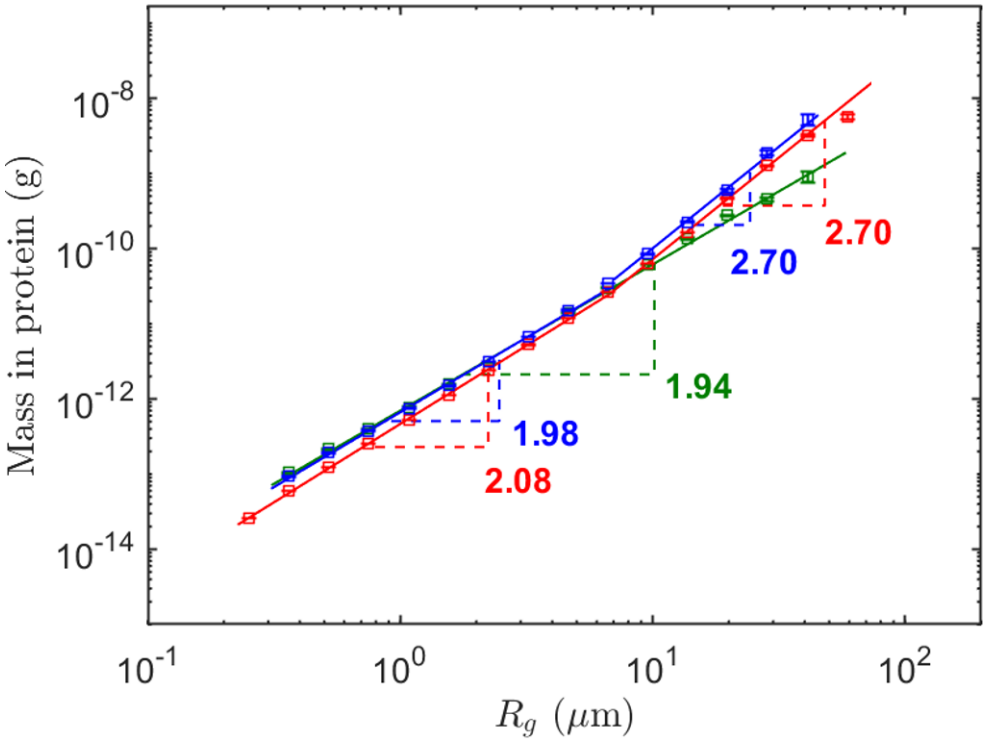

Figure 4.14: Dependence of the protein mass of aggregates formed at 6% w/w 100mM NaCl 3 min 92°C (blue), 3% w/w 120mM NaCl 45 min 92°C (green), 3% w/w 40mM NaCl 20mM $CaCl_2$ 3 min 80°C (red) on the radius of gyration. Fractal dimension are deduced from the slopes. The standard error of the mean are plotted.

μm were characterized for all the conditions by a fractal dimension d_f = 1.9-2.0 and by a decreased density with increasing radius. The internal structure defined by the fractal dimension of aggregates remained the same. When the radius of gyration increased above 10 μm, R_g increased with increasing M_w following a power law characterized by d_f = 2.7 and larger aggregates become denser and more compact as their size increases above few microns.

For these two conditions (1 and 3), increasing initial protein concentration and salt concentration lead to an increase of protein concentration and aggregate size during aggregation. With increasing protein concentration and increasing aggregate size, interparticle distance between aggregates is further reduced. As the fractal dimension we deal with here are not far from 2, aggregates can interpenetrate more strongly. The shear-induced breakage of the aggregates reveals the internal structure of the small aggregates constitutive of the larger ones. Larger aggregates ($R_g \geq 10$ μm) are characterized by denser structure and a density which became independent on the aggregate size. This interpretation is consistent with the fact that condition 1 and 3 were above the sol-gel transition, contrary to condition 2 which was slightly below.

In order to form large aggregates of more than a few microns, while preserving their fractal character and $d_f = 2$, one should avoid interpenetration of the aggregates

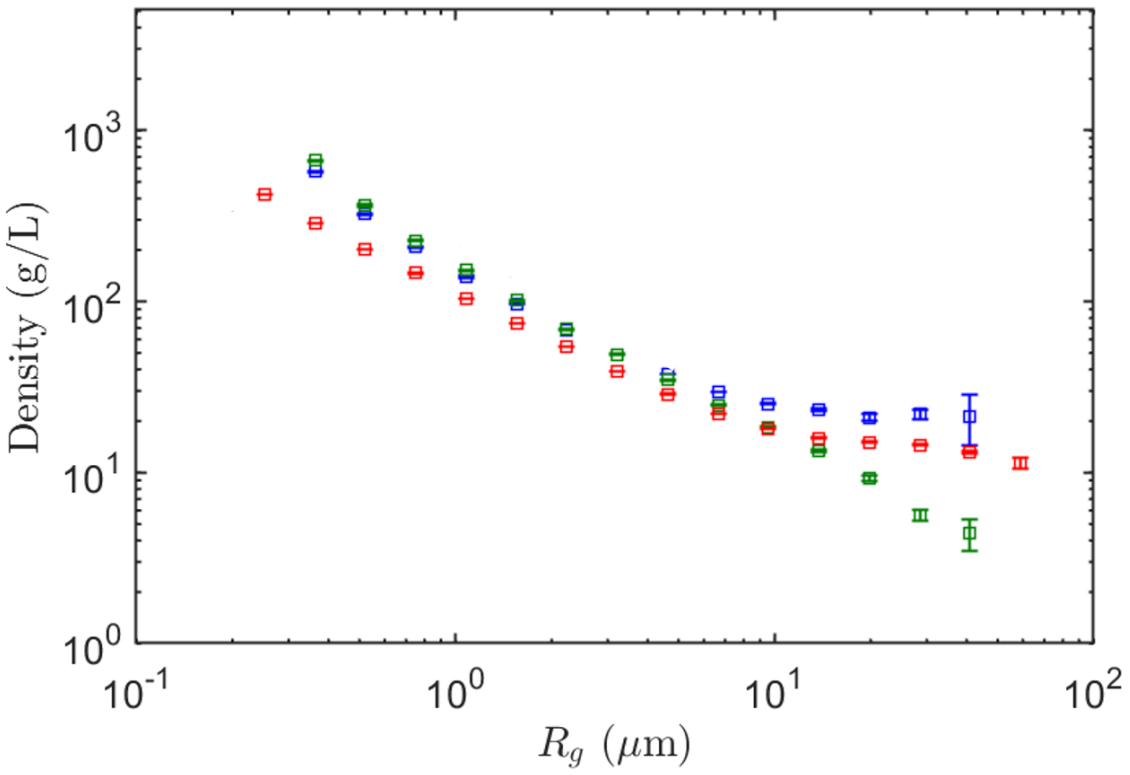

Figure 4.15: Protein density of aggregates formed at 6% w/w 100mM NaCl 3 min 92°C (blue), 3% w/w 120mM NaCl 45 min 92°C (green), 3% w/w 40mM NaCl 20mM $CaCl_2$ 3 min 80°C (red) on the radius of gyration. The standard error of the mean are plotted.

to prevent the percolation of the system and the "blobs" densification.

Results here were consistent with the theory that the primary structure of the gel is fixed, with afterwards more protein being incorporated onto the gel network, leading here to a densification of the later structures. Here we did not attempt to give a full analysis of these results, but simply show the main trends and assess the consistency of our quantitative analysis technique and method.

4.4 Conclusion

The structure of large WPI aggregates formed after heat-denaturation at neutral pH in the presence of salts was studied using a quantitative structural analysis of fluorescent microscopy images through a covalent labelling reaction between WPI and RITC. This covalent labelling permitted to relate the fluorescence intensity of RITC to the protein concentration and thus to the mass of proteins inside an aggregate. Structural characterization of micron-sized aggregates, including their mass, density, size and shape anisotropy was therefore performed, enabling the overcome the size limitation of the previous used techniques. The fractal dimension of aggregates within two decades of sizes below 10 μm was equal to d_f=2, and consistent

with others experimental techniques. However, we found an increase of the fractal dimension when increasing aggregates sizes over one decade above 10 μm, reflecting a densification of proteins mass in the aggregates. This densification may be related to an increased level of interpenetration of the aggregates due to increased number of bonds and bonds strength, and leading to a compaction of the structure with increasing scale level.

- A quantitative structural analysis of heat-induced WPI aggregates by covalent labelling and fluorescent microscopy was developped.
- Structural characterization of micron-sized aggregates, including their mass, density, size and shape anisotropy was performed.
- The range of sizes over which $d_f = 2$ can be extended with the aggregation conditions (from 10 to 50 μm).

Chapter 5

Hydrodynamic spinning of WPI aggregates

To go beyond aggregation conditions in which the size of the aggregates is micrometric, we developed a millifluidic process which permitted us to fabricate fibers of fractal aggregates. The process was based on a co-axial flow focusing device. The inner jet was a suspension of sub-micrometric aggregates just below the sol-gel transition. The sol-gel transition was induced in the jet by the co-flow of a solution of calcium. The calcium ions gelled the jet by a well-known mechanism of salt-induced gelation. We discussed the hydrodynamic and physico-chemical conditions which controlled the formation and the stability of the fibers. Surprisingly, the fibers had a core-shell structure.

Contents

5.1 Introduction

Significant research work has been conducted on studying how whey proteins aggregation impacts on specific colloidal structure at the micro scale and contribute to its macroscopic properties [52, 89]. It has been shown that heat-induced protein aggregation can influence texture in two different ways. On one hand, by turning aqueous solutions into soft solids by forming a space filling network, through a gelation process. On the other hand, through the controlled structural characteristics of the particles forming a stable suspension of aggregates [52].

The viscous behavior of the suspension of aggregates strongly depends on their structure, size and concentration [52]. Four types of stable suspensions of aggregates can be formed by heat-induced aggregation: long semi-flexible (amyloid-type) fibrils, flexible strands, dense spherical particles called microgels and fractal aggregates, depending on the physico-chemical conditions (pH, type and concentration of salts, protein concentration) and the heating conditions (temperature and heating time). Fractal aggregates are featured by a opened and branched structure and characterized by a power law relationship between their average molar mass (M_w) and radius (R) with $M_w = M_p(R/R_0)^{d_f}$, where d_f is the so-called fractal dimension and R_0 the characteristic size of the structural elementary unit. The average density, which is the ratio of the mass to the volume, varies consequently as R^{d_f-3} and subsequently decreases with increasing radius. This structural parameter, which relates the structure of the aggregates to their volume, leads to different functional properties. Spherical objects, such as microgels ($d_f = 3$), occupy a lower volume fraction at a given protein concentration [112]. Conversely, objects of lower fractal dimension occupy a higher volume fraction for the same quantity of matter. Fractal and linear objects are so more interesting in order to increase the viscosity or to induce gelation at lower protein concentration [128].

The extreme situation is where fibers are used. They are characterized by an elongated dimension with a high axial ratio with a fractal dimension of 1. First they will occupy a larger volume in the solution because their hydrodynamic radius is larger ($d_f = 1$) and are subsequently interesting for tailoring the rheology of suspensions [96]. They are also good candidates for drug delivery systems because of their high surface-to-volume ratio. Additionally, fibers can interconnect with each other and create a network. They have been barely exploited in food applications [119, 143] despite their wide range of applications in materials science [42, 48].

Our objective was to show that whey protein isolate (WPI) aggregates can be structured at microscopic scales into fibers. We used a simple millifluidic co-flow device in which sub-micrometric aggregates were used as building blocks to shape fibers by Ca^{2+}-induced gelation. We discussed the conditions in which aggregates can be successfully shaped into fibers in regards to the hydro-dynamical and physico-chemical conditions.

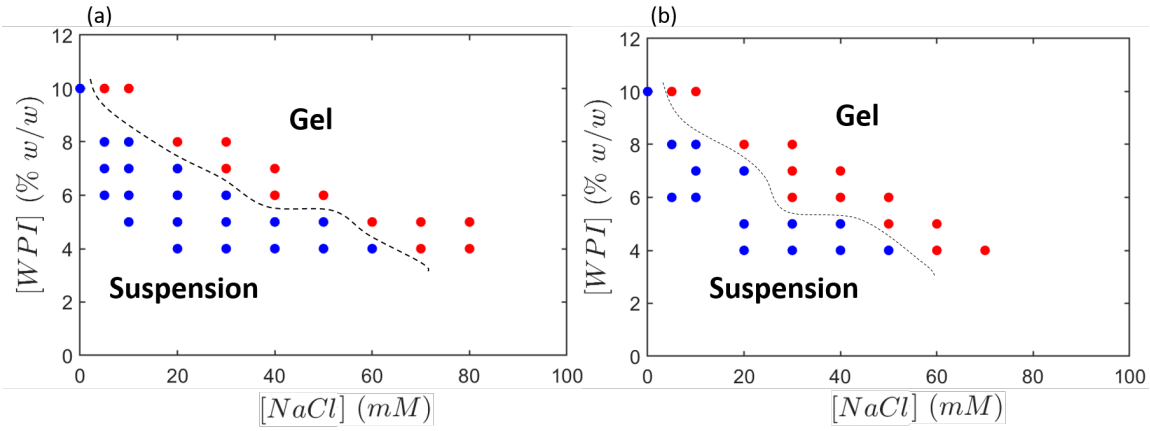

Figure 5.1: State diagram and sol/gel transition of suspensions of aggregates as a function of the concentrations of WPI and NaCl used to prepare the suspension at pH 7.0. Each solution was heated at 92°C during (a) 30 min and (b) 60 min.

5.2 Materials and methods

5.2.1 Materials

WPI aggregates

A WPI stock solution of 15% w/w was prepared by dispersing the WPI powder in demineralized water (0.3-0.9 μS/cm). Details concerning the composition of WPI powder can be found in Chapter 2. Sodium Azide (0.02% w/w, Sigma-Aldrich CAS 26628-22-8) was added to the solution to prevent bacterial growth. The solution was gently stirred for 12 h up to complete dissolution of WPI powder at 4°C. The concentration of the WPI solution was measured by UV absorption at 280 nm with an extinction coefficient of 1.0061 L/g/cm. Finally, demineralized water and sodium chloride (1 M, CAS number 7647-14-5) was added to obtain a 8% w/w WPI solution with a NaCl ionic strength of 10 mM, and pH is adjusted at 7.0 by the addition of sodium hydroxyde (1 M, CAS number 1310-73-2). 10 mL pyrex tubes were filled with the WPI solution and heated at 92°C during 30 min, cooled down in ice bath and kept at 4°C during one night. Suspensions of aggregates of different protein concentration and constant size were prepared either by diluting the suspension with demineralized water or by by heating it in an oven, during several hours at 30°C, to concentrate it by water evaporation, in order to obtain suspension of protein concentration $[WPI]$ ranging from 6.6 to 10% w/w. The hydrodynamic radius R_h was measured by dynamic light scattering using a Vasco Cordouan Technologies at λ=658 nm and we found R_h = 70 nm. Density was found to be equal to 1, $[WPI]$ expressed in % w/w were therefore equivalent to g/L.

Preparation of calcium ions solutions

Solutions of $CaCl_2$ were prepared from $CaCl_2$,$2H_20$ powder purchased from Sigma-Aldrich (CAS number 10035-04-8). A $CaCl_2$,$2H_20$ stock solution of 60% w/w ([$CaCl_2$]

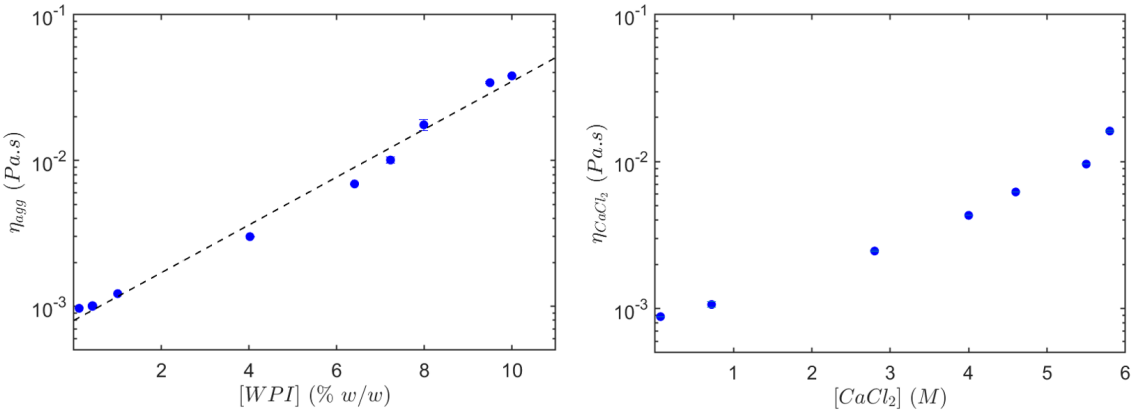

Figure 5.2: Viscosity of solutions used for the fabrication of fibers. Left: Shear viscosity of suspension of aggregates as a function of the mass fraction of WPI aggregates. The initial suspension ($[WPI]$ = 8 % w/w, R_h = 70 nm) was diluted or concentrated. Dashed line: $\eta_{\text{agg}} = 0.8 \times 10^{-3} \exp([WPI]/2.65)$. Right: Shear viscosity of $CaCl_2$ solution as a function of the concentration of $CaCl_2$. Error bars represent the standard deviation and are less than the size of the symbols.

= 5.9 M) was dissolved in demineralized water and diluted from 5.9 M to 34 mM. We defined R_m as the molar ratio between [Ca^{2+}] and $[WPI]$, R_m = [Ca^{2+}]/[WPI], which varied from 8 ([$CaCl_2$] = 34 mM) to 1558 ([$CaCl_2$] = 5.9 M). We considered an average molar mass for WPI of 17.5 kDa [61]. Preliminary to experiments of fiber formation, we did a phase-diagram showing the sol-gel transition as a function of $[WPI]$ and [$CaCl_2$] for two different heating times (Figure 5.1). As expected, the concentration of NaCl required to induce the sol-gel transition increased when the concentration of WPI decreased.

5.2.2 Rheological characterization

The viscosity of the suspensions of aggregates and calcium solutions was measured by standard rheometry (MARS, HAAKE) with a plate-plate geometry at 23°C. This geometry was chosen in regards to the small quantities of samples available. The temperature was controlled by a Peltier system. The suspensions were pre-sheared at 10 s^{-1} during 30 s to homogenize the sample. The viscosity was measured as a function of the shear rate $\dot{\gamma}$ (from 10 s^{-1} to 100 s^{-1}). Each measurement has been replicated twice to four times. After ensuring the Newtonian behaviour of the samples, viscosity values were taken at $\dot{\gamma}$ = 100 s^{-1} and plotted as a function of the concentration (Figure 5.2). In agreement with [52], the viscosity of the suspension of aggregates increased exponentially with the concentration of WPI.

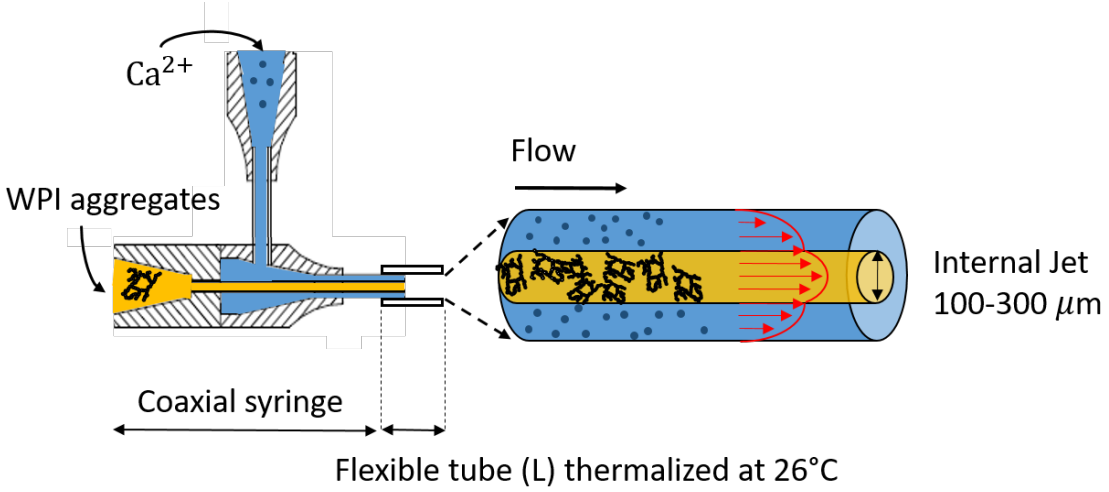

Figure 5.3: Schematic of the co-axial flow focusing device used to produce WPI aggregates fibers by Ca^{2+}-induced gelation. The co-axial needle was connected to a tube. The tube was immersed in a bath at constant temperature (26°C). The fibers were collected in a petri dish. The suspension of WPI aggregates was injected via the inner needle (yellow), whereas the solution of calcium was injected by the outer needle (blue).

5.2.3 Fiber formation in a co-axial flow focusing device

Fibers of pre-formed WPI aggregates were produced in a microfluidic co-flow device thanks to a salt-induced cold gelation process.

The co-axial flow focusing device was based on two well-centered co-axial needles (Ramé-Hart) in which the inner central flow was surrounded by an external flow coming from the outer needle (Figure 5.3). The inner flow was composed of WPI aggregates (η_{agg}, Q_{agg}) while the outer flow was composed of a $CaCl_2$ solution (η_{CaCl_2}, Q_{CaCl_2}. The internal and external diameters of the inner needle were 178 μm and 356 μm, respectively. The internal and external diameters of the outer needle were 584 μm and 889 μm, respectively. Both needle were connected to syringe pumps (neMESYS, CETONI). The total flow rate $Q_{total} = Q_{agg} + Q_{CaCl_2}$ ranges from 8.33 $\times 10^{-9}$ m^3/s to 5×10^{-8} m^3/s. The outer needle was connected to a Fluorinated ethylene-propylene flexible tube (Fluigent) of internal diameter $d = 754$ μm, immersed into a water-bath with a controlled temperature of 26.5°C. The tube length ranged from 11.3 to 226 cm in order to keep constant the residence time. The fibers were then collected in a external solution whose whose composition will be presented later.

Fibers were formed under laminar flow conditions and the control parameters were the total flow rate, Q_{total}, the ratio of the outer to the inner flow rates Q_{CaCl_2}/Q_{agg} which both tune the residence time and the size of the internal jet and consequently the size of the fiber. The ratio of the outer to the inner flow rates could therefore modify the aggregation structure by varying the diameter of the inner jet. The global

residence time t_{global} is expressed as

$$t_{\text{global}} = \frac{\pi d^2 L}{4Q_{\text{total}}} \tag{5.1}$$

The flow rate of the outer and inner phase being different, the flow velocity of the two phases was non uniform. In a permanent laminar regime, the flow velocity field in a cylindrical capillary of length L and of radius R is defined as a parabolic velocity profile and is expressed as

$$v_z = \frac{\Delta P}{4L\eta}(R^2 - r^2) \tag{5.2}$$

The following equations are presented to outline how the flow rates ratio influences the size of the internal jet given that the shaping of the flow is ensured by the laws of hydrodynamics. For steady state conditions and in-compressible, interialess flow, the dynamics is governed by the Stokes equations:

$$\overrightarrow{\nabla} p = \overrightarrow{\nabla} \cdot \underline{\underline{\sigma}} \tag{5.3}$$

with p the pressure and $\underline{\underline{\sigma}}$ the stress tensor. The mass conservation law is expressed as

$$\overrightarrow{\nabla} \cdot \overrightarrow{v} = 0 \tag{5.4}$$

In the case of Newtonian fluids flow, the stress is expressed as: $\underline{\underline{\sigma}} = \eta \overrightarrow{\nabla} \overrightarrow{v}$, with η the viscosity of the fluid. The boundary conditions were the following: the continuity of velocities and stresses at the interface between the two fluids and the non-slip conditions at the wall. The Poiseuille profile is defined in two parts, with a discontinuity of slope at the interface due to the difference of viscosity between the two phases. The pressure gradient is invariant along the transverse axis, with $R_{interface}$ the position of the interface between the two fluids and R the internal radius of the flexible tube in which in inserted the co-flow syringe, we write the flow velocity of the inner phase as :

$$v_z(r) = \frac{\Delta P}{4L\eta_{\text{agg}}}(r^2 - R^2_{\text{interface}}) + \frac{\Delta P}{4L\eta_{\text{CaCl}_2}}(R^2_{\text{interface}} - R^2) \tag{5.5}$$

for r between zero and the position of the interface

and the flow velocity of the outer phase as :

$$v_z(r) = \frac{\Delta P}{4L\eta_{\text{CaCl}_2}}(r^2 - R^2) \tag{5.6}$$

for r between the position of the interface and the internal radius of the flexible tube.

Relating the velocity field to the corresponding flow rate with integration of the velocity field on the respective surface, the inner and outer flow rates are expressed as :

$$Q_{\text{inner}} = \frac{\pi \Delta P R^2_{\text{interface}}}{4L}\left(\frac{R^2_{\text{interface}}}{2\eta_{\text{inner}}} + \frac{R^2 - R^2_{\text{interface}}}{\eta_{\text{CaCl}_2}}\right) \tag{5.7}$$

$$Q_{\mathrm{CaCl_2}} = \frac{\pi \Delta P}{8 L \eta_{\mathrm{CaCl_2}}} (R^2 - R_{\mathrm{interface}}^2)^2 \tag{5.8}$$

We can now express the diameter of the inner jet and the pressure gradient as a function of the control parameters $Q_{\mathrm{CaCl_2}}$ and Q_{agg}:

$$\frac{\Delta P}{L} = \frac{8 \eta_{\mathrm{CaCl_2}} Q_{\mathrm{agg}}}{\pi R^4 (1 - x^2)} \tag{5.9}$$

$$x = \sqrt{\frac{\alpha - 1}{\alpha - 1 + m}} \tag{5.10}$$

with $\alpha = \sqrt{1 + \frac{\eta_{\mathrm{CaCl_2}}}{\eta_{\mathrm{agg}}} \frac{Q_{\mathrm{agg}}}{Q_{\mathrm{CaCl_2}}}}$ and $x = \frac{D_{\mathrm{inner}}}{D_{\mathrm{tube}}}$, D_{tube} being the internal diameter of the flexible tube. The size of the inner jet can therefore be varied according Eq. 5.10 and decreases with increasing flow rate ratio.

5.2.4 Characterization of fibers

Fibers were characterized under optical microscopy. The images were acquired with an Olympus IX70 microscope and a Hamamatsu ORCAFLASH high sensitivity camera (12 bits) with an Olympus objective 4× or 10× when studying the effect of flow rate ratio. The light source was a white light LED. Their diameter was measured by image analysis and evolution of their structure was recorded by image sequence. En error estimation of 10% of the diameter mean value have be considered.

5.3 Results and discussion

Shaping of gelled fibers under flow relies on two simultaneous key steps: the shaping by hydrodynamics and gelation through radial diffusion of the calcium ions. The right hydrodynamics parameters had to be found to induce the shaping of continuous fibers, as well as the right physico-chemical parameters for the gelation to occur within the flow residence time. Firstly, we studied the effect of hydrodynamics parameters such as the total flow rate and the ratio of the outer to the inner flow rates. The residence time in the tube was fixed in this study.

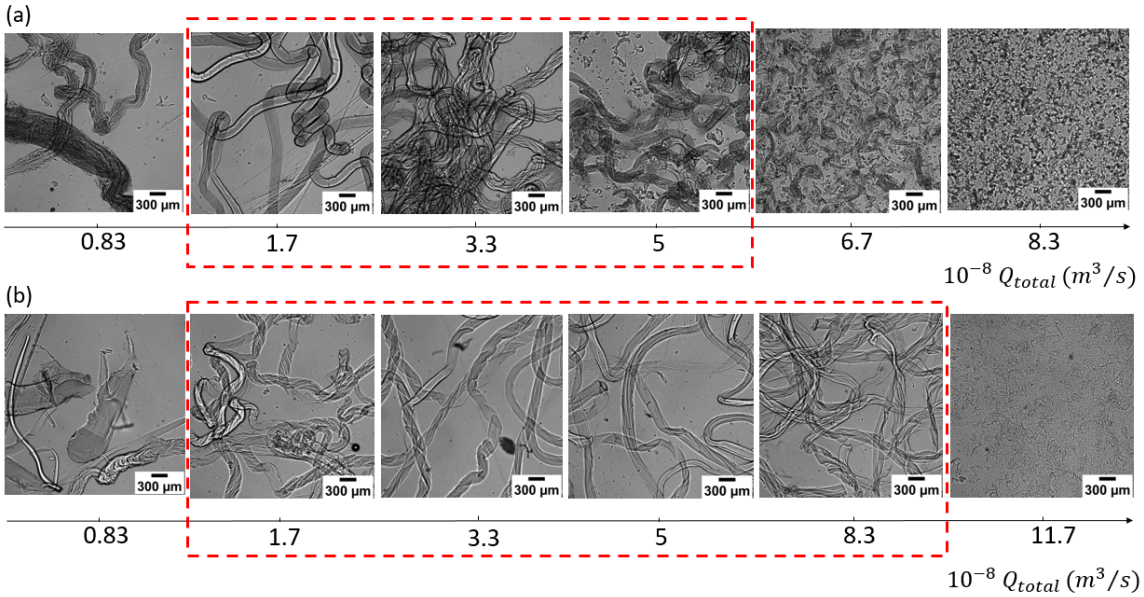

Figure 5.4: Effect of the total flow rate Q_{total} on fiber formation for a fixed residence time (t_{global} = 6 s). Fibers were collected in the $CaCl_2$ solution used for their fabrication. $[WPI]$ was fixed at 8% w/w. (a) Molar ratio R_m = 17 and [$CaCl_2$] = 68 mM. (b) R_m = 335 and [$CaCl_2$] = 1.5 M. Fibers were obtained for a range of Q_{total} that is outlined by the red dotted boxes.

5.3.1 Hydrodynamic conditions for the spinning of aggregates

We studied the effect of the total flow rate, Q_{total}, on the formation of fiber within the flow. Other hydrodynamics parameters, ratio of the outer to the inner flow rates and flow residence time were kept constant : $Q_{CaCl_2}/Q_{\text{agg}} = 10$ and $t_{\text{global}} = 6$ s. The length of the flexible tube was thus varied from L = 11.3 to 158.4 cm. This approach allowed us to keep the internal jet size constant and to vary only the average flow velocity. The study was conducted for two values of molar ratio R_m in order to evaluate the effect of the molar ratio on the influence of the total flow rate. Molar ratio were varied for the same suspension of aggregates ($[WPI]$ = 8% w/w) : R_m = 17, [$CaCl_2$] = 68 mM and R_m = 335, [$CaCl_2$] = 1.5 M. After the flow, the samples were collected from the flexible tube into a petri dish filled with the $CaCl_2$ solution used to produce the fibers. Total flow rate ranged from 0.83×10^{-8} m^3/s to 11.7×10^{-8} m^3/s.

At low total flow rate ($Q_{total} \leq 8.33\times10^{-9}$ m^3/s), discontinuous pieces of gels were produced for both molar ratios (Figure 5.4). Visual inspection of the flexible tube showed that these pieces of gels were produced by clogging of the nozzle: large aggregates were formed and stick at the outlet of the co-flow device and came off randomly with the flow. However, some fibers were still produced between the production of large sections of gel.

Above a critical value of flow rate (5 or 8.3 ×10^{-8} m^3/s), pieces of gel were again

produced instead of continuous fibers. To understand the origin of this mechanism, we define the Reynolds number as $Re = Q_{total} d_{\text{outer}}/\nu$, where d_{outer} is the internal diameter of the flexible tube and ν the kinematic viscosity of the fluid. The flow was always laminar even at the largest flow rates used in this study ($Re \leq 150$), which excluded the destabilization of the inner jet by flow instabilities. Another mechanism which could explain this breakage was the existence of a zone of extensional flow at the outlet of the co-axial needle. We could speculate that at large Q_{total}, extensional stress was sufficient to break the fiber under gelation. The fiber could not develop sufficient strength to resist to the stress. Consequently, the fiber could be therefore broken by the elongational stress imposed by the flow. Moreover, increasing molar ratio enabled fiber formation at higher total flow rate as the mechanical strength of the fiber increased with gelation rate, allowing the fiber to hold out the stress.

In the intermediate range of flow rates, fibers of about 300 μm diameter were formed in less than 10 s (red dotted line boxes in Figure 5.4). The physical principle of the formation of fiber relied on the radial diffusion of the calcium ions toward the aggregates confined in the inner jet, which induced their gelation. In fact, aggregates of 70 nm hydrodynamic diameter did not diffuse out, in contrast with calcium ions, which diffused out with a rate thousands times faster. The characteristic diffusion time of calcium ions over the radius of the fibre r_f is given by $t_{\text{diffusion}} \simeq r_f^2/D$ with r_f the radius of the fiber and D the diffusion coefficient of $CaCl_2$ ($\simeq 10^{-9}$ m^2/s in water). $t_{\text{diffusion}}$ was of the order of 10 s and was so equivalent to the residence time of the fiber in the flow. However, this analysis cannot explain by itself that we obtained stable fibres in less than 10 s, as we have also to consider the kinetics of reaction of Ca^{2+} with WPI aggregates.

Ca-induced gelation of WPI aggregates is also a thermally activated process [61]. Compared to monovalent ions, such as NaCl, divalent ions have three effects on protein aggregation / gelation: (1) to shield electrostatic interactions by lowering the effective charge density and thus decreasing electrostatic repulsion, (2) to form site-specific inter-molecular salt bridges between negatively charged groups on two (partially) unfolded protein molecules and (3) to induce conformational change leading to altered hydrophobic interactions [117]. Rheometrical study of the gelation of WPI aggregates with $CaCl_2$ [61] gave us some useful insights on the characteristic times of the reaction. The time at which appeared the sol-gel transition depended on the temperature, the concentrations of WPI and $CaCl_2$. The elasticity of the gel increased very steeply close to this time and then slowly on long time scales (several hours). In the range of concentrations used in our study, the gelation time should be of the order of 10^3 - 10^5 s according to [61] if both solutions were well-mixed. It was so very surprising to obtain stable fibers in less than 10 s. One scenario to explain our observations could be the formation of a shell around the fibre that stabilized it against hydrodynamic forces. Consequently, the inner content of the fibre should be only partially gelled after 10 s. The question of the storage of the fibre in calcium solution to prolong the gelation will be analyzed hereafter.

The fiber formation was thus reduced within a range of flow rate. It was worth to note that the velocity range of fiber formation depended on the molar ratio and therefore the gelation rate. In the following sections, fibers were formed under a fixed

total flow rate $Q_{\text{total}} = 3.33\times10^{-8}\ m^3/s$ during a residence time $t_{global} = 6$ s ($L = 0.46$ m) at a temperature T = 26°C.

5.3.2 Fibres diameter and hydrodynamic parameters

Secondly, we studied the influence of the flow rate ratio on the fiber diameter D. Fibers were formed for two molar ratio $R_M = 17$ ($CaCl_2 = 68$ mM) and 641 ($CaCl_2 = 2.9$ M). $Q_{\text{CaCl}_2}/Q_{\text{agg}}$ ranged from 1 to 100. Fibers were collected in a solution of $CaCl_2$, whose the concentration was the same than the one used to produce the fiber. The diameter was measured after 20 min of storage of the fibers in this solution. We compared the diameter of the fibre to the theoretical expression which gives the diameter of the jet in the co-axial flow focusing device (Eq. 5.10). From this expression, we expected that the size of the inner jet should decrease with increasing flow rate ratio $Q_{\text{CaCl}_2}/Q_{\text{agg}}$ for a fixed value of Q_{tot}. The diameter of the fibers formed at the lowest concentration of $CaCl_2$ ($R_M = 17$) decreased with the flow rate ratio, Figure 5.5. The agreement with the hydrodynamic law was excellent (red dashed line). Continuous and stable fibers were formed at $R_M = 17$ with a diameter which decreased from 300 to 100 μm when $Q_{\text{CaCl}_2}/Q_{\text{agg}}$ increased. This comparison with hydrodynamic laws suggested that fibers formation and resulting diameter were governed by the hydrodynamic conditions.

However when $Q_{\text{CaCl}_2}/Q_{\text{agg}}$ was larger than 40, continuous and stable fibers were no longer produced. We can reasonably speculate that the decreased of $Q_{\text{CaCl}_2}/Q_{\text{agg}}$ induced an increase of the extensional stress in the hyperbolic contraction after the needle. Increasing the ratio of flow rate resulted in an increase of the stress applied on the inner jet and might result in breakage and inability to form gelled fibers. It suggested that very small fibers could be very difficult to obtain without changing the geometry of the co-flow device in order to minimize the extensional stress.

However, it was interesting to compare these results with those obtained with a higher molar ratio R_M. When increasing R_M to 641, continuous stable fibers were also formed with decreasing diameter while increasing flow rate ratio up to 100, Fig.5.5. However, experimental fibers diameter values did not follow the theoretical predictions (black dotted line). Indeed they were smaller than expected. The decrease of the fiber as a function of the flow rates ratio, was sharper than predicted in the range of low ratios. Fibre size was not solely governed by hydrodynamics, physico-chemical factors appeared to be involved, implying in this case a shrinkage of the fiber.

The influence of the molar ratio and subsequent storage conditions was therefore investigated to understand their role on the process of fiber fabrication.

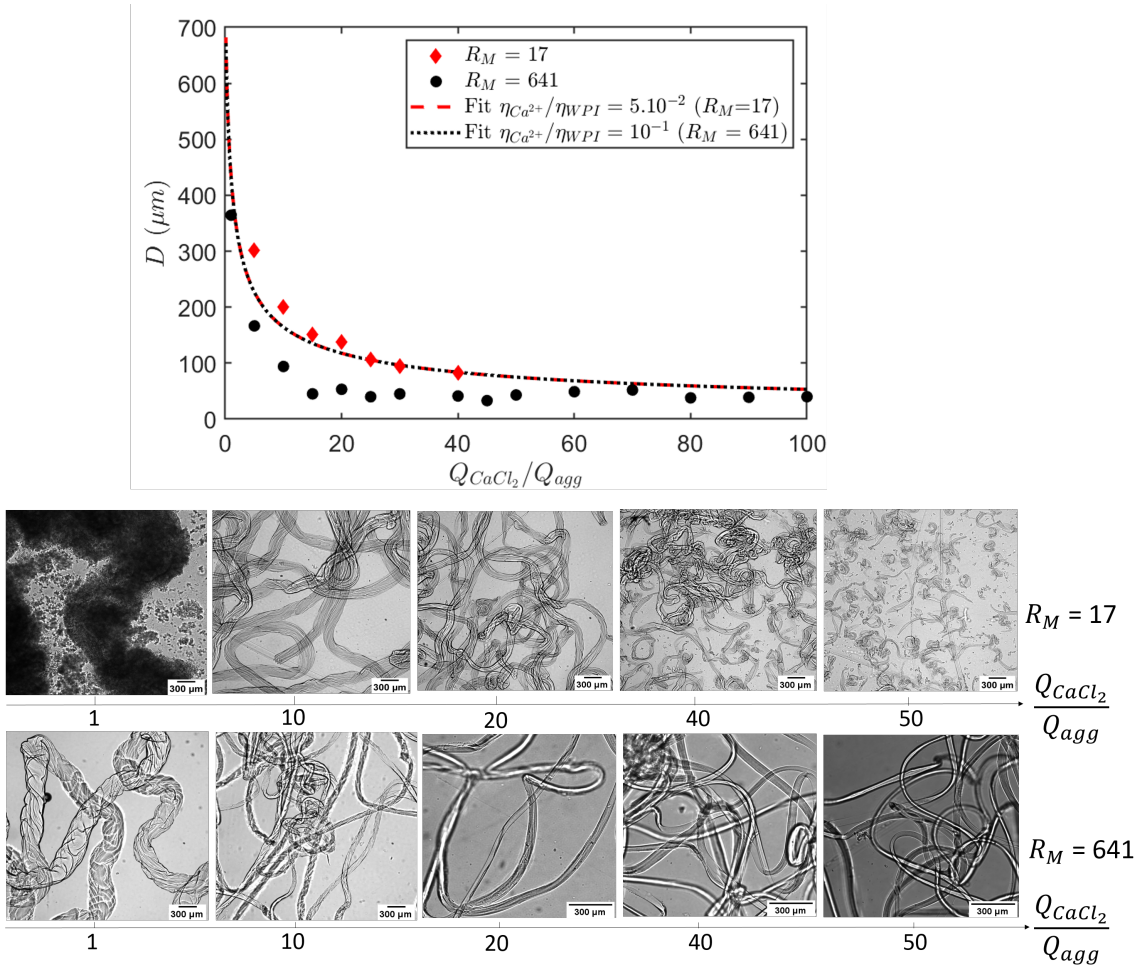

Figure 5.5: Top: Diameter of the fibers as a function of the ratio of the outer and inner flow rates for two molar ratio R_M (= 17 and 641). Dotted lines show the hydrodynamic prediction given by Eq. 5.10. Bottom: Bright field microscopic images of the fibers for both conditions. $[WPI]$ = 8% w/w, t_{global}. = 6 s and $Q_{\text{total}} = 3.3{\times}10^{-8}$ m^3/s)

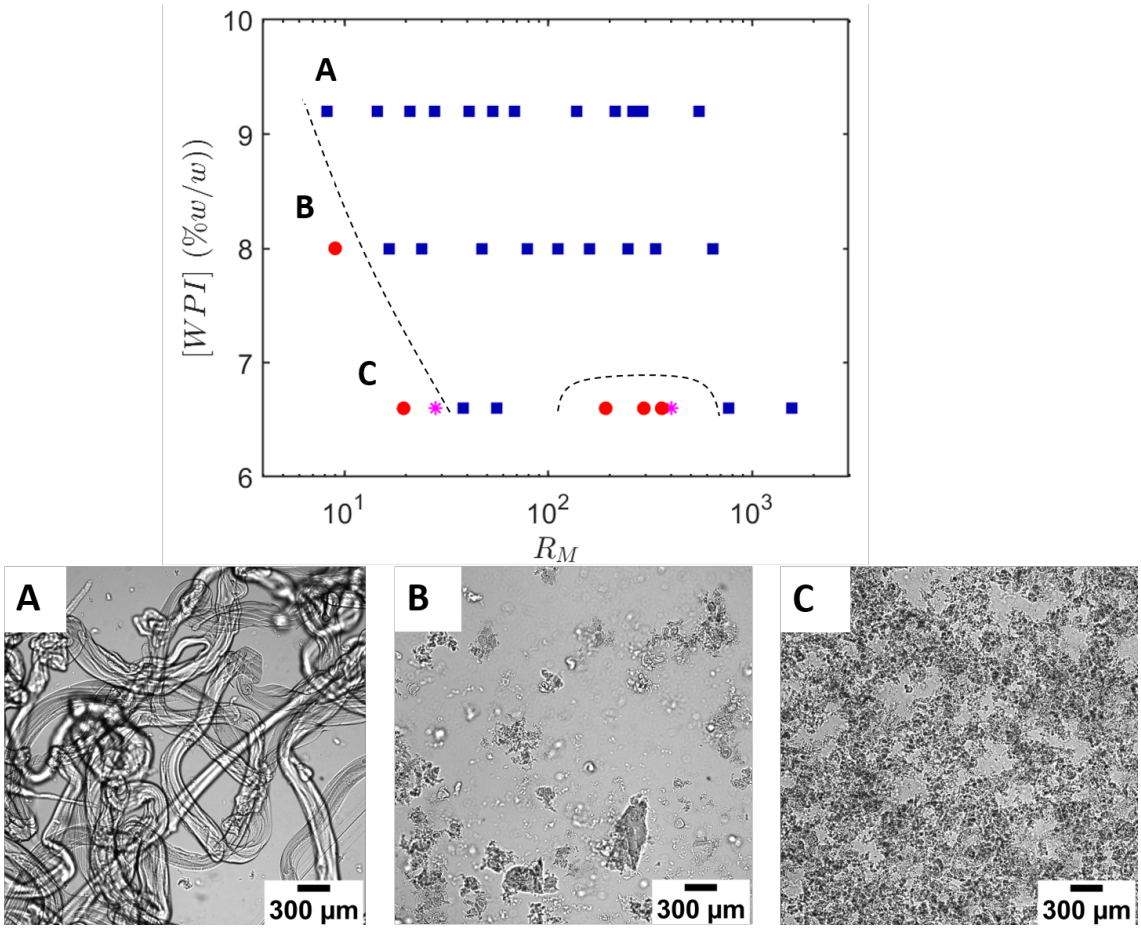

Figure 5.6: State diagram of fibres formation as a function of $[WPI]$ and R_M, after 30 s of their production. Fibres were stored in the calcium solution used for their production. Blue squares: fibers (image A). Red circles: no fibers / microscopic aggregates (images B and C). Pink stars: conditions of transition where both aggregates and short fibers were produced. Dotted lines are a guide for the eyes. $Q_{\text{total}} = 3.3 \times 10^{-8}$ m^3/s, $Q_{\text{CaCl}_2}/Q_{\text{agg}} = 10$, $t_{\text{global}} = 6$ s.

5.3.3 Effect of calcium ions and WPI on fiber formation and stability

Physico-chemical factors, such as the molar ratio R_M and concentration of WPI, influenced the gelation rate and thereby the formation of gelled fiber under flow [61]. The concentration of WPI in the suspension of aggregates was varied by either diluting or concentrating the suspension of aggregates in order to avoid aggregates structural characteristics differences with variation of the protein concentration during heating [4]. Aggregates were first formed at 8% w/w with 10 mM of NaCl, heated during 30 min at 92°C. Three weight fractions were studied: 6.6 % w/w, 8% w/w and 9.2% w/w. The point at 9.2% was just above the sol-gel transition (Figure 5.1).

Formation

We studied the formation of fibers by varying both concentrations of $CaCl_2$ and WPI for fixed processes conditions, $Q_{\text{total}} = 3.3{\times}10^{-8}$ m^3/s, $Q_{CaCl_2}/Q_{agg} = 10$, $t_{\text{global}} =$ 6 s. After their formation, the fibers were collected and stored into a petri dish filled with the $CaCl_2$ solution used for their production. Microscopic images were taken approximately 30 s after the beginning of the storage step. The results were summed-up in a phase diagram.

When the molar ratio was below a critical value, formation of fibers was not possible (Fig. 5.6). Interestingly, the minimum molar ratio required to induce fibre formation increased as $[WPI]$ decreased. Shaping and gelation of self supporting fibers depended on both molar ratio and WPI weight ratio. The closer the WPI concentration was to the sol-gel transition. the less $CaCl_2$ was required to form the fibers. At low weight ratio of WPI ($[WPI] = 6.6$ % w/w), the stability of the fibers showed a more complex feature: fibers were not obtained for both low R_M values and intermediate R_M values (100 - 700).

Stability

For each molar ratio, fibers were collected and stored in the same $CaCl_2$ solution used to produce the fibers. As we expected that the inner of the fibre was not gelled, we. collected them in $CaCl_2$ in order to pursue the gelation process. However, we observed that the size of the fibres could evolve with time according to the conditions and even disappear. The phase diagram of Figure 5.7 sum-up the states of the fibres after 20 min of storage in the $CaCl_2$ solution. Three states were distinguished: (I) the fibers were stable, (II) the fibers swelled, (III) the fibers shrank. Image analysis was not performed beyond 20 min of storage, but we verified that stable gelled fibres did not become unstable over longer storage times. Surprisingly, the transition between these three regimes was non monotonic. For a fixed value of $[WPI]$, at low R_M fibers swelled up to stabilize. For intermediate values of R_M fibers swelled up to disappear or locally break. At high value of R_M fibers shrank. Figure 5.8 shows the evolution of the diameter as a function of R_M after 20 min of incubation in the $CaCl_2$ solution. With increasing $CaCl_2$ concentration, fibers size increased. Then, there was a large

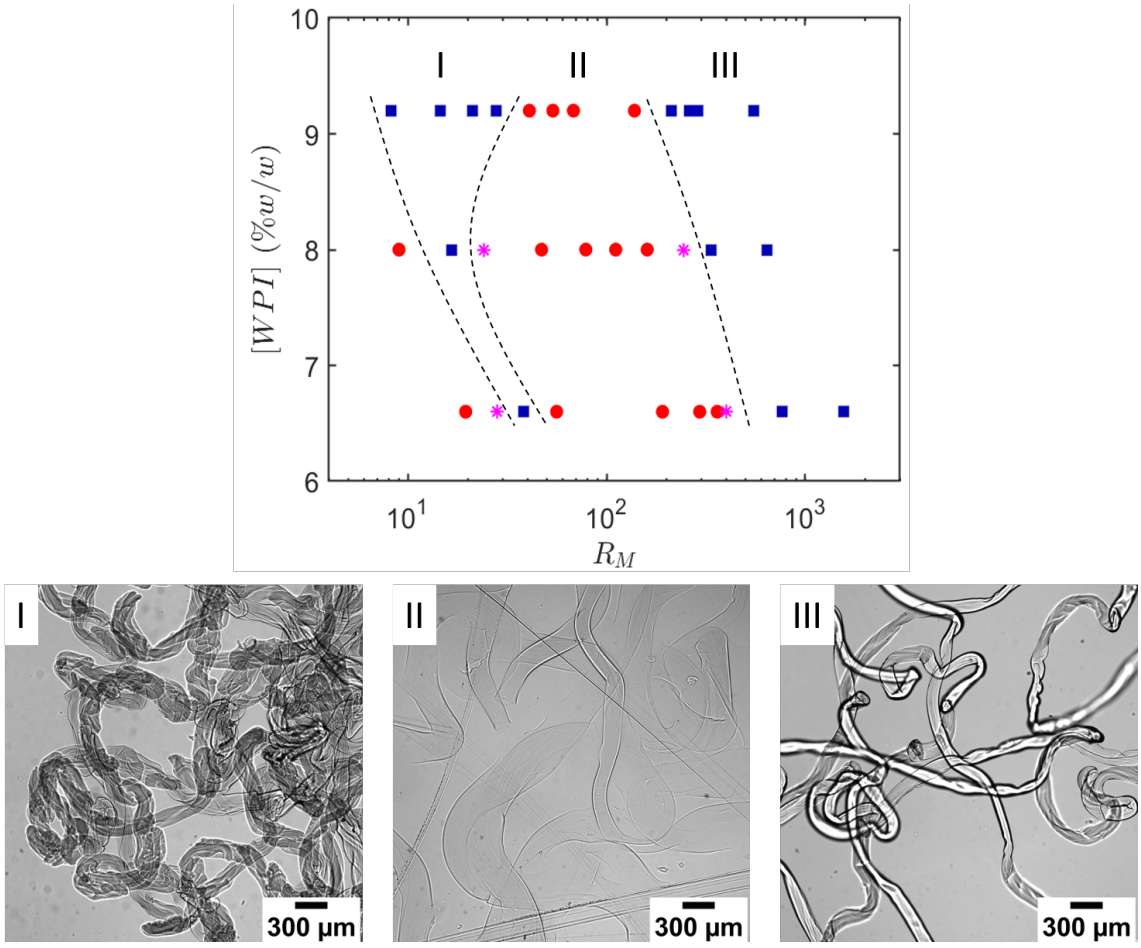

Figure 5.7: State diagram of fibres formation as a function of $[WPI]$ and R_M, after 20 min of storage in the calcium solution used for their fabrication. Blue squares: fibers. Red circles: no fibers and/or microscopic aggregates. Pink stars: transition. Three regimes of fiber evolution were identified and are illustrated by the corresponding images. I: fibers that swelled up to stabilize. II: fibers that swelled up to break-up. III: fibers that shrank. $Q_{\text{total}} = 3.3 \times 10^{-8}$ m^3/s, $Q_{\text{CaCl}_2}/Q_{\text{agg}} = 10$, $t_{\text{global}} = 6$ s.

range of intermediate values of R_M for which the fibers swelled up to disappear. At large values of R_M, the diameter of the fibers decreased.

The evolution of the fibers during the storage step was further investigated for the three regimes. First we studied the time evolution of the diameter of the fiber for $[WPI]$ of 9.2% w/w (Fig.5.9) in the regime I for which fibers were stable. A measurement error of 10% can be reasonably assumed for the fiber size estimation. Fibers formed at the lowest R_M and $CaCl_2$ concentration of storage exhibited a smaller size and did not evolve during the storage. When increasing the concentration of $CaCl_2$, fibers swelled progressively as their diameter increased up to stabilize after 600 s. Considering the uncertainty on the measurement of the diameter, it was difficult to assess if there was significant changes in fiber diameter at 30 s.

In the second regime (II), fibers were not stable over time. We observed two conditions of destruction: fibers kept swelling up to disappear or the boundaries

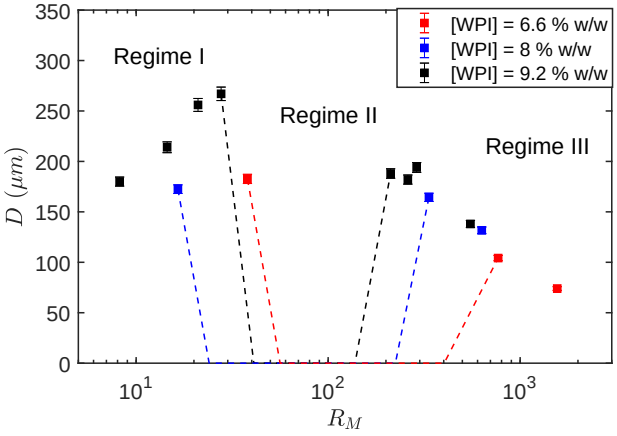

Figure 5.8: Evolution of the diameter of the fibers formed and stored in a $CaCl_2$ solution as a function of the molar ratio R_M after 20 min of storage in the calcium solution used for their fabrication. The three regimes are identified by I, II and III. In the regime II, the fibers swelled up to break-up. $Q_{\text{total}} = 3.3 \times 10^{-8}$ m^3/s, $Q_{\text{CaCl}_2}/Q_{\text{agg}} = 10$, $t_{\text{global}} = 6$ s.

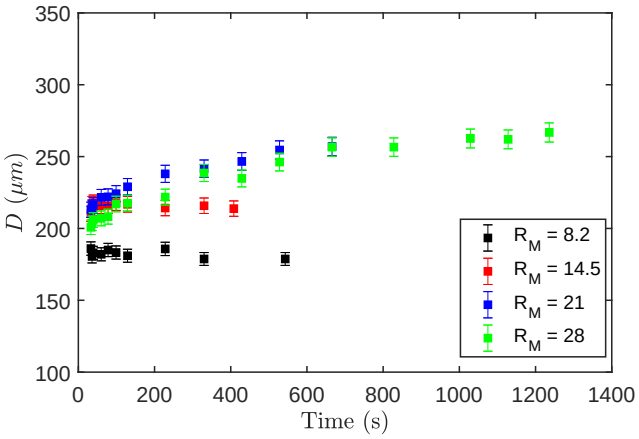

Figure 5.9: Swelling of fibers during the storage step in $CaCl_2$ solution formed at low molar ratio R_M (Regime I) with $[WPI] = 9.2\%$ w/w. The kinetics of swelling depended on R_M and stabilized in regime I. Error bars represent a measurement error of 10% of the mean value. $Q_{\text{total}} = 3.3 \times 10^{-8}$ m^3/s, $Q_{\text{CaCl}_2}/Q_{\text{agg}} = 10$, $t_{\text{global}} = 6$ s.

cracked at some spots. Figure 5.10 shows two examples of these behaviours: (a) $R_M = 47$ for $[WPI] = 8\%$ w/w, (b) $R_M = 41$ for $[WPI] = 9.2\%$ w/w). Fibers were both collected in the same $CaCl_2$ storage concentration than the one used for their production. For condition (a) fibers swelled and boundaries remained, eventually keeping the appearance of a footprint. For condition (b) the gelled membrane of the fibers burst in several locations (red arrows), in less than 10 min. It confirmed that the fibre was not gelled over its whole radius and that a shell was formed during the flow. This breakage was counter-intuitive as we could expect further gelation of the initiated core-shell structure with increasing consolidation, considering the very

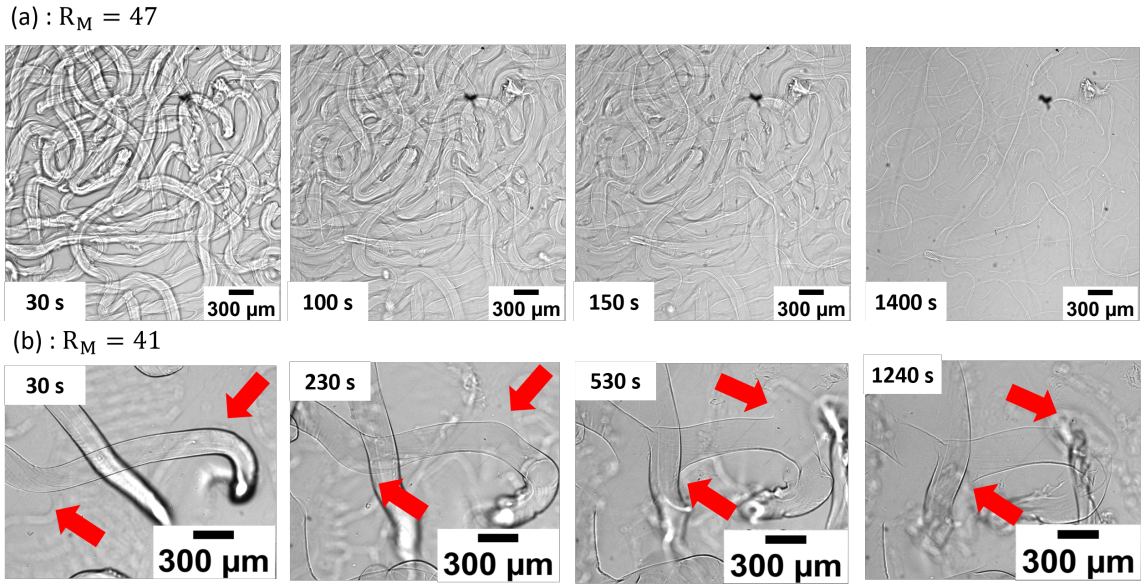

Figure 5.10: Kinetics of swelling and breakage of the fiber at intermediate molar ratio R_M (regime II) during the storage step in $CaCl_2$ solutions. a: $[WPI] = 8\%$ w/w and $R_M = 47$. The fibers swelled up to disappear. b: $[WPI] = 9.2\%$ w/w and $R_M = 41$. The shell of the fiber broke-up locally, as shown by red arrows. $Q_{\text{total}} = 3.3 \times 10^{-8}$ m^3/s, $Q_{\text{CaCl}_2}/Q_{\text{agg}} = 10$, $t_{\text{global}} = 6$ s.

short flow residence time.

The regime III, at high molar ratio R_M, was characterized by the formation of stable and continuous fibers of few cm length of radius smaller that the one predicted by the hydrodynamic equations, $D = 165$ μm for $Q_{\text{CaCl}_2}/Q_{\text{agg}} = 10$ (Figure 5.5). The shrinkage mechanism took place presumably during flow (6 s) and/or the time lag between their production and the images recording (30 s) as no evolution of their size was recorded during storage.

To sum-up these observations, the formation of fibers in flow depended as well on the hydrodynamic conditions as the physico-chemical conditions. The closer the conditions were to the sol-gel transition, the easier was the production of fibres. However, their stability depended also on the concentration of $CaCl_2$ used during their formation and the storage step in a non monotonic way. The fibers i) swells up to stabilize at low calcium concentration, ii) swells up to break for intermediate concentration, iii) shrinks at high concentration (Figure 5.9). These observations and the characteristic times of gelation [61] suggested strongly that the fibre had a core-shell structure, which was magnified by the observation of the break-up of the shells for given parameters. The alternation of these states with increasing calcium concentration for a given protein concentration suggested complex balance between different mechanisms. At this stage, we could only speculate about different scenarios. Shrinkage of fibers at high R_M values could result from the difference of chemical potentials between the liquid core of the fibre and the solution of $CaCl_2$ which induced a flux of water, from the core of the fibre to the high concentrated solution of calcium. However, in analogy to water exchanges in U tube containing

a semi-permeable membrane, such osmotic flux should imply that the shell of the fibre should have the role of a semi-permeable membrane to calcium ions. However, this mechanism could not explain the swelling of the fibers at lower calcium concentration: the swelling should increase when the concentration of calcium decreased. Conversely, we observed a maximum of swelling at intermediate values of calcium concentration. So the balance between the chemicals potentials of the calcium solution and the non-gelled suspension of aggregates cannot explain by itself our observations.

Alternatively, we could invoke a modification attractive to repulsive forces between aggregated within the fiber, leading to the diffusion of aggregates. In fact, the time ($\sim$ 100 s) and length ($\sim$ 10 μm) scales over which the fibers swelled is coherent with a diffusive mechanism of the aggregates ($\sim 10^{-12}$ m^2/s, $\sqrt{10^{-12} \times 100} = 10$ μm). During the gelation process several types of covalent and non-covalent bonds are involved within the aggregates: electrostatic interactions, Van der Waals forces, hydrogen bonds, hydrophobic interactions, overlapping interactions, disulphide bonds. The formation and the stabilisation of these bonds rely on different mechanisms and physico-chemical conditions. Considering the very short gelation time under flow, we expected that the inner aggregate suspension was not fully gelled. Moreover, by increasing the concentration of calcium during the flow and in the storage step, we expected an increase of the gelation rate and so a better stability of the fiber.

5.3.4 Effect of salts and pH on fiber stability during storage

We varied the conditions of the storage step to gain a deeper insight into the swelling and dissolution mechanism. We varied the concentration, the type of salts and the pH of the storage solution. To neglect the remaining free calcium and chlorure ions from the flow, a few drops of the flowing solution containing the fibers were collected in a large volume of storage solution (50 mL). We considered that the fibers were manipulable when we were able to pick them from the storage solution with a micropipette tip. This test allowed us to qualitatively evaluate the mechanical properties of the fibers.

Effect of $CaCl_2$ concentration

We varied the concentration of $CaCl_2$ independently of the molar ratio used to form the fibers. It also permitted us to dissociate the flow to the storage step effect on the fiber structure. As the molar ratio during the flow step influenced the gelation rate and bonds strength, we studied the effect of the $CaCl_2$ storage concentration for two conditions under flow: $R_M = 17$ and 535 for $[WPI] = 8\%$ w/w.

We observed that the fibers size remained constant within the storage when fibers were stored in 0.03 M $CaCl_2$ with $D = 187 \pm 7$ μm for $R_M = 47$ and $D = 264 \pm 9$ μm for $R_M = 535$ (Figure 5.11). A qualitative decrease of the pixels intensity was observed, hypothetically linked to a structuring of the fiber within the observation time.

When the $CaCl_2$ storage concentration increased ($[CaCl_2] = 0.2$ and 0.72 M), we observed for both flow molar ratio swelling, and fibers dissolution only for $R_M =$

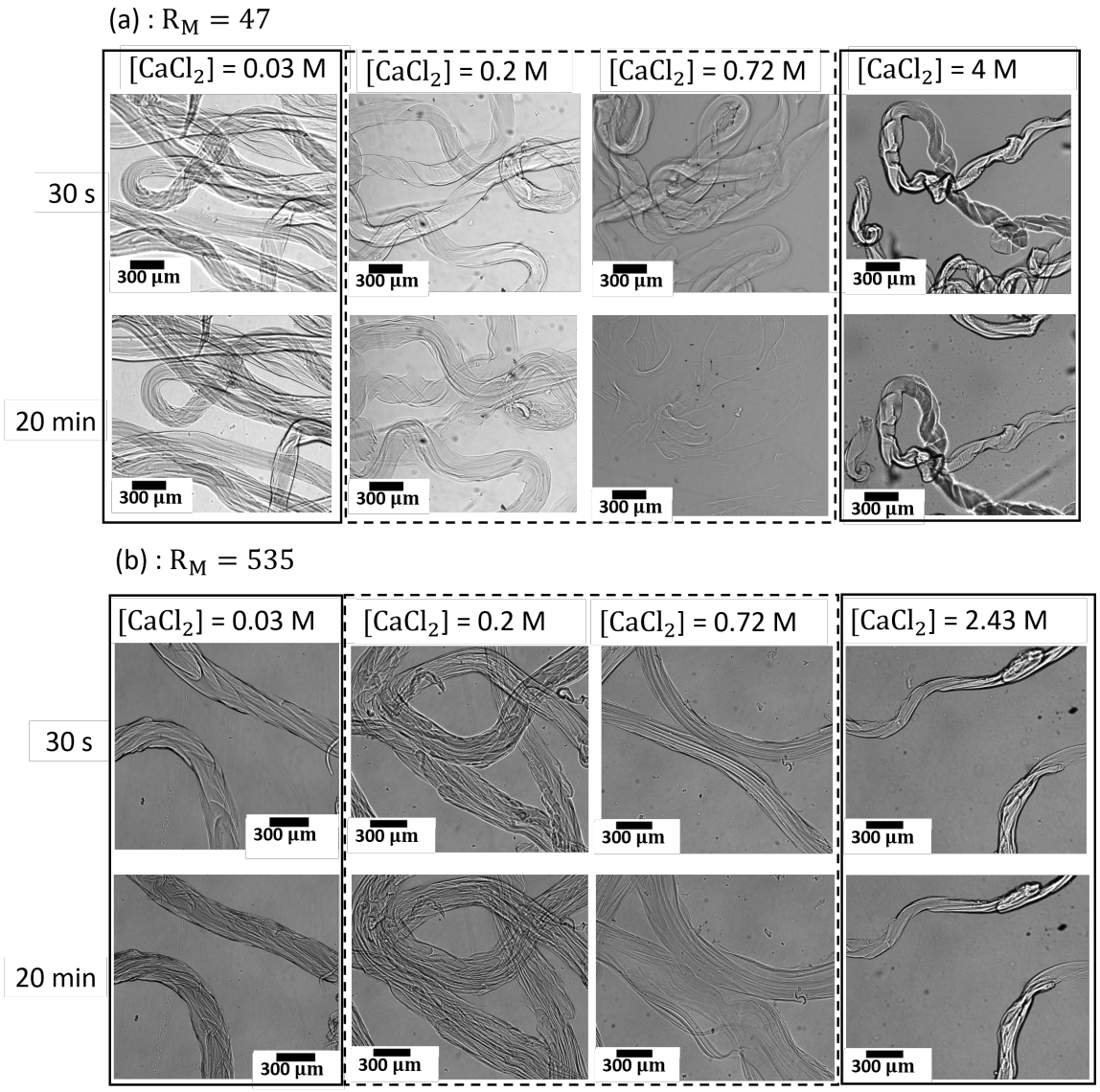

Figure 5.11: Effect of increasing $CaCl_2$ storage concentration on stability of the fiber structure during the storage step. a: $R_M = 47$, $[WPI] = 8\%$ w/w and $[CaCl_2] = 0.2$ M. b: $R_M = 535$, [WPI] = 8% w/w and $[CaCl_2] = 2.4$ M. Plain boxes indicate conditions for which fibers could be manipulated using a micropipette. Dotted boxes indicate conditions for which fibers swelled, dissolved or were not manipulable. $Q_{\text{total}} = 3.3 \times 10^{-8}$ m^3/s, $Q_{CaCl_2}/Q_{\text{agg}} = 10$, $t_{\text{global}} = 6$ s.

47 as described in the previous section. The $CaCl_2$ storage solution was therefore driving the destabilization mechanism. Even when fibers were formed at high molar ratio during the flow, the subsequent storage step destabilized their structure for intermediate ranges of $CaCl_2$ concentration. However, the gelation rate and resulting fiber structure after flow seemed to affect the dissolution rate and/or mechanism in the storage step: fibers produced at $R_M = 47$ and stored in of 0.72 M $CaCl_2$ solution swelled up to dissolution, whereas fibers produced $R_M = 535$ swelled up to stabilize for the same $CaCl_2$ solution. Finally, when the $CaCl_2$ storage concentration was further increased, shrinkage of the fiber was observed for both flow molar ratio ($R_M = 47$ $D = 145\pm6$ μm and $R_M = 535$ $D = 148\pm8$ μm). We concluded that calcium ions had different distinct roles which could be uncoupled. The first one was related to the formation of the fiber under the flow as it permitted to pass the sol-gel transition (Figure 5.6). The second one led to the shrinkage of the fiber. This phenomena could be simply explained by osmotic phenomena. The third one was the most surprising and was related to the swelling of the fibers. At this stage, only speculative explications based on the interaction mechanisms of calcium ions towards negatively charged surfaces could be put forward. The dissolution mechanism could be seen as the result of increased repulsive interactions between negatively charged surfaces of the aggregates. One should take into account the first reaction that occurred under flow between calcium ions and aggregates. Instead of an increase in attractive interactions, the opposite phenomenon occurred, under the assumption of electrostatic interactions. A charge inversion could therefore have occurred during subsequent storage step in intermediate $CaCl_2$ concentrations.

Storage in demineralized water

The fibers were stored in a demineralized water solution ($\sigma = 0.5$-0.9 μS/cm, pH=5.5-6.5, Figure 5.12). Fibers formed under flow at three selected molar ratios $R_M = 47$, 535, 641, were subsequently stored in demineralized water solution and studied over time. We observed swelling and breakage of the fibers. However, at 20 min of storage the fiber structure was different depending on the physico-chemical flow conditions. Fibers formed at the lowest molar ratio under flow exhibited swelling up to stabilize, whereas when increasing R_M fibers exhibited first swelling and rupture, then only rupture. In these two last cases ($R_M = 535$ and 641), aggregates were identified at the outside of the fiber, meaning that these aggregates have been released from the fiber due to the break-up of its shell. These observations were coherent with simple osmotic phenomena based on the difference of chemical potentials between the inner of the fiber and the outer solution which increased when R_M increased.

Effect of NaCl concentration

In order to understand if the role of the calcium was or not specific to this kind of divalent salt, we used NaCl solution to store the fibers. Note that NaCl is also involved in cold-set gelation of WPI aggregates, but the gelation kinetics is slower. Then, we changed the kind of salt by using a monovalent salt NaCl, we did not observe significant swelling from 5 mM to 0.3 M NaCl. At 1 M NaCl, fibers swelled

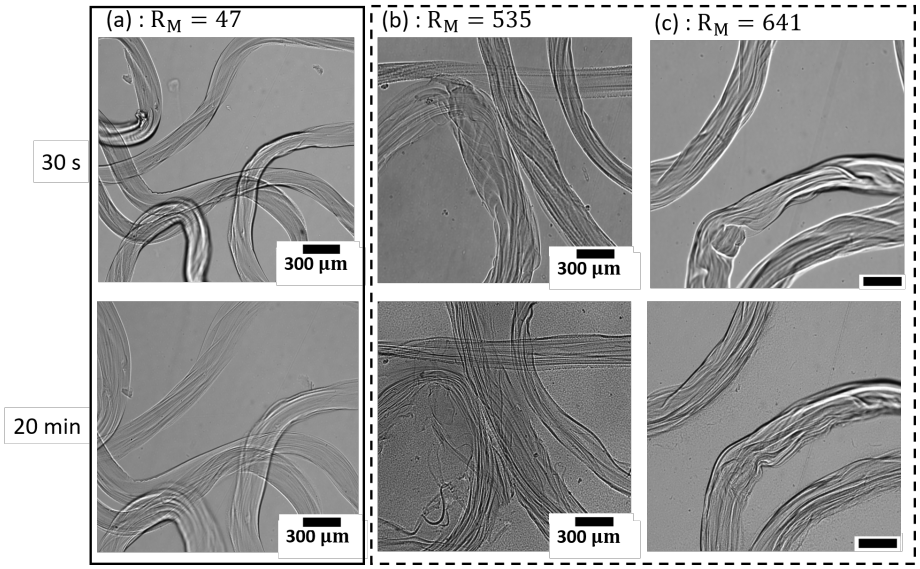

Figure 5.12: Swelling and rupture of fibers during their storage in demineralized water storage solution (σ = 0.5-0.9 μS/cm, pH=5.5-6.5). Fibers were formed for three selected molar ratios. (a) $R_M = 47$, (b) $R_M = 535$ and (c) $R_M = 640$. After 20 min of storage, the fibers swelled and aggregates were visible in the water closed to the fibers. Plain boxes indicate conditions for which fibers could be manipulated with a micropipette. Dotted boxes indicate conditions for which fibers swelled, dissolved or were not manipulable. Scales bars : 300 μm $[WPI] = 8\%$ w/w, $Q_{\text{total}} = 3.3 \times 10^{-8}$ m^3/s, $Q_{\text{CaCl}_2}/Q_{\text{agg}} = 10$, $t_{\text{global}} = 6$ s.

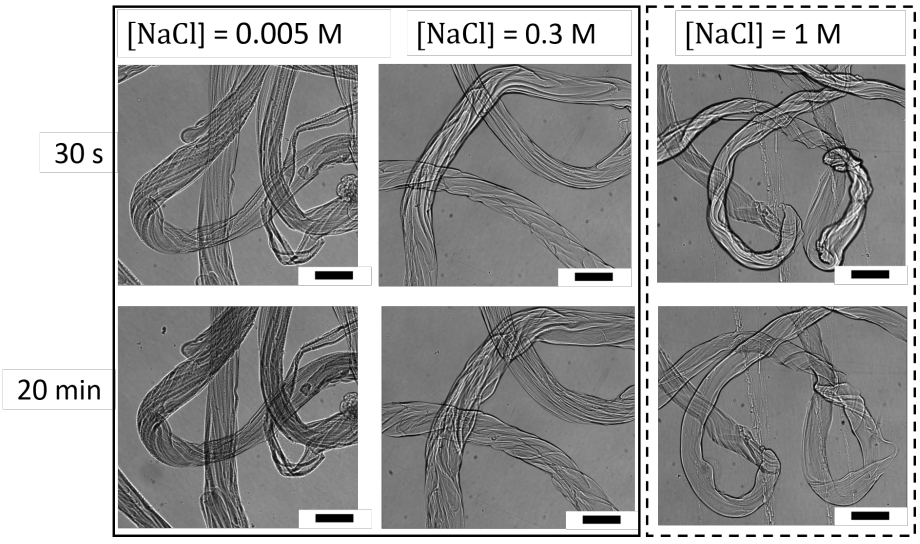

Figure 5.13: Stability of the fibers in NaCl solutions. Green dotted boxes indicate conditions for which fibers could be manipulated with a micropipette. Plain boxes indicate conditions for which fibers were manipulable. Dotted boxes indicate conditions for which fibers swelled, dissolved or were not manipulable. $[WPI] = 8\%$ w/w, $R_M = 535$, $Q_{\text{total}} = 3.3 \times 10^{-8}$ m^3/s, $Q_{\text{CaCl}_2}/Q_{\text{agg}} = 10$, $t_{\text{global}} = 6$ s.

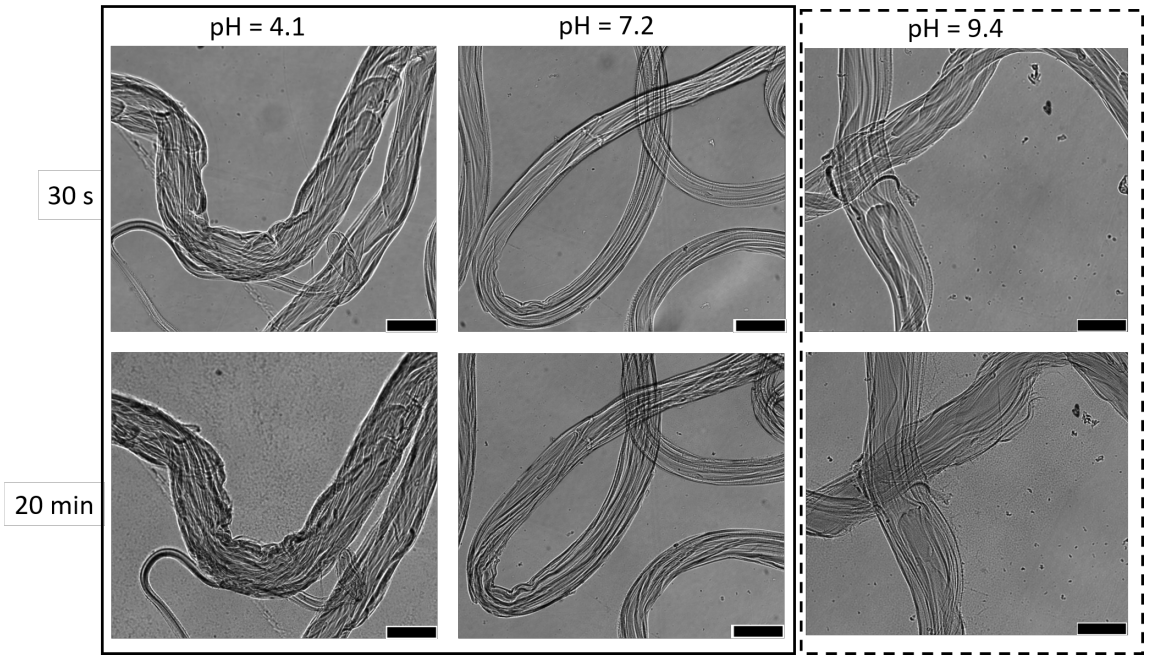

Figure 5.14: Stability of the fibers under acidic, neutral and alkalin storage solution. Fibers swelled up to stabilize at pH = 7.2, broke at pH = 4.1 and swelled up to break-up at pH = 9. Aggregates were also visible in the water near the fibers for pH 4.1 and 9 after 20 min of storage. Plain boxes indicate conditions for which fibers could be manipulated with a micropipette. Dotted boxes indicate conditions for which fibers swelled, dissolved or were not manipulable. Scale bars: 300 μm. $[WPI] = 8\%$ w/w, $R_M = 535$, $Q_{\text{total}} = 3.3 \times 10^{-8}$ m^3/s, $Q_{\text{CaCl}_2}/Q_{\text{agg}} = 10$, $t_{\text{global}} = 6$ s.

and were not manipulable (i.e. takeable from the storage solution with a micropipette tipe), as for intermediate concentrations of $CaCl_2$ (Figure 5.11). This result was not due to the difference of osmotic pressure between the core of the fibre and the NaCl solution, because in this case the fibers should swell when the concentration of NaCl decrease.

Effect of pH

Fibers formed at $R_M = 535$ with $[WPI] = 8\%$ w/w were stored in different storage solutions with pH set at 4.1, 7.2 and 9.4 (Figure 5.14). Note that pH 4.1 was below the isolectric point of WPI (5.2). In acidic conditions, no significant swelling was observed but fiber breakage occurred as aggregates were found in the water near the fibers. At neutral pH, we observed a swelling of 30% after 20 min of storage in pH 7.2. At pH 9.4, fibers swelled to up to break up and some aggregates were released in the solution.

Again, these observations could not be explained by osmotic phenomena, as the swelling should be maximum at neutral pH. Conversely, the swelling was maximum at acidic and basic pH. All of these results suggested strongly that swelling and shrinking of fibers was not controlled solely by osmotic pressure difference between the core of

the fiber and the supernatant. However, these results were reminiscent of pH-sensitive hydrogels swelling behavior. Gunasekaran et al. (2006) [45] showed that whey protein concentrate hydrogels exhibited a pH-sensitive swelling behavior, as ionic hydrogels, the swelling being quicker at alkalin pH. Park et al. [92] studied the swelling ratio of gel made from an albumin solution. They found that the swelling ratio increased with increasing the pH of the external medium toward alkaline conditions. They showed that the pH sensitive swelling characteristics of the gels could be shifted by varying the pH of albumin solutions. Gels prepared at pH = 11.1 exhibited higher swelling rate with increasing pH medium values. They linked this behavior with the higher number of ionized carboxyl groups remaining in the gel under this pH condition. With increasing the pH above the isoelectric point of the proteins, the net negative charge of the proteins is increased due to deprotonation of acidic amino acid residues (aspartic acid: $pK_a = 3.86$, glutamic acid: $pK_a = 4.25$, cysteine: $pK_a = 8.33$, tyrosine: $pK_a = 10.07$) [16]. In alakilin conditions, proteins would be thereby negatively highly charged and repulsive forces would increased between the aggregates within the fiber. Increasing deprotonation of carboxylic groups may also result in an increase of site specific calcium binding. In acidic conditions, the net positive charge density increased with protonation of alkaline amino acid residues (histidine: $pK_a = 6.0$, lysine: $pK_a = 10.53$, arginine: $pK_a = 12.48$), [16]. Breakage of the membrane was also observed without a similar swelling behavior as observed in alkalin conditions. As the distribution of the functional ionisable groups is not symmetrical on both sides of the protein isoelectric point, exact same behavior was not expected to occur [112]. This result was found to be consistent with the pH-dependent swelling behaviour of hydrogels which show a higher swelling ratio in the alkaline than in the acidic range [16]. For Betz et al. (2012) "this is due to the polyampholytic character of the whey protein hydrogels whose swelling ratio is higher as the charge density of the network is increased". Betz et al. (2012) studied the effect of physico-chemical alterations during protein gelation on pH-dependent swelling behaviour of whey protein hydrogels. They highlighted that "the pH during gelation has a strong impact not only on the resulting network structure like density and nature of cross-links but also on the pH-dependent hydrogel charge".

To sum-up, as the protein charge density is pH-dependent, swelling and breakage could be induced by increased surface charge density. We have seen that storage under intermediate concentration of $CaCl_2$ (0.2 M < [$CaCl_2$] < 1 M) led to swelling and breakage of the fiber which was striking. The pH of the $CaCl_2$ solutions that induced swelling and breakage during storage was measured and varied between 6.2 and 5.9. Variations in the pH of $CaCl_2$ storage solutions was therefore not involved. Alternatively, swelling could be explained by the mechanism introduced by Phan-Xuan et al. [97] in which a self-stabilization effect could appear due to spontaneous increase of the pH during aggregate formation that should lead to an increase of their surface charge density. As calcium ions bind to specific sites of the protein, a decrease of the pH was recorded due to the release of protons to the solution by Kharlamova et al. [61, 62], but without significant change of the degree of protonation of the proteins. In our range of $CaCl_2$ concentration were swelling was observed (0.2 M < [$CaCl_2$] < 1 M), considering than an aggregate binds 3 Ca^{2+} all Ca^{2+} binding

sites were supposed saturated and excess of $CaCl_2$ induced excessive screening by decrease of the effective charge density according to Kharlamova et al. (2018)([61]). When fibers were collected in low $CaCl_2$ concentration, calcium ions were not in sufficient proportion to induce high repulsive forces among the aggregates. To test this last hypothesis, we stored the fibers in EDTA solution (pH 8., 0.5 M EDTA), a calcium chelatant, for R_M ranging from 17 to 160 and 8% w/w WPI. We observed that fibers were stable without swelling, which could be explained by increasing site specific calcium binding while the excess of calcium ions formed neutral complexes with EDTA. From our understanding, we propose that the Ca^{2+}-dependent swelling behaviour of the fibers is likely to be induced by variation of aggregates charge density leading to increased repulsive interactions. The mechanisms involving the Ca^{2+} and the variation of the charge density in an intermediate range remained speculative.

5.4 Conclusion

A new structuring process to form fibers from WPI fractal aggregates by a combination of micro-flows and Ca^{2+}-induced gelation was developed. The diffusion - gelation time of calcium ions towards the jet aggregates being of the same order of the residence time of the fiber in the flow, fibers had a core-shell structure. The shell was composed of gelled aggregates, whereas the core was composed of aggregates. This core-shell structure was illustrated by the rupture of the shell and the release of the inner aggregates under specific chemical conditions (pH, salts), opening the ways to use these fibers not only as texture agents but also as responsive materials for drug delivery. Moreover, the size of the fibre was not solely set by the hydrodynamic parameters. The fibers shrank under high concentration of calcium, due to osmotic water flux from the core of the fibre to the highly concentrated salt solution. The core-shell structure was also partly the result of the concentration of aggregates in the shell. Finally, the stability of these fibers under different chemical conditions resulted of a complex interplay between different phenomena which have to be further investigated: gelation kinetics, variation of the effective charge density and osmotic stresses.

- Core-shell fibers of about 100 μm diameter and few centimeters length based on WPI aggregates by Ca^{2+}-induced gelation were produced in a co-axial flow focusing device.
- The diameter of the fiber was controlled as well by the hydrodynamic as by the calcium concentration.
- The fibers were responsive to chemical stimuli (salts, pH): they could shrink or release their content by swelling, bursting or dissolution.

Chapter 6

Characterization of the diffusion-reaction mechanism of calcium ions in a suspension of WPI aggregates

Contents

6.1 Introduction

Strong evidences showed that fibers produced by a combination of hydrodynamic spinning and salt-induced gelation of concentrated suspension of WPI aggregates had a core-shell structure. Moreover, non-monotonous swelling and shrinking could lead to the stabilization or the bursting of the fibers. To shed light on the underlying phenomena, we studied in this chapter the gelation of suspension of WPI aggregates by diffusion of calcium ions in a simplified geometry. In this chapter we used a bi-dimensional geometry to visualize and gain further insights on the gelation mechanism occurring during the fiber formation under flow. The gelation of WPI aggregates resulted from the diffusion of the calcium ions towards the aggregates and subsequent reaction leading to the formation of a gel network. The gelation was further described in terms of a diffusion reaction mechanism. We varied the molar ratio between calcium ions and WPI aggregates and studied the evolution of a diffusion reaction front. Results reported in this chapter are presented as an opening.

6.2 Materials and methods

6.2.1 Materials

WPI aggregates

WPI aggregates were prepared as described in Chapter 5. In this study both labelled and unlabelled aggregates were used, both prepared at 8% w/w with 10 mM of NaCl at neutral pH and heated during 30 min at 92°C. 10 μm diameter fluorescent particles made of polystyrene (Thermo Scientific Fluoro-Max Dyed Green Aqueous Fluorescent Particles) were added to the suspension of unlabelled aggregates to quantify the velocity gradient during the diffusion reaction. The labelled native proteins were prepared as described in Chapter 3. Prior to aggregation, a 8% w/w WPI solution was prepared with 5% of labelled native proteins and 95% of unlabelled native proteins, with 10 mM of NaCl and the pH was adjusted to 7.

Preparation of calcium ions solutions

$CaCl_2$ solutions were prepared as described in Chapter 5. $CaCl_2$ concentrations varied from 4 M to 207 mM and R_M varied from 882 to 47.

6.2.2 Experimental device

Two experimental devices were used. First, we set up a chamber in which we brought the aggregates and the calcium ions into contact (Figure 6.1). This chamber was made by adhering a gene frame to a glass slide. A second glass slide was placed perpendicular to the first one, leaving one extremity of the gene frame open to fill the chamber with the aggregates suspension. The thickness of the chamber, equal to the thickness of the gene frame, was 250 μm. The aggregates suspension was injected slowly into the chamber (B) to prevent bubble entrapment, until it reached

the other extremity (A). A few drops were deposited at the entrance B so to form a reservoir of aggregates. The extremity A was left open to deposit a drop of $CaCl_2$, so to bring into contact calcium ions with aggregates. This step was critical, as the manner of depositing the drop could either result in a homogeneous plane front or a tree structure. Image recording was started before the $CaCl_2$ drop deposit. In this configuration we could not change the thickness of the chamber, as the thickness of the gene frame was fixed. The greater the height of the chamber, the greater the error in determining the position of the front especially at short times.

To overcome these problems, we used a glass capillary with a thickness of 100 μm. We used this geometry for the time evolution of the diffusion-reaction front with labelled aggregates. The capillary was filled by capillarity with the aggregate suspension. It was deposited on a glass slide. Then a drop of $CaCl_2$ was deposited at the entrance. The manner of depositing the drop was critical in this configuration as well.

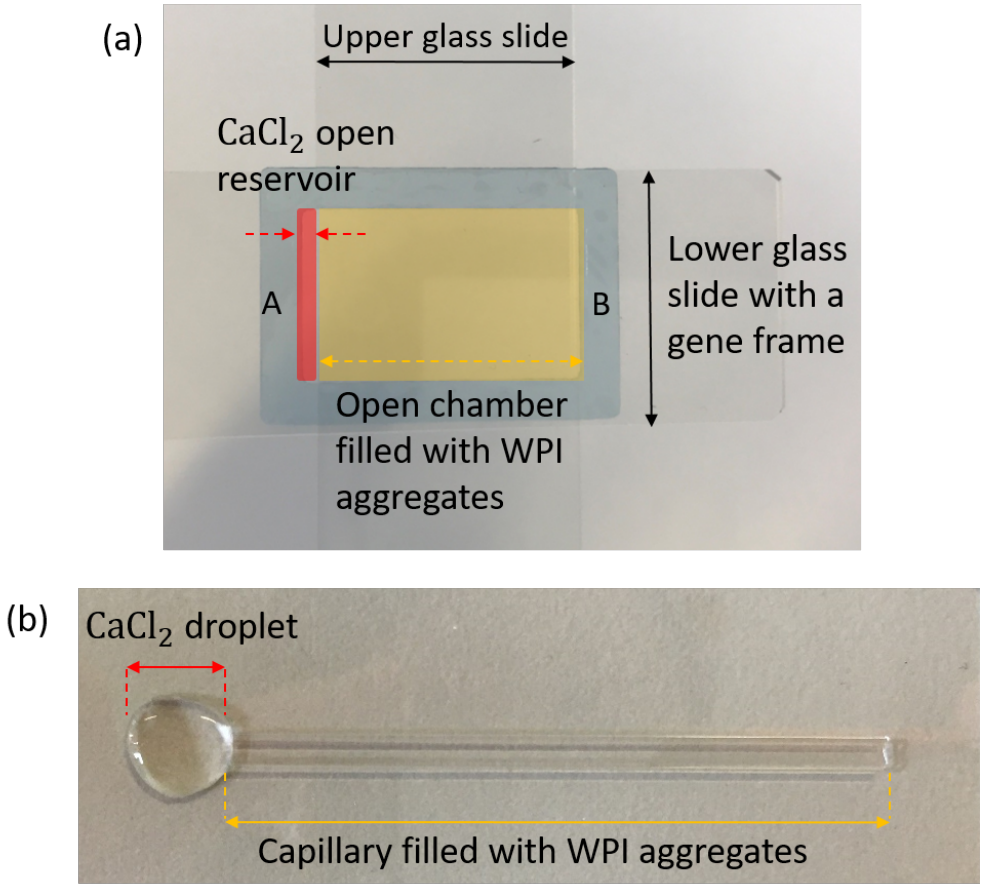

Figure 6.1: Bi-dimensional geometries used to bring into contact calcium ions with WPI aggregates. (a) : The chamber was first filled with the suspension of aggregates from the right, to reach the extremity of the perpendicular glass slide. Then a drop of $CaCl_2$ was deposited at the left, constituting an open reservoir of calcium. (b) : A glass capillary was filled by capillarity with the aggregate suspension. It was deposited on a glass slide. Then a drop of $CaCl_2$ was deposited at the entrance resulting in the formation of either a plane front or a tree structure. Evolution of the plane front was recorded over time.

6.2.3 Images recording

Image recording was carried out using a Hamamatsu ORCAFLASH high sensitivity camera (12 bits) and an Olympus IX 73 microscope. When labelled aggregates were used, a shutter was used to capture the image for the duration of the exposure time (100 ms). Image recording was started before the deposit of the $CaCl_2$ droplet and the frame rate was varied.

6.2.4 Image analysis

The analysis of the images was based on a difference in the grey level intensity of the pixels during the diffusion reaction of calcium ions in the aggregate suspension (Figure 6.2). Each image of the sequence was normalized by the first image before the addition of the $CaCl_2$ droplet. A time-space image was generated with the time on the y-axis and the distance on the x-axis. Each image of the sequence corresponded to a time and was converted into a time value depending on the fps value used. In each image we averaged a dozen of lines. Each horizontal line (y-axis) of the time-space image corresponded therefore to the average value of a dozen of lines of the corresponding image (Figure 6.3). The position of the front was defined as the intensity transition zone and was determined manually, with an uncertainty of about 10μm. The estimation of the front position was therefore rather accurate but caution should be taken for the early times of the diffusion reaction process.

Let us mention that definition of the position of the front as the intensity transition zone is purely pragmatic and the physical reason leading to a sudden change in the light intensity remains unclear.

Labelled aggregates were also used without fluorescent particles. All the images were normalized by an image without $CaCl_2$. The intensity of the aggregates in the initial state was therefore equal to 1. We therefore followed, as a function of time and space parameters, the evolution of the normalized intensity, related to the aggregate concentration.

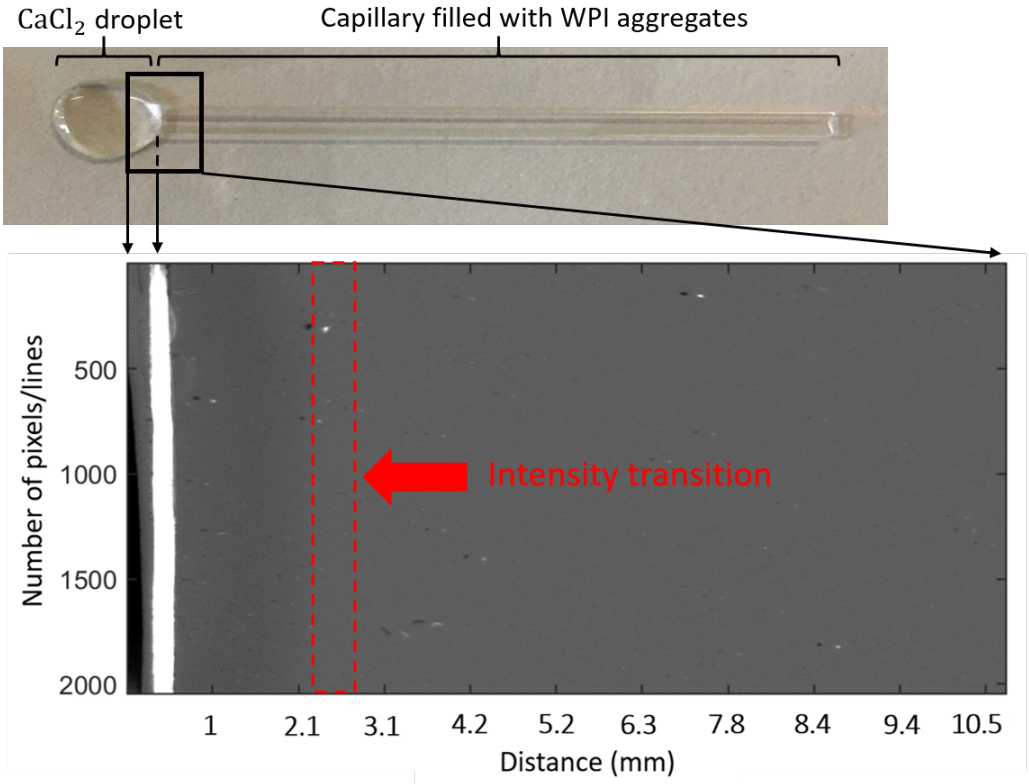

Figure 6.2: Difference in the grayscale intensity of the pixels during the diffusion reaction of calcium ions in the aggregate suspension. The position of the intensity transition is determined at each time. This image corresponds to Time = 900 s of the image sequence. [WPI] = 8% w/w, $R_M = 47$, [$CaCl_2$] = 207 mM.

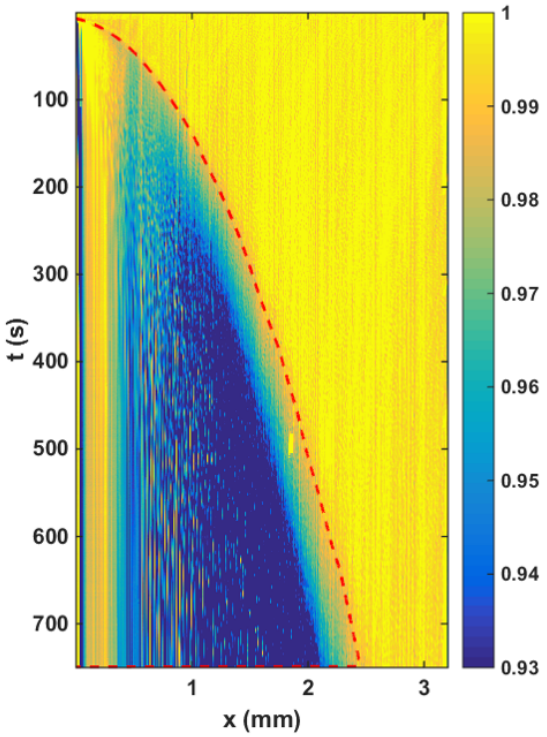

Figure 6.3: Spatio-temporal image of the grayscale intensity, after normalization by the initial image and averaging along the transverse direction. From this spatio-temporal image, we determine by hand the location of the head of the front as the first point where the intensity suddenly changed (red dashed line). In this example, [WPI] = 8% w/w, $R_M = 882$, [$CaCl_2$] = 4 M.

6.2.5 Modelling of the front advancement

We modelled the advancement of the front of gel thanks to the reaction-diffusion equations. We note C the concentration of Ca^{2+} and P the concentration of WPI. For a second order reaction between Ca^{2+} and WPI aggregates

$$P + n\mathrm{Ca}^{2+} \rightarrow G \tag{6.1}$$

where G is the gel, k the constant of reaction and n the stoichiometry of the reaction, the rate of reaction v is given by

$$v = -\frac{\partial P}{\partial t} = -\frac{1}{n}\frac{\partial C}{\partial t} = \frac{\partial G}{\partial t} = kPC \tag{6.2}$$

Coupling this equation with the diffusion equations in one dimension for both species leads to a set of coupled differential equations

$$\frac{\partial C}{\partial t} + D_{\mathrm{Ca}^{2+}}\frac{\partial^2 C}{\partial x^2} = -nkCP \tag{6.3}$$

$$\frac{\partial P}{\partial t} + D_{\text{agg}} \frac{\partial^2 P}{\partial x^2} = -kCP \tag{6.4}$$

where D_{agg} and $D_{\text{Ca}^{2+}}$ are the diffusion coefficients of the aggregates and Ca^{2+} respectively. To simplify this set of equations, we assumed that $D_{\text{Ca}^{2+}} >> D_{\text{agg}}$ and that the calcium was in large excess compared to the proteins

$$\frac{\partial C}{\partial t} + D_{\text{Ca}^{2+}} \frac{\partial^2 C}{\partial x^2} = 0 \tag{6.5}$$

$$\frac{\partial P}{\partial t} = -kCP \tag{6.6}$$

The initial conditions are $C(x = 0, t = 0) = C_0$ and $C(x > 0, t = 0) = P_0$. For the boundary conditions, we assumed that the concentration of calcium ions is fixed at $x = 0$, $C(x = 0, t > 0) = C_0$ and the concentration of protein is constant far from the front $C(x \to +\infty, t > 0) = P_0$. This set of equations was solved by the Matlab solver for initial-boundary value problems for parabolic-elliptic equations (Mathworks). As a preliminary step, we checked that the simplification of the set of equations was correct by comparing the kinetics of front advancement obtained with the full set of equations in the limit of $C_0 >> P_0$ and $D_{\text{Ca}^{2+}} >> D_{\text{agg}}$ with the results simplified set of equations.

6.3 Results and discussion

6.3.1 Evolution of the diffusion reaction front

The evolution of the front was measured for three selected molar ratios between $CaCl_2$ and WPI: 47, 111 and 640 (Figure 6.4). The detection of the front before 10 seconds was difficult due to the limits of imaging resolution at short time scales and the front determination method. Moreover, we have to be cautious about the interpretation of this change of light intensity that we interpreted as a signature of the sol-gel transition. Other interpretations could be possible. As expected, the kinetics of front propagation was quicker when R_M increased. At long times scales, we found a power law with an exponent 0.5, characteristic of diffusion law. At short time scales, the front increased abruptly, which was a signature of a kinetics limited by the reaction.

Then, we fitted the reaction-diffusion equations in the limit of negligible diffusion of aggregates and calcium ions in excess compared to the protein. There was so only two fitting parameters k and $D_{\text{Ca}^{2+}}$ which were fixed to the same values for the three experiments. Moreover, we had to define arbitrarily the position of the front x_f as the location where $P(x = x_f, t) = P_0/\alpha$ with α being a constant. Note that the fitted value of k was strongly dependent on the value of α, but $D_{\text{Ca}^{2+}}$ was independent of this choice. By default, we fixed α to 2. For large time scales, in the regime where the front advancement was limited by diffusion, the threes sets of experiments were well-fitted by the model. The apparent diffusion coefficient of Ca^{2+} was $0.7\times10^{-9}\text{m}^2/\text{s}$.

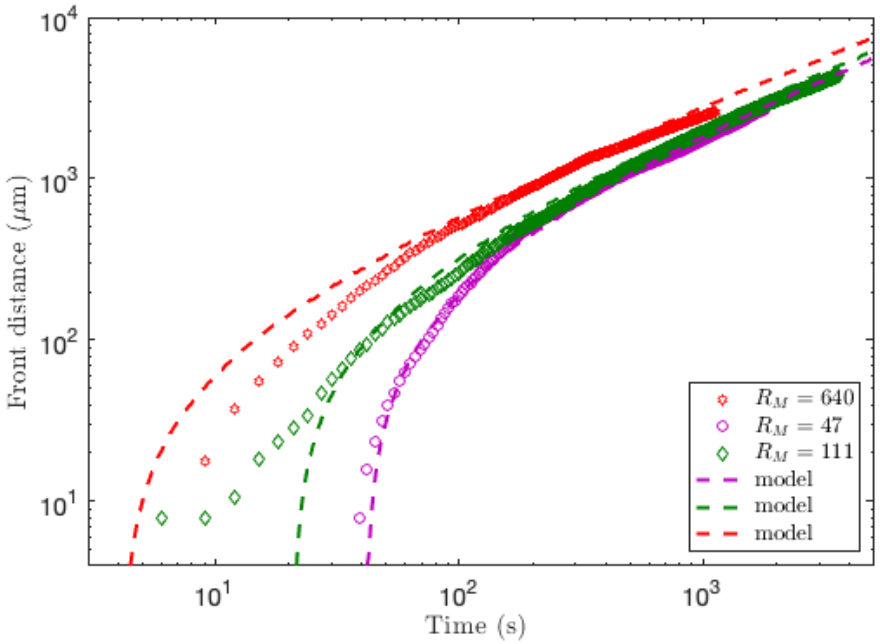

Figure 6.4: Evolution of the front of the gel as a function of the time for three molar ratios R_M. Dashed lines are the best fit of the model for $D_{Ca^{2+}} = 0.7\times10^{-9}$m^2/s, $k = 0.5\ \times10^{-3}$ L/g/s for each R_M.

This value was lower than the diffusion coefficient of Ca^{2+} in water at 25° which is 1.16×10^{-9}m^2/s [91]. Oztop et al. [91] measured also the transport of Ca^{2+} in WPI gels by magnetic resonance imaging and nuclear magnetic resonance relaxometry. They obtained an apparent diffusion coefficient of 0.9×10^{-10}m^2/s by fitting a Fickian law on their experimental data. This value is almost one order of magnitude lower than the value that we measured by fitting the reaction-diffusion model to our data. At low time scale, in the regime where the front advancement was limited by the reaction, the fit was good for the lowest molar ratios. For larger molar ratio, the model was coherent with the experimental data as the measurement uncertainties were large in this regime. To sum-up, the front propagation of the gel was coherent with a simple diffusion-reaction model for molar ratio ranging from 47 to 640 with constant values of k and $D_{Ca^{2+}}$ for the three cases.

Despite this rather good agreement with a simple diffusion-reaction mechanism, let us mention that we believe that this model remains oversimplified for many reasons. First, the gelation cannot be described as a simple reaction, as it has been shown that the mechanical properties of such a gel increases over time during several decades [61]. Second, the concentration range studied is far from dilute conditions, and the calcium diffusion coefficient might be concentration dependent. Third, at high calcium concentration, we will see in the following section that an advective term should be added, since there exists a mean flow in the cell.

These results can also be discussed in regards to formation of fibres. Even if the nature of the intensity transition was subject to interpretation, these results shed light

on the kinetics of fiber formation under flow. Let us recall that the hydrodynamic spinning of the protein aggregates reported in the previous chapter took place in a few seconds, and that the fibers are then consolidated in a storage reservoir. The diameter of the fibers is of the order of 100 μm. According to Figure 6.4, for these space and time window, the fiber formation was generally speaking in the transition zone between reaction limited and diffusion limited regimes. More precisely, for the lowest calcium chloride concentrations tested, fiber formation mostly occurred in the reaction limited regime. Gelation was therefore delayed and an important consequence is that it should be homogeneous inside the fiber. On the contrary, for the highest calcium chloride concentration, reaction was fast and gelation was limited by diffusion. These orders of magnitude are consistent with the picture of the formation of core-shell fibers at high calcium concentration, in which aggregates were not fully gelled in the core of the fibre.

6.3.2 Evidence of a mean flow at high $CaCl_2$ concentration

By adding 10 μm diameter fluorescent particles to the suspension of unlabelled aggregates, we realized that for high calcium concentration, a net flow could be observed in the cell, directed towards the calcium reservoir. It is qualitatively evidenced in Figure 6.5. The displacement of the tracers were non uniform, due to the fact they are probably located at different heights in the cell. However, there were no significant gradient of this displacement, except inside the gelled part close to the calcium reservoir, where it was significantly smaller.

In order to characterize quantitatively this flow as function of space and time, tracer position were tracked and their displacement averaged in time and space windows that are typically a tens of images and about twenty micrometers in the direction of the front displacement. Despite averaging in the transverse direction, the number of particles used remained too small to obtain a good averaging. Thus, fluctuations coming from the heterogeneous height of the tracer particles could not be avoided in some cases. This point should deserve special attention in future work.

The results are displayed in Figure 6.6 for the highest calcium concentration tested and in Figure 6.7 for two lower ones. Let us first discuss the highest concentration case ($R_M = 882$). The velocity measured was of the order of 1 μm/s, and it was uniform in the liquid phase, located at the right of the diffusion-reaction front. In the gelled phased, a velocity gradient could be seen, as the velocity tended to zero close to the calcium reservoir. The velocity slowly decreased as time increased. For this experimental condition, the velocity data were precise enough to estimate a strain rate, $\dot{\epsilon} = \partial_x v_x$, and to integrate it with respect to time to compute a total deformation ϵ. The latter is displayed Figure 6.6. Putting aside fluctuations, the deformation was about zero right to the front, but reached rather important values in a layer of about one millimeter close to the calcium reservoir. In this layer, ϵ was about -0.5 after a few hundreds of seconds, meaning that this part of the gel had been squeezed by about 50 %.

At a smaller concentration ($R_M = 160$), the velocity field was more noisy but a non-zero velocity was still measurable. It was about 0.1 μm/s, as could be seen in

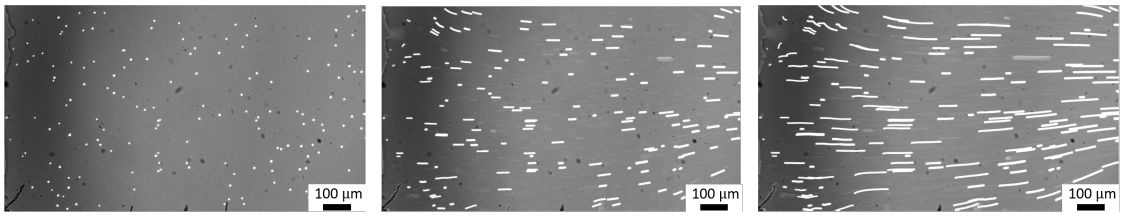

Figure 6.5: Tracer trajectories, obtained by image superposition (each pixel is the maximum intensity in the previous images), at $t = 15$s, $t = 35$s, $t = 90$s. The $CaCl_2$ reservoir is on the left.

Figure 6.7. We did not try to estimate a deformation as in the previous case, due to the poor quality of the data. When lowering the calcium concentration further ($R_M = 16$), tracer displacements were very small and their trajectories random-like. We could estimate that the mean velocity was below 10 nm/s.

Therefore the net flow reported in this section was very strongly dependant on the calcium concentration, as it increased from almost zero at $R_M = 16$ to 0.1 μm/s at $R_M = 160$ and to 1 μm/s at $R_M = 882$. It should be noticed that, due to their big size (10μm), the tracer particles were trapped in the gel. Thus, the velocity characterized in this section corresponds to the suspension velocity in the liquid like phase, where no difference between water and protein velocity is expected, but corresponds only to the aggregate velocity is the gelled phase. To ensure volume conservation, a flow of water must occur through the gel, in the direction of the calcium reservoir.

Since it is strongly dependant on calcium concentration, it is tempting to interpret the existence of this flow as a consequence of the huge osmotic pressure difference which exists between the calcium reservoir and the cell. Let us highlight that given the concentration range investigated ($[CaCl_2] = 4$M at $R_M = 882$), we are far from dilute conditions, and the phenomenon needs to be described in the framework of multi-components mixtures. Calcium chloride and water mutually diffuse into one another. However, the presence of the protein aggregates and of the gel, one would only expect only a diffusion flux, without any mean flow. One possible interpretation of the flow characterized above is to hypothesize that the gel acts as a (partly) semi-permeable membrane. In the extreme case where the gel would be impermeable to calcium or chloride ions, one would indeed expect a flow of water towards the $CaCl_2$ reservoir, exactly as in a u-tube osmotic pressure experiment. In this case indeed, water flows towards the reservoir containing salt. Given the very high ion concentrations investigated, we postulate that even a very small ion-selective properties of the gel would be required to induce the rather low water flux evidenced experimentally.

Although the above interpretation should deserve additional work, it is worth discussing the consequences of the flux of water towards the calcium chloride reservoir. This advection should carry protein aggregate towards the gelled phase, and as a result, the local concentration of protein should increase. Using the velocity gradient measured in the gel, we already reported in Figure 6.6 that the gel is significantly compressed, up to 50% at $[CaCl_2]$=4M.

In order to assess this phenomenon, we used labelled WPI aggregates to follow the evolution of the aggregate concentration during the diffusion reaction. By nor-

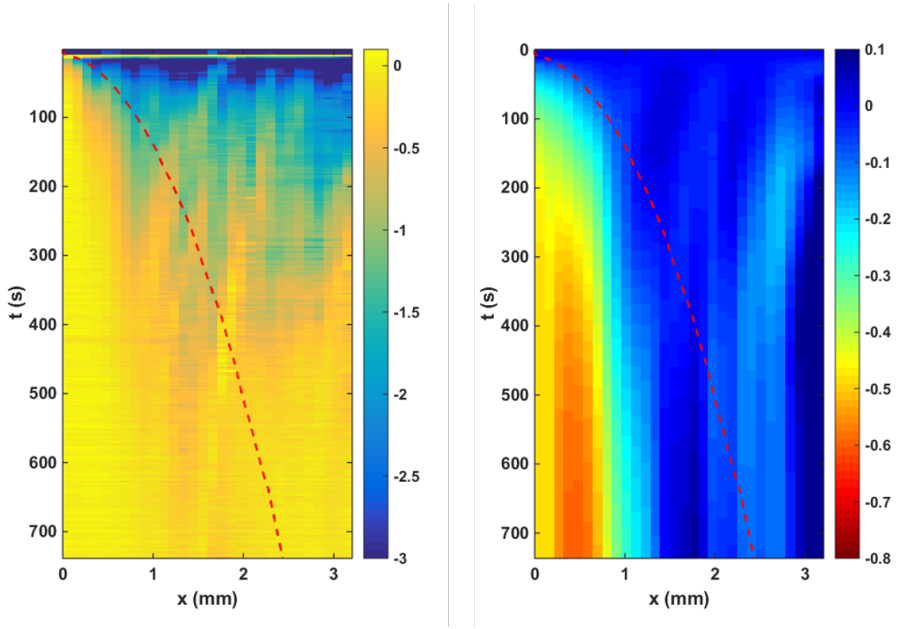

Figure 6.6: Left: spatio-temporal map of the velocity field v_x in the cell, for $R_M = 882$. The $CaCl_2$ reservoir is on the left, at $x = 0$. The velocity field is deduced from individual tracer trajectories, averaged in the transverse direction. The dashed line represents the front evolution, deduced from the grayscale intensity images. Right: from the velocity the total deformation ϵ is computed as $\epsilon = \int_0^t \partial_x v_x$.

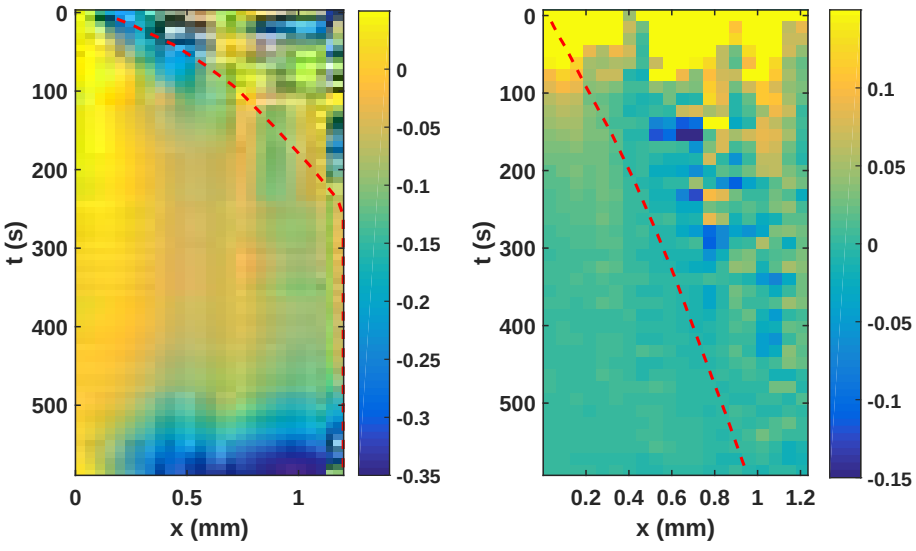

Figure 6.7: Spatio temporal plot of the velocity field in the cell, for $R_M = 160$ (Left), and $R_M = 16$ (Right). The dashed line represent the front displacement, obtained from the grayscale images.

malizing the images by the first image of the sequence, the evolution of the aggregate concentration was studied comparatively to the beginning of the diffusion reaction experiment. The molar ratio studied in the case of labelled aggregates was equal to 641 and was equivalent to $[CaCl_2] = 2.9$ M. The results are displayed in Figure 6.8. The spatio-temporal map of the normalized fluorescence intensity is equivalent to that of the relative protein concentration. Clearly, an increase of protein concentration is evidenced close to the calcium chloride reservoir. At this boundary, the concentration increased progressively by a factor of 1.7. These value is in semi-quantitative agreement with the order of magnitude of the gel deformation estimated from velocity measurements, and the qualitative comparison between figure 6.8 a) and figure 6.6 b) is striking. The progression of the diffusion-reaction front was also visible on the spatio-temporal map of the fluorescence intensity, which proved that the water flux carried protein aggregates and induced an increase of the local concentration in the gelled phase.

This observation at high molar ratio was consistent with the results presented in Chapter 5 for the highest molar ratios. When increasing molar ratio under flow and increasing $CaCl_2$ concentration during subsequent storage step, we observed a decrease of the fiber size. We hypothesised that the presence of an osmotic gradient was the driving force for this shrinkage phenomenon. In the case of fibre formation, we considered a characteristic length of about 100 μm, equivalent to the radius of the fibers. In this characteristic length we observed from Figure 6.8 (a) a flow of aggregates towards the calcium and chloride ions. It also validated the hypothesis of the formation of a gelled shell.

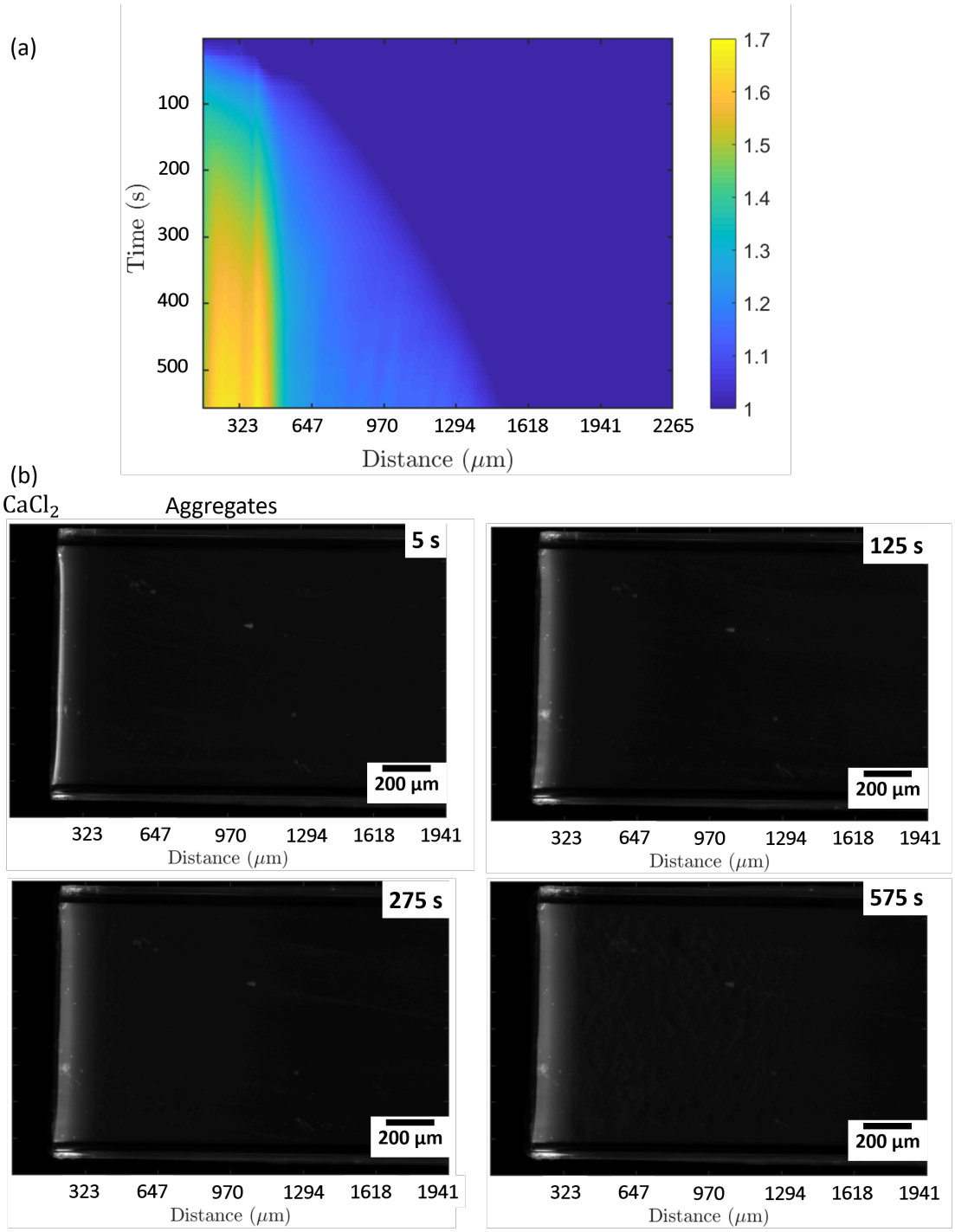

Figure 6.8: (a) Spacio-temporal image of the fluorescent intensity after normalization by the initial image for $R_M = 641$. (b) Progression of the normalized intensity within the glass capillary from the left to the right and subsequent structuring of the gel over the time.

6.4 Conclusion

In this chapter we used a bi-dimensional geometry to gain further insight on the fiber gelation mechanism occurring during the flow through radial diffusion of the calcium ions towards the aggregates. Thanks to light intensity modulation, we were able to follow the front advancement, which is rather well described by the most simple reaction-diffusion mechanism of a first-order reaction kinetics. The kinetics of the gel formation is limited at short times by the reaction and at long times by the diffusion of calcium ions. Time and length scales involved are interesting to compare to that involved in the fiber formation experiments. At low calcium concentration, fiber gelation is limited by the reaction, meaning that gelation occurred in the collecting bath, without strong gradients inside the fibers. In contrast, in the case of high calcium concentration, the gelation is limited by the diffusion of calcium ions inside the fibers, which can lead to a core-shell structure.

The addition of fluorescent particles to the suspension of aggregates showed that increasing molar ratio lead to the apparition of an osmotic flow of the aggregates toward the $CaCl_2$ reservoir. The use of labelled aggregates showed that this osmotic flow resulted in the concentration of the aggregates towards the $CaCl_2$ reservoir. We can use these results to interpret fibre formation. Combined effect of increasing gelation rate with increasing molar ratio and osmotic gradients during the flow resulted in the formation of a core-shell structure. During subsequent storage in high $CaCl_2$ storage concentration, osmotic gradients led to the shrinkage of the fibers.

It would be interesting to investigate the evolution of the mechanical properties during gelation, as a function of time and space parameters, using microrheology. The use of optical tweezers would allow us to manipulate single particles, to characterise their variation in space and time and to determine the rheological properties of the gel in formation.

We have also noticed a spacial evolution of the structure of the gel within the time which depended on the molar ratio used (Figure 6.9). We observed a step change in the intensity: a decrease followed by an increase of the intensity at 323 μm. Then, above 470 μm, we observed an abrupt decrease of the aggregates concentration followed by a constant progression of the aggregate concentration. In the last image in Figure 6.8 (b) (t = 575 s), we effectively observed a change of gel structure above 470 μm. This spacio-temporal structuring was therefore linked to the molar ratio, but its interpretation remains unclear. This observation support the purpose of the study of the evolution of the mechanical properties during gelation, as a function of time and space parameters, using microrheology.

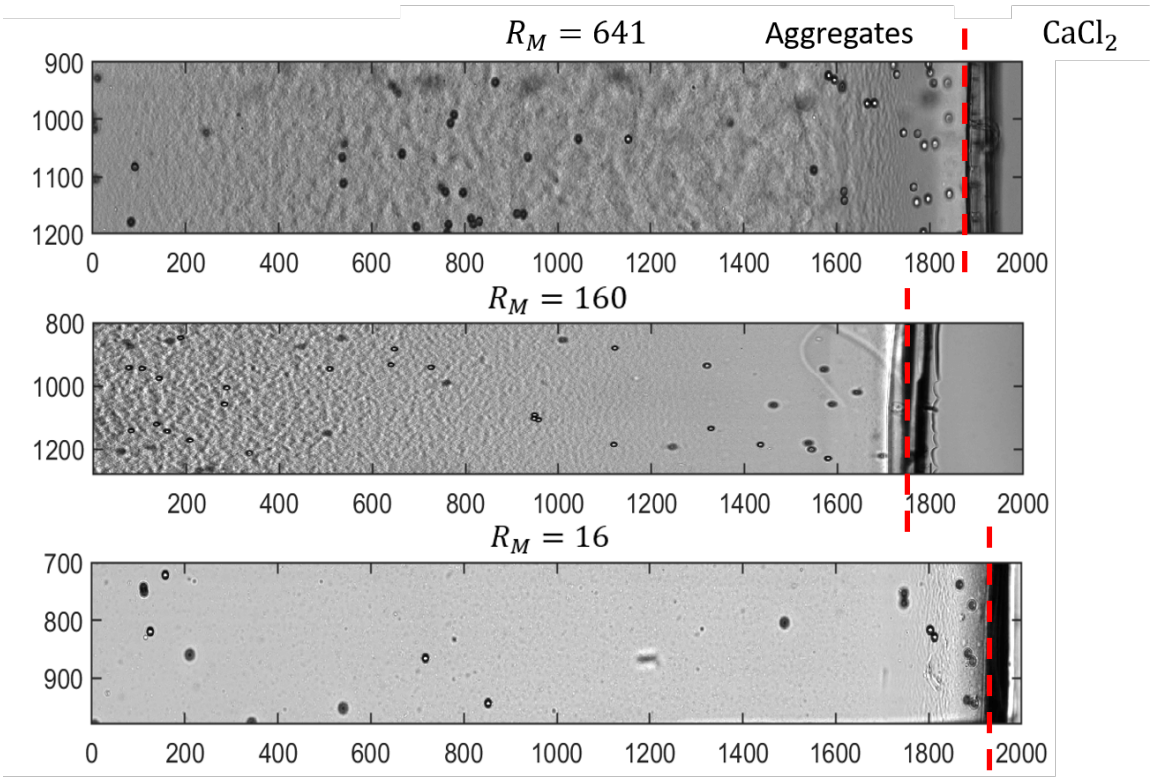

Figure 6.9: Spacial structuring of the gel within time for various molar ratios after t = 20 min.

- Kinetics of the gel formation is limited at short times by the reaction and at long times by the diffusion of calcium ions.
- Increasing molar ratio led to the apparition of an osmotic flow of the aggregates toward the $CaCl_2$ reservoir and resulted in the concentration of the aggregates.
- Combined effect of increasing gelation rate with increasing molar ratio and osmotic gradients during the flow resulted in the formation of a core-shell structure.

Chapter 7

Conclusion and perspectives

Contents

The objective of the thesis was to study new aggregation and gelation processes in order to produce new aggregate structures to improve their texturing capacity.

We studied by small angle X-ray scattering the denaturation and aggregation kinetics of aggregates formed at 4% w/w in the presence of 10 mM NaCl at pH 7 for a temperature of 92°C. We showed that at this temperature, denaturation and aggregation occurred together and that a nucleation step limited the reaction and was described by a reaction order equal to 1.5. Furthermore, we observed that the size of the aggregates formed under these conditions as well as the denaturation was almost invariant with the shear rate (for variations covering almost two orders of magnitude) under isothermal conditions. Under these conditions, the size of the aggregates formed was limited and the underlying mechanism remained an open question. However, we have shown that decreasing the aggregation temperature from 92°C to 75°C increased the final aggregate size.

To go further, it would be interesting to study these temperature kinetics for different protein concentrations by the method presented in chapter 3 in order to refine the understanding of the reaction mechanism and the mechanisms limiting the size of the aggregates.

Thanks to the development of an image analysis technique, we have quantified the size and protein mass of micrometric aggregates. We applied this characterization method to aggregates formed under different physico-chemical conditions. We showed that the size scale on which fractal aggregates of fractal dimension d_f of 2 were formed could be modulated according to the aggregation conditions (protein concentration, temperature, salt concentration). Fractal aggregates of $d_f = 2$ can reach sizes up to 50 μm when formed at the limit of the gel point at 92°C (3% 120 mM NaCl). When the gel point has passed, the constituent aggregates of the gel exhibit a fractal dimension of $d_f = 2$ only up to a size of 10 μm.

This result was very interesting on the one hand because it showed that the aggregation conditions allowed to modulate the critical size of the compact assembly of fractal aggregates. On the other hand, it brought additional elements of understanding in the formation of fractal aggregates of high viscosity value. It would also be interesting to quantify the intrinsic viscosity properties of the aggregates according to the aggregation conditions, in the light of the presented results. A microfluidic system of on-line viscosity measurement was set up during this thesis in order to measure the intrinsic viscosity of aggregates. The viscosity of a suspension was determined by $\eta = \frac{\triangle P}{Q}\frac{\pi R^4}{8\triangle L}$. The pressure variation, induced by the resistance of the fluid to the flow, was measured by a differential pressure sensor over a distance $\triangle$L. The flow rate Q was imposed. It would therefore be interesting to use this method to characterize the intrinsic viscosity of the aggregates and to relate it to the critical compact assembly size of fractal aggregates.

We jointly varied the WPI concentration, the salt concentration (NaCl, $CaCl_2$), and the temperature. It would also be interesting to decouple these effects and study their influence on the size scale up to which fractal aggregates of $d_f = 2$ are formed.

Then, we directed our study, aimed at maximizing the viscosifying properties of WPI aggregates, towards a flow structuring approach. We investigated a novel structuring of fractal aggregates at the micrometer scale through controlled flows and cold gelation mechanisms. The aggregates were shaped into fibers of about 100 microns in diameter and several centimeters in length. We studied in particular the formation and stability of these objects according to hydrodynamic and physicochemical conditions. We thus obtained a new texturizing structure in the form of core-shell fibers from fractal aggregates. These fibers were also sensitive to physico-chemical conditions and can release their contents, giving them a controlled release functionality. Unknowns remained regarding the mechanisms that destabilized the fiber. We hypothesized that they were related to changes in net and/or effective charge density at the surface of the aggregates inducing an increase in electrostatic repulsions. It would also be interesting to use labeled proteins in order to follow the destabilization of the fiber through the fluorescence intensity.

We also showed that osmotic phenomena were involved in the shrinkage of the fiber diameter. It would be interesting to study the rheological properties of fiber suspensions for texturing applications. It would also be interesting to characterize their mechanical properties, as their stiffness may influence their entanglement and rheological properties.

Several tests to estimate the mechanical properties of the fibers were considered. The objective was to study the deformation of the fiber under increasing stress. First, we applied a displacement (-Ox) via a motorized stage, on which a petri dish containing the fiber was placed, with a constant velocity field while the fiber was stopped by a fixed rod. The goal was to define a critical velocity above which the fibers were deformed (Figure 7.1-a). This method would allow to measure the bending modulus of the fibers. To study the stress-strain relationship until failure, we used a tensile test. Each end of the fiber was gripped by a flat clamp and pulled horizontally in the opposite direction. The maximum elongation before fiber breakage was thus measured (Figure 7.1-b). In addition, the breakage could occur at several locations in the fibers. This test gave us indications that some fibers could undergo a percentage elongation of 100 %. Other tests of mechanical properties estimation remained to be set up in order to try to modulate the mechanical properties of the fiber according to the formulation.

Finally, we have shown the existence of an increase in the local concentration of the aggregates in the form of a gelled shell, linked to an osmotic flow, in a simplified geometry. This flow, which we interpreted as the consequence of the partially ion permeable nature of the gel, is, to our knowledge, an original observation that deserves to be further investigated by systematic experiments. Independently of its physical origin, this phenomenon favored the formation of core-shell fibers. The preliminary experiments required a deeper understanding of the mechanisms at the origin of the intensity difference on which our temporal monitoring of the front formation is based. Indeed, questions remained about the analysis of the front evolution. It seemed difficult to decouple the analysis of the diffusion from the reaction of calcium ions by microscopy. It would be interesting to study the evolution of rheological properties

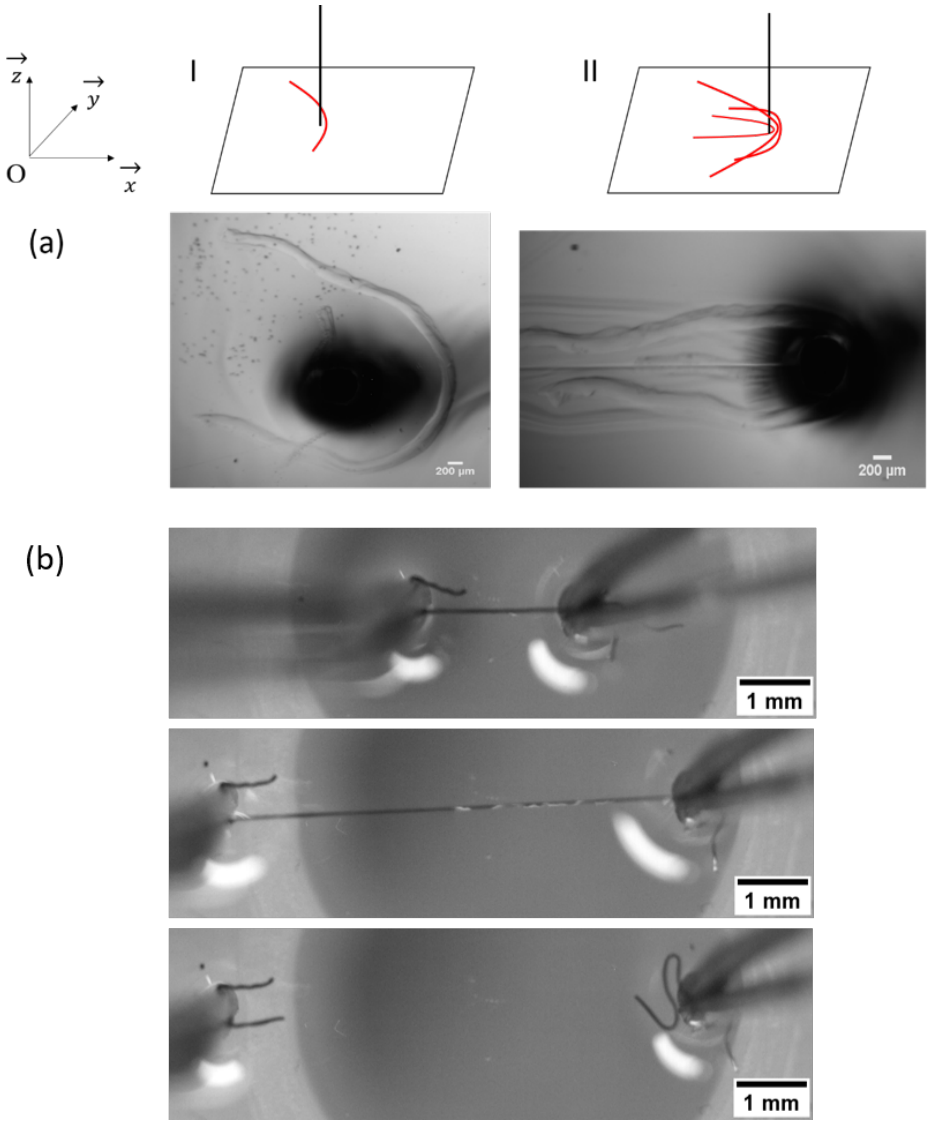

Figure 7.1: Tests set up to evaluate the mechanical properties of gelled fibers formed under flow. (a): A horizontal displacement velocity is imposed on the fiber which is held fixed by a stop point. (I): fiber in the initial state, (II): fiber deformed under a displacement speed of 2 mm/s. (b): Fiber elongation test, each end of the fiber was gripped by a flat clamp and pulled horizontally in the opposite direction.

during the diffusion reactions of calcium ions in the aggregate suspension. To do this, an optical tweezers system could be used to trap a particle added to the aggregate suspension and follow the evolution of the elastic modulus over time and for different molar ratios.

List of Figures

List of Tables

Bibliography

[1] K. Ako, D. Durand, T. Nicolai, and L. Becu. Quantitative analysis of confocal laser scanning microscopy images of heat-set globular protein gels. *Food Hydrocolloids*, 23(4):1111–1119, 2009.

[2] K. Ako, T. Nicolai, and D. Durand. Salt-induced gelation of globular protein aggregates: structure and kinetics. *Biomacromolecules*, 11(4):864–871, 2010.

[3] A. C. Alting, H. H. de Jongh, R. W. Visschers, and J.-W. F. Simons. Physical and chemical interactions in cold gelation of food proteins. *Journal of Agricultural and Food Chemistry*, 50(16):4682–4689, 2002.

[4] A. C. Alting, R. J. Hamer, C. G. de Kruif, M. Paques, and R. W. Visschers. Number of thiol groups rather than the size of the aggregates determines the hardness of cold set whey protein gels. *Food Hydrocolloids*, 17(4):469–479, 2003.

[5] A. C. Alting, M. Weijers, E. H. de Hoog, A. M. van de Pijpekamp, M. A. Cohen Stuart, R. J. Hamer, C. G. de Kruif, and R. W. Visschers. Acid-induced cold gelation of globular proteins: effects of protein aggregate characteristics and disulfide bonding on rheological properties. *Journal of agricultural and food chemistry*, 52(3):623–631, 2004.

[6] R. Andoyo, F. Guyomarc'h, and M.-H. Famelart. Acid gelation of whey protein microbeads of different sizes. *Dairy Science & Technology*, 96(2):213–225, 2016.

[7] R. Aris. On the dispersion of a solute in a fluid flowing through a tube. *Proc. Roy. Soc. A.*, 235:67–77, 1956.

[8] P. Aymard, D. Durand, and T. Nicolai. The effect of temperature and ionic strength on the dimerisation of β-lactoglobulin. *International journal of biological macromolecules*, 19(3):213–221, 1996.

[9] P. Aymard, J.-C. Gimel, T. Nicolai, and D. Durand. Experimental evidence for a two-step process in the aggregation of β-lactoglobulin at ph 7. *Journal de Chimie Physique et de Physico-Chimie Biologique*, 93:987–997, 1996.

[10] P. Aymard, D. Durand, T. Nicolai, and J.-C. Gimel. Fractality of globular protein aggregates: from the molecular to the microscopic level. *Fractals*, 5 (supp02):23–43, 1997.

[11] P. Aymard, T. Nicolai, D. Durand, and A. Clark. Static and dynamic scattering of β-lactoglobulin aggregates formed after heat-induced denaturation at ph 2. *Macromolecules*, 32(8):2542–2552, 1999.

[12] S. Barbut and D. Drake. Effect of reheating on sodium-induced cold gelation of whey proteins. *Food research international*, 30(2):153–157, 1997.

[13] S. Barbut and E. Foegeding. Ca2+-induced gelation of pre-heated whey protein isolate. *Journal of Food Science*, 58(4):867–871, 1993.

[14] K. Baussay, C. Le Bon, T. Nicolai, D. Durand, and J.-P. Busnel. Influence of the ionic strength on the heat-induced aggregation of the globular protein β-lactoglobulin at ph 7. *International Journal of Biological Macromolecules*, 34(1-2):21–28, 2004.

[15] P. Bernado and D. I. Svergun. Structural analysis of intrinsically disordered proteins by small-angle x-ray scattering. *Molecular Biosystems*, 8(1):151–167, 2012.

[16] M. Betz, J. Hörmansperger, T. Fuchs, and U. Kulozik. Swelling behaviour, charge and mesh size of thermal protein hydrogels as influenced by ph during gelation. *Soft Matter*, 8(8):2477–2485, 2012.

[17] O. Bonhomme, J. Leng, and A. Colin. Microfluidic wet-spinning of alginate microfibers: A theoretical analysis of fiber formation. *Soft Matter*, 8(41):10641–10649, 2012.

[18] W. K. Brown and K. H. Wohletz. Derivation of the weibull distribution based on physical principles and its connection to the rosin–rammler and lognormal distributions. *Journal of Applied Physics*, 78(4):2758–2763, 1995.

[19] S. Brownlow, J. H. M. Cabral, R. Cooper, D. R. Flower, S. J. Yewdall, I. Polikarpov, A. C. North, and L. Sawyer. Bovine β-lactoglobulin at 1.8 å resolution—still an enigmatic lipocalin. *Structure*, 5(4):481–495, 1997.

[20] C. Bryant and D. McClements. Influence of nacl and cacl2 on cold-set gelation of heat-denatured whey protein. *Journal of Food Science*, 65(5):801–804, 2000.

[21] A. I. Campbell, V. J. Anderson, J. S. van Duijneveldt, and P. Bartlett. Dynamical arrest in attractive colloids: The effect of long-range repulsion. *Physical Review Letters*, 94(20):208301, 2005.

[22] F. Cardinaux, A. Stradner, P. Schurtenberger, F. Sciortino, and E. Zaccarelli. Modeling equilibrium clusters in lysozyme solutions. *EPL (Europhysics Letters)*, 77(4):48004, 2007.

[23] P. C. Chatwin. The approach to normality of the concentration distribution of a solute in a solvent flowing along a straight pipe. *Journal of Fluid Mechanics*, 43(2):321–352, 1970. doi: 10.1017/S0022112070002409.

[24] P. C. Chatwin. The initial development of longitudinal dispersion in straight tubes. *Journal of Fluid Mechanics*, 80(1):33–48, 1977. doi: 10.1017/S0022112077001529.

[25] Y. Cheng, F. Zheng, J. Lu, L. Shang, Z. Xie, Y. Zhao, Y. Chen, and Z. Gu. Bioinspired multicompartmental microfibers from microfluidics. *Advanced Materials*, 26(30):5184–5190, 2014.

[26] T. Croguennec, D. Mollé, R. Mehra, and S. Bouhallab. Spectroscopic characterization of heat-induced nonnative β-lactoglobulin monomers. *Protein Science*, 13(5):1340–1346, 2004.

[27] E. L. Cussler. *Diffusion: mass transfer in fluid systems*. Cambridge university press, 2009.

[28] F. Dannenberg and H.-G. Kessler. Reaction kinetics of the denaturation of whey proteins in milk. *Journal of Food Science*, 53(1):258–263, 1988.

[29] D. de Guibert, M. Hennetier, F. Martin, T. Six, Y. Gu, C. Le Floch-Fouéré, G. Delaplace, and R. Jeantet. Flow process and heating conditions modulate the characteristics of whey protein aggregates. *Journal of Food Engineering*, 264:109675, 2020.

[30] M. A. de la Fuente, H. Singh, and Y. Hemar. Recent advances in the characterisation of heat-induced aggregates and intermediates of whey proteins. *Trends in Food Science & Technology*, 13(8):262 – 274, 2002.

[31] J. De Wit. Thermal stability and functionality of whey proteins. *Journal of Dairy Science*, 73(12):3602–3612, 1990.

[32] J. de Wit. Thermal behaviour of bovine β-lactoglobulin at temperatures up to 150°c. a review. *Trends in Food Science & Technology*, 20(1):27 – 34, 2009.

[33] J. De Wit. Thermal behaviour of bovine β-lactoglobulin at temperatures up to 150 c. a review. *Trends in Food Science & Technology*, 20(1):27–34, 2009.

[34] R. J. Delahaije, H. Gruppen, E. L. van Eijk-van Boxtel, L. Cornacchia, and P. A. Wierenga. Controlling the ratio between native-like, non-native-like, and aggregated β-lactoglobulin after heat treatment. *Journal of agricultural and food chemistry*, 64(21):4362–4370, 2016.

[35] M. Dissanayake, L. Ramchandran, C. Piyadasa, and T. Vasiljevic. Influence of heat and ph on structure and conformation of whey proteins. *International Dairy Journal*, 28(2):56 – 61, 2013.

[36] L. Donato, E. Kolodziejcyk, and M. Rouvet. Mixtures of whey protein microgels and soluble aggregates as building blocks to control rheology and structure of acid induced cold-set gels. *Food Hydrocolloids*, 25(4):734–742, 2011.

[37] D. Durand, J. C. Gimel, and T. Nicolai. Aggregation, gelation and phase separation of heat denatured globular proteins. *Physica A: Statistical Mechanics and its Applications*, 304(1-2):253–265, 2002.

[38] N. Erabit, D. Flick, and G. Alvarez. Formation of β-lactoglobulin aggregates during thermomechanical treatments under controlled shear and temperature conditions. *Journal of Food Engineering*, 120:57–68, 2014.

[39] N. Erabit, F. T. Ndoye, G. Alvarez, and D. Flick. Coupling population balance model and residence time distribution for pilot-scale modelling of β-lactoglobulin aggregation process. *Journal of Food Engineering*, 177:31–41, 2016.

[40] D. Galani and R. K. Owusu Apenten*. Heat-induced denaturation and aggregation of β-lactoglobulin: kinetics of formation of hydrophobic and disulphide-linked aggregates. *International journal of food science & technology*, 34(5-6): 467–476, 1999.

[41] E. Ganani and R. Powell. Suspensions of rodlike particles: Literature review and data correlations. *Journal of composite materials*, 19(3):194–215, 1985.

[42] A. Gholampour and T. Ozbakkaloglu. A review of natural fiber composites: Properties, modification and processing techniques, characterization, applications. *Journal of Materials Science*, 55(3):829–892, 2020.

[43] J. C. Gimel, D. Durand, and T. Nicolai. Structure and distribution of aggregates formed after heat-induced denaturation of globular proteins. *Macromolecules*, 27(2):583–589, 1994.

[44] W. S. Gosal, A. H. Clark, P. D. Pudney, and S. B. Ross-Murphy. Novel amyloid fibrillar networks derived from a globular protein: β-lactoglobulin. *Langmuir*, 18(19):7174–7181, 2002.

[45] S. Gunasekaran, S. Ko, and L. Xiao. Use of whey proteins for encapsulation and controlled delivery applications. *Journal of food engineering*, 83(1):31–40, 2007.

[46] P. Hongsprabhas and S. Barbut. Ca2+-induced cold gelation of whey protein isolate: effect of two-stage gelation. *Food Research International*, 30(7):523–527, 1997.

[47] P. Hongsprabhas and S. Barbut. Protein and salt effects on ca2+-induced cold gelation of whey protein isolate. *Journal of Food Science*, 62(2):382–385, 1997.

[48] M. Hu, R. Deng, K. M. Schumacher, M. Kurisawa, H. Ye, K. Purnamawati, and J. Y. Ying. Hydrodynamic spinning of hydrogel fibers. *Biomaterials*, 31 (5):863–869, 2010.

[49] X. Hu, M. Tian, B. Sun, L. Qu, S. Zhu, and X. Zhang. Hydrodynamic alignment and microfluidic spinning of strength-reinforced calcium alginate microfibers. *Materials Letters*, 230:148–151, 2018.

[50] S. Iametti, B. De Gregori, G. Vecchio, and F. Bonomi. Modifications occur at different structural levels during the heat denaturation of β-lactoglobulin. *European Journal of Biochemistry*, 237(1):106–112, 1996.

[51] F. P. Incropera, A. S. Lavine, T. L. Bergman, and D. P. DeWitt. *Fundamentals of heat and mass transfer*. Wiley, 2007.

[52] W. Inthavong, A. Kharlamova, C. Chassenieux, and T. Nicolai. Structure and flow of dense suspensions of protein fractal aggregates in comparison with microgels. *Soft matter*, 12(10):2785–2793, 2016.

[53] A. Jelińska, A. Zagożdżon, M. Górecki, A. Wisniewska, J. Frelek, and R. Holyst. Denaturation of proteins by surfactants studied by the taylor dispersion analysis. *PLOS ONE*, 12(4):1–11, 04 2017. doi: 10.1371/journal.pone.0175838. URL `https://doi.org/10.1371/journal.pone.0175838`.

[54] S. Jeyarajah and J. C. Allen. Calcium binding and salt-induced structural changes of native and preheated. beta.-lactoglobulin. *Journal of Agricultural and Food Chemistry*, 42(1):80–85, 1994.

[55] Z. Ju and A. Kilara. Aggregation induced by calcium chloride and subsequent thermal gelation of whey protein isolate. *Journal of Dairy Science*, 81(4):925–931, 1998.

[56] J.-M. Jung, G. Savin, M. Pouzot, C. Schmitt, and R. Mezzenga. Structure of heat-induced β-lactoglobulin aggregates and their complexes with sodium-dodecyl sulfate. *Biomacromolecules*, 9:2477–2486, 2008.

[57] Y. Ker and R. Toledo. Influence of shear treatments on consistency and gelling properties of whey protein isolate suspensions. *Journal of Food Science*, 57(1): 82–85, 1992.

[58] F. Kerche, M. Weterings, and M. Beyrer. The effect of temperature and shear upon technological properties of whey protein concentrate: Aggregation in a tubular heat exchanger. *International Dairy Journal*, 60:32–38, 2016.

[59] H.-G. Kessler and H.-J. Beyer. Thermal denaturation of whey proteins and its effect in dairy technology. *International Journal of Biological Macromolecules*, 13(3):165–173, 1991.

[60] A. Kharlamova, C. Chassenieux, and T. Nicolai. Acid-induced gelation of whey protein aggregates: Kinetics, gel structure and rheological properties. *Food Hydrocolloids*, 81:263–272, 2018.

[61] A. Kharlamova, T. Nicolai, and C. Chassenieux. Calcium-induced gelation of whey protein aggregates: Kinetics, structure and rheological properties. *Food Hydrocolloids*, 79:145–157, 2018.

[62] A. Kharlamova, T. Nicolai, and C. Chassenieux. Gelation of whey protein fractal aggregates induced by the interplay between added hcl, cacl2 and nacl. *International Dairy Journal*, 111:104824, 2020.

[63] A. G. Kikhney and D. I. Svergun. A practical guide to small angle x-ray scattering (saxs) of flexible and intrinsically disordered proteins. *FEBS letters*, 589(19):2570–2577, 2015.

[64] S. Ko and S. Gunasekaran. Preparation of sub-100-nm β-lactoglobulin (blg) nanoparticles. *Journal of microencapsulation*, 23(8):887–898, 2006.

[65] E. Kolodziejczyk, V. Petkova, J.-J. Benattar, M. E. Leser, and M. Michel. Effect of fluorescent labeling of β-lactoglobulin on film and interfacial properties in relation to confocal fluorescence microscopy. *Colloids and Surfaces A: Physicochemical and Engineering Aspects*, 279(1-3):159–166, 2006.

[66] D. E. Kuehner, J. Engmann, F. Fergg, M. Wernick, H. W. Blanch, and J. M. Prausnitz. Lysozyme net charge and ion binding in concentrated aqueous electrolyte solutions. *The Journal of Physical Chemistry B*, 103(8):1368–1374, 1999.

[67] K. R. Kuhn, Â. L. F. Cavallieri, and R. L. Da Cunha. Cold-set whey protein gels induced by calcium or sodium salt addition. *International journal of food science & technology*, 45(2):348–357, 2010.

[68] M. Latini and A. J. Bernoff. Transient anomalous diffusion in poiseuille flow. *Journal of Fluid Mechanics*, 441:399–411, 2001. doi: 10.1017/S0022112001004906.

[69] C. Le Bon, T. Nicolai, and D. Durand. Growth and structure of aggregates of heat-denatured β-lactoglobulin. *International journal of food science & technology*, 34(5-6):451–465, 1999.

[70] C. Le Bon, T. Nicolai, and D. Durand. Kinetics of aggregation and gelation of globular proteins after heat-induced denaturation. *Macromolecules*, 32(19): 6120–6127, 1999.

[71] M. Li, M. A. Auty, J. A. O'Mahony, A. L. Kelly, and A. Brodkorb. Covalent labelling of β-casein and its effect on the microstructure and physico-chemical properties of emulsions stabilized by β-casein and whey protein isolate. *Food Hydrocolloids*, 61:504–513, 2016.

[72] W. Liu, D. I. Wilson, X. D. Chen, and R. Mercadé-Prieto. Quantification of the local protein content in hydrogels undergoing swelling and dissolution at alkaline ph using fluorescence microscopy. *Food and bioprocess technology*, 11 (3):572–584, 2018.

[73] Y. D. Livney. Milk proteins as vehicles for bioactives. *Current opinion in colloid & interface science*, 15(1-2):73–83, 2010.

[74] Y.-F. Maa and C. C. Hsu. Effect of high shear on proteins. *Biotechnology and bioengineering*, 51(4):458–465, 1996.

[75] N. Mahmoudi, S. Mehalebi, T. Nicolai, D. Durand, and A. Riaublanc. Light-scattering study of the structure of aggregates and gels formed by heat-denatured whey protein isolate and β-lactoglobulin at neutral ph. *Journal of Agricultural and Food Chemistry*, 55(8):3104–3111, 2007.

[76] G. A. Manderson, M. J. Hardman, and L. K. Creamer. Effect of heat treatment on bovine β-lactoglobulin a, b, and c explored using thiol availability and fluorescence. *Journal of Agricultural and Food Chemistry*, 47(9):3617–3627, 1999.

[77] A. Marangoni, S. Barbut, S. McGauley, M. Marcone, and S. Narine. On the structure of particulate gels—the case of salt-induced cold gelation of heat-denatured whey protein isolate. *Food hydrocolloids*, 14(1):61–74, 2000.

[78] A. Mediwaththe, D. Bogahawaththa, M. K. Grewal, J. Chandrapala, and T. Vasiljevic. Structural changes of native milk proteins subjected to controlled shearing and heating. *Food Research International*, 114:151–158, 2018.

[79] S. Mehalebi, T. Nicolai, and D. Durand. Light scattering study of heat-denatured globular protein aggregates. *International Journal of Biological Macromolecules*, 43(2):129–135, 2008.

[80] R. Mezzenga and P. Fischer. The self-assembly, aggregation and phase transitions of food protein systems in one, two and three dimensions. *Reports on Progress in Physics*, 76(4):046601, 2013.

[81] C. Moitzi, L. Donato, C. Schmitt, L. Bovetto, G. Gillies, and A. Stradner. Structure of β-lactoglobulin microgels formed during heating as revealed by small-angle x-ray scattering and light scattering. *Food Hydrocolloids*, 25(7): 1766–1774, 2011.

[82] H. Mondésert, F. Bossard, and D. Favier. Anisotropic electrospun honeycomb polycaprolactone scaffolds: Elaboration, morphological and mechanical properties. *Journal of the Mechanical Behavior of Biomedical Materials*, 113:104124, 2021.

[83] A. M. Morris, M. A. Watzky, and R. G. Finke. Protein aggregation kinetics, mechanism, and curve-fitting: A review of the literature. *Biochimica et Biophysica Acta*, 1794:375–397, 2009.

[84] F. Nallet. Introduction à la diffusion aux petits angles. Lecture, May 2009. URL `https://cel.archives-ouvertes.fr/cel-00577143`.

[85] B. T. Nguyen, C. Chassenieux, T. Nicolai, and C. Schmitt. Effect of the ph and nacl on the microstructure and rheology of mixtures of whey protein isolate and casein micelles upon heating. *Food Hydrocolloids*, 70:114–122, 2017.

[86] T. Nicolai. Gelation of food protein-protein mixtures. *Advances in colloid and interface science*, 270:147–164, 2019.

[87] T. Nicolai and D. Durand. Controlled food protein aggregation for new functionality. *Current Opinion in Colloid & Interface Science*, 18(4):249–256, 2013.

[88] T. Nicolai, C. Urban, and P. Schurtenberger. Light scattering study of turbid heat-set globular protein gels using cross-correlation dynamic light scattering. *Journal of colloid and interface science*, 240(2):419–424, 2001.

[89] T. Nicolai, M. Britten, and C. Schmitt. β-lactoglobulin and wpi aggregates: Formation, structure and applications. *Food Hydrocolloids*, 25(8):1945–1962, 2011.

[90] I. Nicorescu, A. Riaublanc, C. Loisel, C. Vial, G. Djelveh, G. Cuvelier, and J. Legrand. Impact of protein self-assemblages on foam properties. *Food Research International*, 42(10):1434–1445, 2009.

[91] M. H. Oztop, K. L. McCarthy, M. J. McCarthy, and M. Rosenberg. Uptake of divalent ions (mn+ 2 and ca+ 2) by heat-set whey protein gels. *Journal of food science*, 77(2):E68–E73, 2012.

[92] H.-Y. Park, I.-H. Song, J.-H. Kim, and W.-S. Kim. Preparation of thermally denatured albumin gel and its ph-sensitive swelling. *International journal of pharmaceutics*, 175(2):231–236, 1998.

[93] J. Perez, P. Vachette, D. Russo, M. Desmadril, and D. Durand. Heat-induced unfolding of neocarzinostatin, a small all-β protein investigated by small-angle x-ray scattering. *Journal of Molecular Biology*, 308(4):721–743, 2001.

[94] J. Pérez, P. Vachette, D. Russo, M. Desmadril, and D. Durand. Heat-induced unfolding of neocarzinostatin, a small all-β protein investigated by small-angle x-ray scattering. *Journal of Molecular Biology*, 308:721–743, 2001.

[95] J. Petit, T. Six, A. Moreau, G. Ronse, and G. Delaplace. β-lactoglobulin denaturation, aggregation, and fouling in a plate heat exchanger: pilot-scale experiments and dimensional analysis. *Chemical Engineering Science*, 101:432–450, 2013.

[96] C. J. Petrie. The rheology of fibre suspensions. *Journal of Non-Newtonian Fluid Mechanics*, 87(2-3):369–402, 1999.

[97] T. Phan-Xuan, D. Durand, T. Nicolai, L. Donato, C. Schmitt, and L. Bovetto. On the crucial importance of the ph for the formation and self-stabilization of protein microgels and strands. *Langmuir*, 27(24):15092–15101, 2011.

[98] T. Phan-Xuan, D. Durand, T. Nicolai, L. Donato, C. Schmitt, and L. Bovetto. Tuning the structure of protein particles and gels with calcium or sodium ions. *Biomacromolecules*, 14(6):1980–1989, 2013.

[99] T. Phan-Xuan, D. Durand, T. Nicolai, L. Donato, C. Schmitt, and L. Bovetto. Heat induced formation of beta-lactoglobulin microgels driven by addition of calcium ions. *Food Hydrocolloids*, 34:227–235, 2014.

[100] M. Pouzot, T. Nicolai, D. Durand, and L. Benyahia. Structure factor and elasticity of a heat-set globular protein gel. *Macromolecules*, 37(2):614–620, 2004.

[101] M. Pouzot, T. Nicolai, R. Visschers, and M. Weijers. X-ray and light scattering study of the structure of large protein aggregates at neutral ph. *Food Hydrocolloids*, 19(2):231–238, 2005.

[102] P. Puyol, M. Perez, and D. Horne. Heat-induced gelation of whey protein isolates (wpi): effect of nacl and protein concentration. *Food Hydrocolloids*, 15 (3):233–237, 2001.

[103] B. Y. Qin, M. C. Bewley, L. K. Creamer, H. M. Baker, E. N. Baker, and G. B. Jameson. Structural basis of the tanford transition of bovine β-lactoglobulin. *Biochemistry*, 37(40):14014–14023, 1998.

[104] K. Rade-Kukic, C. Schmitt, and H. M. Rawel. Formation of conjugates between β-lactoglobulin and allyl isothiocyanate: Effect on protein heat aggregation, foaming and emulsifying properties. *Food Hydrocolloids*, 25(4):694–706, 2011.

[105] R. P. Rambo and J. A. Tainer. Characterizing flexible and intrinsically unstructured biological macromolecules by sas using the porod-debye law. *Biopolymers*, 95(8):559–571, 2011.

[106] P. Relkin and D. M. Mulvihill. Thermal unfolding of β-lactoglobulin, α-lactalbumin, and bovine serum albumin. a thermodynamic approach. *Critical Reviews in Food Science and Nutrition*, 36(6):565–601, 1996.

[107] C. J. Roberts. Non-native protein aggregation kinetics. *Biotechnology and Bioengineering*, 98:927–938, 2007.

[108] F. Robin, H. P. Schuchmann, and S. Palzer. Dietary fiber in extruded cereals: Limitations and opportunities. *Trends in Food Science & Technology*, 28(1): 23–32, 2012.

[109] S. P. F. M. Roefs and K. G. De Kruif. A model for the denaturation and aggregation of β-lactoglobulin. *European Journal of Biochemistry*, 226:883–889, 1994.

[110] A. Salis, M. Bostrom, L. Medda, F. Cugia, B. Barse, D. F. Parsons, B. W. Ninham, and M. Monduzzi. Measurements and theoretical interpretation of points of zero charge/potential of bsa protein. *Langmuir*, 27(18):11597–11604, 2011.

[111] C. Schmitt, C. Sanchez, A. Lamprecht, D. Renard, C.-M. Lehr, C. G. de Kruif, and J. Hardy. Study of β-lactoglobulin/acacia gum complex coacervation by diffusing-wave spectroscopy and confocal scanning laser microscopy. *Colloids and Surfaces B: Biointerfaces*, 20(3):267–280, 2001.

[112] C. Schmitt, C. Moitzi, C. Bovay, M. Rouvet, L. Bovetto, L. Donato, M. E. Leser, P. Schurtenberger, and A. Stradner. Internal structure and colloidal behaviour of covalent whey protein microgels obtained by heat treatment. *Soft Matter*, 6(19):4876–4884, 2010.

[113] A. Shukla, E. Mylonas, E. Di Cola, S. Finet, P. Timmins, T. Narayanan, and D. I. Svergun. Absence of equilibrium cluster phase in concentrated lysozyme solutions. *Proceedings of the National Academy of Sciences*, 105(13):5075–5080, 2008.

[114] J. V. Silva, G. Balakrishnan, C. Schmitt, C. Chassenieux, and T. Nicolai. Heat-induced gelation of aqueous micellar casein suspensions as affected by globular protein addition. *Food Hydrocolloids*, 82:258–267, 2018.

[115] M. Simmons, P. Jayaraman, and P. Fryer. The effect of temperature and shear rate upon the aggregation of whey protein and its implications for milk fouling. *Journal of Food Engineering*, 79(2):517–528, 2007.

[116] M. Simmons, P. Jayaraman, and P. Fryer. The effect of temperature and shear rate upon the aggregation of whey protein and its implications for milk fouling. *Journal of Food Engineering*, 79(2):517–528, 2007.

[117] J.-W. F. Simons, H. A. Kosters, R. W. Visschers, and H. H. de Jongh. Role of calcium as trigger in thermal β-lactoglobulin aggregation. *Archives of biochemistry and biophysics*, 406(2):143–152, 2002.

[118] M. v. Smoluchowski. Versuch einer mathematischen theorie der koagulationskinetik kolloider lösungen. *Zeitschrift für physikalische Chemie*, 92(1):129–168, 1918.

[119] F. Sordo, E.-R. Janecek, Y. Qu, V. Michaud, F. Stellacci, J. Engmann, T. J. Wooster, and F. Sorin. Microstructured fibers for the production of food. *Advanced Materials*, 31(14):1807282, 2019.

[120] C. Sorensen. Light scattering by fractal aggregates: a review. *Aerosol Science & Technology*, 35(2):648–687, 2001.

[121] T. Spiegel. Whey protein aggregation under shear conditions–effects of lactose and heating temperature on aggregate size and structure. *International Journal of Food Science & Technology*, 34(5-6):523–531, 1999.

[122] T. Spiegel and M. Huss. Whey protein aggregation under shear conditions–effects of ph-value and removal of calcium. *International journal of food science & technology*, 37(5):559–568, 2002.

[123] A. Stradner, H. Sedgwick, F. Cardinaux, W. C. Poon, S. U. Egelhaaf, and P. Schurtenberger. Equilibrium cluster formation in concentrated protein solutions and colloids. *Nature*, 432(7016):492, 2004.

[124] G. I. Taylor. Dispersion of soluble matter in solvent flowing slowly through a tube. *Proc. Roy. Soc. A.*, 219:186–203, 1953.

[125] I. Teraoka. *Polymer solutions*. John Wiley & Sons, Inc, 2002.

[126] A. Tolkach and U. Kulozik. Reaction kinetic pathway of reversible and irreversible thermal denaturation of β-lactoglobulin. *Le Lait*, 87(4-5):301–315, 2007.

[127] A. Tolkach and U. Kulozik. Reaction kinetic pathway of reversible and irreversible thermal denaturation of β-lactoglobulin. *Le Lait*, 87(4-5):301–315, 2007.

[128] C. Veerman, H. Baptist, L. M. Sagis, and E. van der Linden. A new multistep ca2+-induced cold gelation process for β-lactoglobulin. *Journal of agricultural and food chemistry*, 51(13):3880–3885, 2003.

[129] C. Veerman, G. de Schiffart, L. M. Sagis, and E. van der Linden. Irreversible self-assembly of ovalbumin into fibrils and the resulting network rheology. *International Journal of Biological Macromolecules*, 33(1-3):121–127, 2003.

[130] M. Verheul, S. P. F. M. Roefs, and K. G. de Kruif. Kinetics of heat-induced aggregation of β-lactoglobulin. *Journal of Agriculture and Food Chemistry*, 46: 896–903, 1998.

[131] M. Verheul, J. S. Pedersen, S. P. Roefs, and K. G. de Kruif. Association behavior of native β-lactoglobulin. *Biopolymers: Original Research on Biomolecules*, 49(1):11–20, 1999.

[132] A. Vilotte, H. Bodiguel, K. Ako, D. Z. Gunes, C. Schmitt, and C. de Loubens. Kinetic and structural characterization of whey protein aggregation in a millifluidic continuous process. *Food Hydrocolloids*, 110:106137, 2021.

[133] R. Vreeker, L. Hoekstra, D. Den Boer, and W. Agterof. Fractal aggregation of whey proteins. *Food Hydrocolloids*, 6(5):423–435, 1992.

[134] M. Weijers, R. W. Visschers, and T. Nicolai. Light scattering study of heat-induced aggregation and gelation of ovalbumin. *Macromolecules*, 35(12):4753–4762, 2002.

[135] D. Weinbuch, S. Zölls, M. Wiggenhorn, W. Friess, G. Winter, W. Jiskoot, and A. Hawe. Micro–flow imaging and resonant mass measurement (archimedes)–complementary methods to quantitatively differentiate protein particles and silicone oil droplets. *Journal of Pharmaceutical Sciences*, 102(7):2152–2165, 2013.

[136] M. Wolz, E. Mersch, and U. Kulozik. Thermal aggregation of whey proteins under shear stress. *Food Hydrocolloids*, 56:396–404, 2016.

[137] Y. L. Xiong, K. A. Dawson, and L. Wan. Thermal aggregation of β-lactoglobulin: effect of ph, ionic environment, and thiol reagent. *Journal of Dairy Science*, 76(1):70–77, 1993.

[138] Y. Yu, F. Fu, L. Shang, Y. Cheng, Z. Gu, and Y. Zhao. Bioinspired helical microfibers from microfluidics. *Advanced Materials*, 29(18):1605765, 2017.

[139] E. Zaccarelli. Colloidal gels: equilibrium and non-equilibrium routes. *Journal of Physics: Condensed Matter*, 19(32):323101, 2007.

[140] F. Zhang, S. Weggler, M. J. Ziller, L. Ianeselli, B. S. Heck, A. Hildebrandt, O. Kohlbacher, M. W. Skoda, R. M. Jacobs, and F. Schreiber. Universality of protein reentrant condensation in solution induced by multivalent metal ions. *Proteins: Structure, Function, and Bioinformatics*, 78(16):3450–3457, 2010.

[141] F. Zhang, G. Zocher, A. Sauter, T. Stehle, and F. Schreiber. Novel approach to controlled protein crystallization through ligandation of yttrium cations. *Journal of Applied Crystallography*, 44(4):755–762, 2011.

[142] Y. Zhang. Cancer-preventive isothiocyanates: measurement of human exposure and mechanism of action. *Mutation Research/Fundamental and Molecular Mechanisms of Mutagenesis*, 555(1-2):173–190, 2004.

[143] J. Zhong, S. D. Mohan, A. Bell, A. Terry, G. R. Mitchell, and F. J. Davis. Electrospinning of food-grade nanofibres from whey protein. *International journal of biological macromolecules*, 113:764–773, 2018.

[144] E. B. Zhulina and O. V. Borisov. Theory of block polymer micelles: Recent advances and current challenges. *Macromolecules*, 45:4429–4440, 2012.

[145] M. Zirnsak, D. Hur, and D. Boger. Normal stresses in fibre suspensions. *Journal of non-newtonian fluid mechanics*, 54:153–193, 1994.

[146] C. Zittle, E. DellaMonica, R. Rudd, and J. Custer. The binding of calcium ions by β-lactoglobulin both before and after aggregation by heating in the presence of calcium ions. *Journal of the American Chemical society*, 79(17):4661–4666, 1957.

[147] N. Zumaeta, E. P. Byrne, and J. J. Fitzpatrick. Predicting precipitate particle breakage in a pipeline: Effect of agitation intensity during precipitate formation. *Chemical engineering science*, 61(24):7991–8003, 2006.

[148] R. Zuniga, A. Tolkach, U. Kulozik, and J. Aguilera. Kinetics of formation and physicochemical characterization of thermally-induced β-lactoglobulin aggregates. *Journal of Food Science*, 75(5):E261–E268, 2010.